Metal Cluster Sputtering under reactive Ion Bombardment investigated by TOF-SNMS-Laser-System

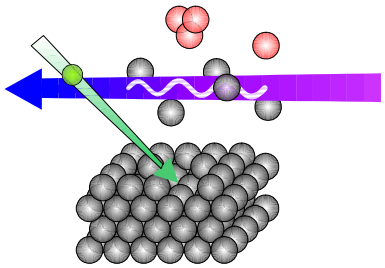

Dissertation

Submitted to the Department of Physics, University of Duisburg-Essen

In order to fulfill the requirements for the academic degree

Doctor rerum naturalium (Dr. rer. nat.)

by

Sobhy Ahmed Nassar Ahmed Ghalab
born in Ghariba, Egypt

1. Referee: Prof. Dr. A. Wucher
2. Referee: Prof. Dr. R. Möller

Public defence held on 13.07.2005

July 21, 2005

Contents

1 Introduction

Sputtering is the removal of materials from the surface of a solid through the impacting of energetic particles. The materials released from the bombarded surface consist predominantly of neutral atoms and secondary ions positively or negatively charged [Be81], [Be91]. The sputtering process has been the subject of scientific investigations for long time. First discussions over the sputtering by atomic beams were already underway at the beginning of the last century [St08], [St09], [Hi27]. Besides atomic species, the flux of sputtered particles contains an abundant fraction of agglomerates of two or more atoms; these species were called sputtered clusters. R. Honig [Ho58] was the first to report on sputtered clusters in 1958s, he succeeded in detecting positively charged silver dimers within the flux of particles emitted by sputter erosion of cathode in a gas discharge. Hortig and Müller [Ho69] observed negative clusters with a size up to 60 Ag_n^- atoms when they bombarded polycrystalline silver (which was partly covered in Cs in order to enhance negative formation) with 15 keV Kr^+. This record in cluster size was only broken by Katakuse et al .[Ka85], [Ka86], who found Ag_n^+ clusters containing up to more than 200 atoms sputtered from polycrystalline silver under bombardment with 10 keV Xe^+ ions. In fact, the secondary ion mass spectrometry (SIMS) suffers primarily from the strong matrix effects i.e. the flux of a specific kind of particles changes not only as a function of the surface concentration of this specific particle type, but mainly due to the presence of other elements at the surface. Due to this effect, the quantification based on the SIMS signal is difficult. Therefore, it is very essential to investigate the sputtered neutral species.

Therefore, several attempts have been made to study sputtered neutral clusters that have to be post-ionized prior the detection by analytical techniques. A highly successful investigation of sputtered neutral clusters was performed in the seventies of last century, when Oechsner and Gerhard determined the abundance of neutral dimers and trimers sputtered from various metallic samples by sub-keV Ar^+ ions. In these experiments the neutral species were post-ionized by means of low pressure RF argon plasma sustained by electron cyclotron wave resonance [Oe74], [Oe78]. After several years this work was continued by Gnaser et al. [Gn89] and Franzreb et al [Fr90] by using an electron beam impact to post-ionize neutral species. Due to the relatively low ionization efficiency of both plasma and electron impact post-ionization methods, the size of sputtered neutral clusters detected experimentally was for a long time limited to very small clusters containing less than five atoms.

C. H. Becker [Be84], was the first to utilize the non-resonant multiphoton ionization to post-ionize sputtered neutral clusters. By bombarding copper under Ar^+ ions at impact energy of several kilovolts, he observed atoms and

dimers. As a consequence, laser has became routinely being used to post - ionizing neutral sputtering species with a high post-ionization efficiency [Co91], [Co93], [Co94], [Wu93a], [Wu93b]. Using this technique, a large number of sputtered neutral clusters for several metals has been detected. In addition, spectra of kinetic energy distributions of sputtered particles were determined. The mass spectrometry of secondary neutrals (SNMS) has two major advantages: (i) the ionization efficiency is increased compared to SIMS process, (ii) matrix effects are reduced because the sputtered neutral particles are ionized after they have left the target body and when the chemical environment has lost the most of its influence [Wu001].

So far, numerous studies have been conducted to determine the factors affecting the enhancement of sputtering yield i.e., the number of particles emitted per the number of incident [Be81]. These studies pointed out the secondary ion yields depend strongly on the electronic and chemical properties of the surface of solids. Purposeful modification of surface chemistry to obtain a high secondary ion yield has been achieved by the judicious selection of the bombarding ion species. In particular, Andersen [An70], [An73] demonstrated drastically higher positive secondary ion yields were obtained under bombardment by ions of an electronegative element e.g. O_2^+ than by inert gas e.g. Ar^+. Andersen attributed this enhancement to the increased surface work function of oxidized metal. On the basis of these observations, the oxygen ions O_2^+ are routinely used for sputtering in positive secondary ion mass spectrometry (SIMS) to enhance detection sensitivities [Be75]. In more detail, high secondary ion yields are observed for these elements that can be completely oxidized and form strong ionic bonds with oxygen [Be75]. However, the secondary ion yields may be decreased up to several orders of magnitude either for elements that form weak bonds with oxygen or are only partially oxidized under O_2^+ bombardment [St77].

Since the halogen elements (e. g. fluorine F^+ ions) are higher reactive with metal than oxygen, one would expect strong metal-fluoride bonds compared to metal oxides. Therefore, higher secondary ion yields will be expected for elements that only partially oxidize with oxygen under bombardment by projectiles containing fluorine. To address this point, Reuter and coworkers [Re87], [Re88a], [Re88b] have investigated experimentally the ionization probabilities and relative sputtered yields produced from different target metals bombarded with O_2^+ and F_2^+ or CF_3^+. Their studies demonstrated the use of F_2^+ or CF_3^+ as projectiles leads to a drastic increase in both ionization probability and ionic sputtered yield for elements that have weak oxide bonds with oxygen. As a consequence, SF_5^+ projectile has been demonstrated to be very effective in secondary ion mass spectrometry (SIMS) of organic surface. Such projectile has two advantages: (i) it has F atoms that enhance the secondary ion yields as mentioned previously (ii) it is a polyatomic projectile that leads to significant enhancements of both the total Y_{tot} and partial Y_X sputtering yield of secondary

cluster ions (Y_{tot}: the average number of target atoms sputtered per impinging projectile & Y_X the average number of a certain sputtered species per impinging ion) [An93], [Ap89]. More specifically, it has been shown that particularly the signal measured for complex molecular ions is drastically enhanced under SF_5^+ bombardment as compared to usually employed rare gas or O_2^+ projectile ions [Ha98], [Ko98a], [St98], [Gi98], [Gi2000]. A similar enhancement was observed when a Si (100) surface is bombarded with $SF_5^+$and SF^+in comparison to Xe^+ [Ya98]. These observations suggest that the relative abundance of clusters among the sputtered flux may also be enhanced, if the surface is bombarded with SF_5^+ ions as compared to rare gas ion projectiles of the same kinetic energy. [Ya2000].

In most of these experiments, only the charged fraction of the sputtered flux (secondary ions) has been analyzed. Since it is known that the majority of sputtered particles leaves a metal surface as neutrals, it is not clear whether the secondary ion yield enhancements observed in the literature are caused by an enhancement of the partial sputtering yield of complex species or rather relate to an enhanced ionization probability, i.e., the probability that a sputtered particle becomes ionized in the course of the emission process. It is therefore necessary to perform similar experiments detecting the corresponding sputtered neutral species.

The present work is intended to examine previously observations on SF_5^+ projectiles in comparison to monoatomic projectiles by investigation both of ionic and neutral particles sputtered from a metallic surface under otherwise identical conditions. In order to get more information about the effect of fluorine nuclearity in projectile ions on the formation of sputtered clusters we have used SF_m^+ ($m = 1, ..., 5$) projectiles. As a first step, indium metal is selected for investigation since: (i) the largest neutral sputtered clusters have been observed for indium under rare gas ion bombardment [St002] and (ii) the photo-ionization of sputtered neutral indium atoms and clusters is easily saturated using single photon ionization at a convenient wavelength of 193 nm [St002]. In second step, silver is selected as a target surface to expand our work. In this respect, it is well known that (i) the rare gas ion bombardment of a silver surface produces relatively large amounts of Ag_n clusters [St2000] and (ii) for this element a large database on sputtering of clusters under various sputtering conditions is already available in literature. Therefore, our results can be compared with the published data. In a third step, the experiments are repeated in a different ultrahigh vacuum system containing an X-ray photoelectron spectrometer in order to obtain more information about the surface chemistry of silver subjected to SF_m^+ bombardment and to determine the concentration of fluorine of bombarded surface as a function of projectile nuclearity.

The thesis is organized as follows: after the introduction, **Chapter 2** provides the physical basis of the sputtering process and describes the different

kinds of sputtering events.

Chapter 3 presents an overview about the studies that have been done experimentally and theoretically on the formation of sputtered clusters. Moreover, an overview about the influence of reactive ion bombardment on secondary ion yields is given.

Chapter 4 describes the experimental setup and different equipments that have been used in the present work.

Chapter 5 displays the time synchronization between target potential, primary ion and ionizing laser: Further, the basic principles of measurements in the laser SNMS technique employed in the present work will be described.

Chapter 6 discusses the photo-ionization process of sputtered species by the laser beam.

Chapter 7 displays the obtained experimental results, which contain investigations of the bombarded surface by (i) time-of-flight mass spectrometry (TOF-MS) connected with a UV laser system and (ii) X-ray photoelectron spectrometry (XPS)

Chapter 8 presents the summary, the conclusions of the present work and an outlook for future research.

2 Physical basis of the sputtering process

2.1 Description of sputtering process

The sputtering process can be described qualitatively, at least for amorphous and polycrystalline samples, by the Sigmund collisional sputtering theory [Si69], [Be81], [Si87]. In this theory an impinging primary ion experiences a series of collisions in the target material, recoiling atoms with sufficient energy go through secondary collisions and create further generations of recoiling atoms. The recoil atoms have a chance to leave the target surface as secondary ions, if they have enough energy to overcome the surface binding energy. The majority of sputtered particles emitted from clouds of high order recoil atoms has very low energies (several electron volts) and originate from the uppermost atomic layers of the target. The major concepts of the collisional picture of sputtering theory are found in the reviews of Sigmund [Be81], Thompson [Th81]. They can be summarized as follows:

- Stopping of the projectile via energy loss to target atoms (nuclear stopping power and electronic stopping power);
- Occurrence of a linear collision cascade;
- Escape of certain recoil atoms through the surface potential energy barrier;

Sigmund had also succeeded to compute the sputtering yield Y, which is defined as

$$Y = \frac{\text{mean number of sputtered particles}}{\text{incident particles}}$$

Sigmund's general yield expression is given by:

$$Y(E) = \Lambda \alpha N S_n(E) \tag{1}$$

Where Λ is a material constant including the range of displaced target atoms and the probability of the ejection of an atom at the surface, α is a dimensionless correction factor, N is the atomic density of the target, and $S_n(E)$ is the nuclear stopping cross section as a function of the initial energy E of the projectile. Sigmund's yield expression takes low and high energy forms. For ion energies smaller than 1 keV the yield is:

$$Y(E) = \frac{3}{4\pi^2} \alpha \frac{\gamma E}{U_0} \tag{2}$$

Where γ is the energy transfer mass factor for elastic collisions that will be defined in Eq. (15), and U_0 is the surface binding energy, which is defined as the minimum energy needed to remove an atom from the surface. As a general

rule, Sigmund used thermodynamic data (heat of sublimation) for U_0. For energies greater than 1 keV the yield given by

$$Y(E) = \frac{\left(0.042\mathring{A}^{-2}\right)\alpha S_n(E)}{U_0} \tag{3}$$

In order to estimate the nuclear stopping cross section for elastic collisions S_n, assume that an projectile ion with atomic number Z_1 and atomic mass M_1 moving with velocity v collides with an target having atomic number Z_2 and atomic mass M_2. It is known that in elastic scattering the energy and momentum of the projectile are the same before and after collision, the change in momentum is given by

$$\Delta P = \int_{-\infty}^{\infty} F_0 dt \tag{4}$$

$$\Delta P = \frac{1}{v}\int_{-\infty}^{\infty} F_0 dx \tag{5}$$

where F_0 is the component of the force acting on the ion perpendicular to its incident direction.

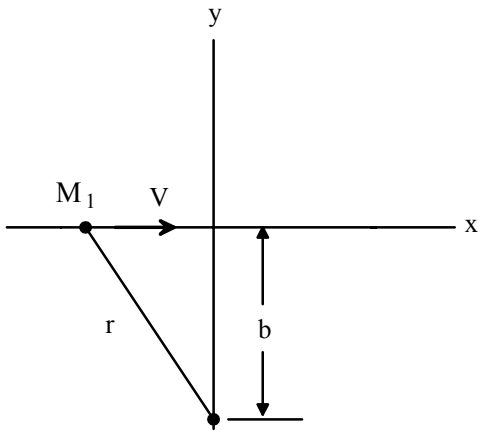

Figure 1: Approximation diagram for the change of momentum

By using the geometry of Fig. 1 the force may be rewritten with $r = (x^2 + b^2)^{1/2}$, therefore:

$$F_0 = -\frac{\partial V(r)}{\partial y} = -\frac{\partial V\left(\left(x^2+b^2\right)^{1/2}\right)}{\partial b} \tag{6}$$

Then

$$\Delta P = -\frac{1}{v}\frac{\partial}{\partial b}\int_{-\infty}^{\infty} V\left(\sqrt{x^2+b^2}\right)dx \tag{7}$$

The interaction potential between two atoms Z_1 and Z_2 can be written in the form of a screened coulomb potential using χ as the screening function,

$$V(r) = \frac{Z_1 Z_2 e^2}{r} \cdot \chi\left(\frac{r}{a}\right) \tag{8}$$

where a is the Thomas-Fermi screening length, given by

$$a = \frac{0.8853 a_\circ}{\left(Z_1^{2/3} + Z_2^{2/3}\right)^{1/2}}$$

where $a_\circ$ is the Bohr radius, 0.529 $\mathring{A}$.

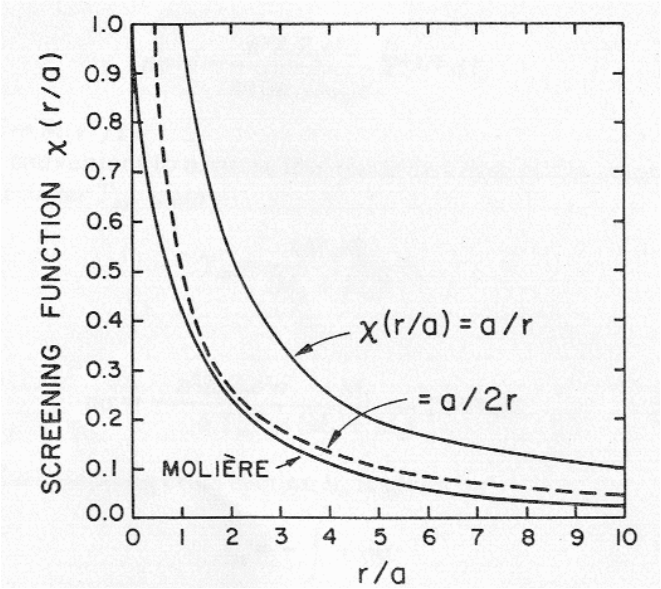

Figure 2: The screening function χ in the Moliere approximation. At $r = a$, the value of the screening function has dropped to about 0.4 in support of the choice of a as an approximation for the atomic size. Also the screening function $\chi = a/r$ and $a/2r$ are shown [Fe86]

It is well known that the screening function has several values depending on the kind of potential (Fig. 2). We put $\chi\left(\frac{r}{a}\right) = \frac{a}{2r}$, this value is the most appropriate to describe the linear collision cascade. Now Eq. (8), becomes

$$V(r) = \frac{Z_1 Z_2 e^2 a}{2r^2} \tag{9}$$

by substituting Eq.(9) into (7) we obtain on

$$\Delta P = -\frac{1}{v}\frac{\partial}{\partial b}\int_0^\infty \frac{Z_1 Z_2 e^2 a}{x^2 + b^2} dx = \frac{\pi Z_1 Z_2 e^2 a}{2vb^2} \tag{10}$$

where the total energy T transfer to the recoiling nucleus is given by

$$T = \frac{\Delta P^2}{2M_2} = \frac{\pi^2 Z_1^2 Z_2^2 e^4 a^2}{8M_2 v^2 b^4} \tag{11}$$

The total cross section of a scattering process is determined by the change of differential cross section $d\sigma(T)$ for transferred energy between T and $T + dT$

$$d\sigma(T) = -2\pi b(T)\, db \tag{12}$$

by solving Eq. (11) with respect to b, calculating db and inserting it into Eq. (12) we obtain

$$d\sigma(T) = -\frac{\pi^2 Z_1 Z_2 e^2 a}{8\sqrt{M_2/M_1 E}} T^{3/2} dT \tag{13}$$

Where $E = \frac{1}{2} M_1 V^2$ is the initial kinetic energy of the projectile. It is convenient to express this result in terms of the maximum energy transfer in elastic collision $T_{\max}$, where

$$T_{\max} = \frac{4M_1 M_2}{(M_1 + M_2)} E = \gamma E \tag{14}$$

and

$$\gamma = \frac{4M_1 M_2}{(M_1 + M_2)} \tag{15}$$

Then we get

$$d\sigma = -\frac{\pi^2 Z_1 Z_2 e^2 a}{4T_m^{1/2}} \frac{M_1}{(M_1 + M_2)} T^{-3/2} dT \tag{16}$$

The nuclear stopping cross section is given by

$$S_n = -\int_0^{T_{\max}} T d\sigma = -\int_0^{T_{\max}} -\frac{\pi^2 Z_1 Z_2 e^2 a}{4\sqrt{T_m}} \cdot \frac{M_1}{M_1 + M_2} \cdot T^{-\frac{3}{2}} dT = \frac{\pi^2 Z_1 Z_1 e^2 a M_1}{2(M_1 + M_2)} \tag{17}$$

The nuclear stopping power dE/dx is the product of the cross section and the atomic density of target N, therefore we have

$$dE/dx = N S_n = N \frac{\pi^2 Z_1 Z_1 e^2 a M_1}{2(M_1 + M_2)} \tag{18}$$

Note that the dE/dx with this approximation of χ is independent of energy. This result is in contrast to the dependence of nuclear stopping power on the energy of projectile that is observed in experimental work (see Fig. 3). In order to estimate a general form for S_n, a more widely used form of the interaction potential is:

$$V(r)\,\alpha r^{-1/m} \tag{19}$$

where m is an energy dependent parameter varies from $m = 1$ at high energies to $m \approx 0$ at very low energies. By inserting Eq. (19) into Eq. (7) the change of cross section $d\sigma(T)$ becomes

$$d\sigma(T) = C_m E^{-m} T^{-(1+m)} dT \quad ; \qquad 0 \le T \le T_{\max} \tag{20}$$

where C_m is constant, a general form for the nuclear stopping cross section is

$$S_n(E) = \frac{1}{1-m} \cdot C_m \gamma^{1-m} E^{1-2m} \tag{21}$$

The last equation gives good information on the behavior of S_n at different ion energies. It is predicted that at low energies, where ($m \approx 0$) the $S_n(E)$ should increase linearly with E, approaches a plateau at intermediate energies ($m \approx 0.5$) and falls off at higher energies ($0.5 < m \le 1$). At $m = 1$ the $S_n(E)$ should decrease like E^{-1}, but diverges due to the $\frac{1}{1-m}$ factor. These results are in good agreement with the experimental data on the sputtering yield of amorphous silicon bombarded with Ar^+ ions at different energy range (Fig. 3).

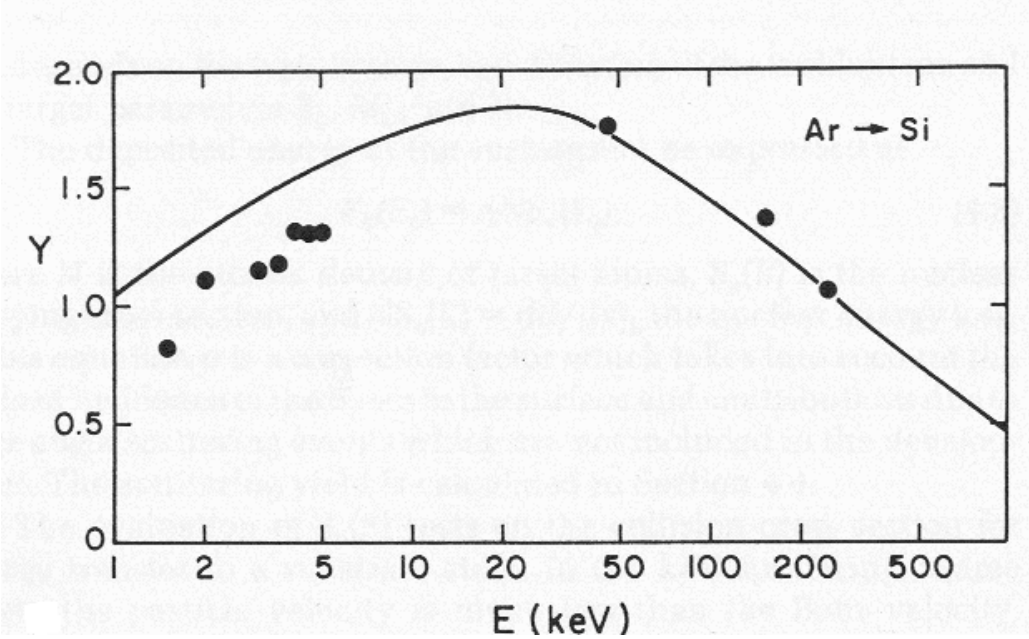

Figure 3: The energy dependence of the sputtering yield (Y) of amorphous silicon bombarded with Ar^+ ions [An75].

On the basis of this result, $S_n(E)$ depends on the atomic model that is used to describe the interaction. In particular, on the form adopted for the screened

Coulomb potential. The last equation can be rewritten in a more compact form

$$S_n(E) = \left(\frac{4\pi a e^2 Z_1 Z_1 M_1}{M_1 + M_2}\right) \cdot s_n(\epsilon) \tag{22}$$

where $s_n(\epsilon)$ is a universal function depending on the detailed form adopted for the screened Coulomb potential that has several proposed forms for different screening approximations. ϵ is the reduced projectile energy given by

$$\epsilon(E) = \left[\frac{aM_1}{Z_1 Z_2 e^2 (M_1 + M_2)}\right] \cdot E \tag{23}$$

and defined as the projectile energy in the center of mass frame normalized by the potential energy of the projectile-recoil combination when separated by the screening length. The accurate value of the nuclear stopping power (dE/dx) is given by

$$dE/dx = 4N\pi Z_1 Z_1 e^2 a \frac{M_1}{M_2 + M_1} \cdot s_n(\epsilon) \tag{24}$$

According to Lindhard and coworkers [Li63] the energy loss per unit length in the target (stopping power) is given as the sum of nuclear $S_n(E)$ and electronic $S_e(E)$ stopping powers, which describe the elastic and inelastic collision respectively.

$$\frac{dE}{dx} = \left(\frac{dE}{dx}\right)_n + \left(\frac{dE}{dx}\right)_e = -N(S_n(E) + S_e(E)) \tag{25}$$

The relative importance of the various interaction processes between the ion and the target medium depends mostly on the ion velocity and on the charges of the ion and target atoms. A comparison of the nuclear and electronic stopping powers is shown in Fig. 4

It is seen that, in the first order at lower velocities $\epsilon \leq 1$ the nuclear cross section increases linearly with energy reaching a plateau at intermediate energy, and then decreases at higher energies. Contrary to nuclear stopping, electronic stopping does not cause appreciable scattering of the penetrating particles because of the small electron mass. At low projectile energies electronic stopping is proportional to the particle velocity and can be neglected in the low keV energy range. At higher velocities, for $(v \leq Z_1^{2/3} e^2/\hbar)$ the nuclear stopping decreases and electronic stopping becomes dominant at range of about MeV, and the $S_e(E)$ in this range is given by Lindhard and Scharff [Li61] formula:

$$S_e(E) \approx \xi_e 8\pi e^2 a_\circ \frac{Z_1 Z_2}{Z} \frac{v}{e^2/\hbar} \tag{26}$$

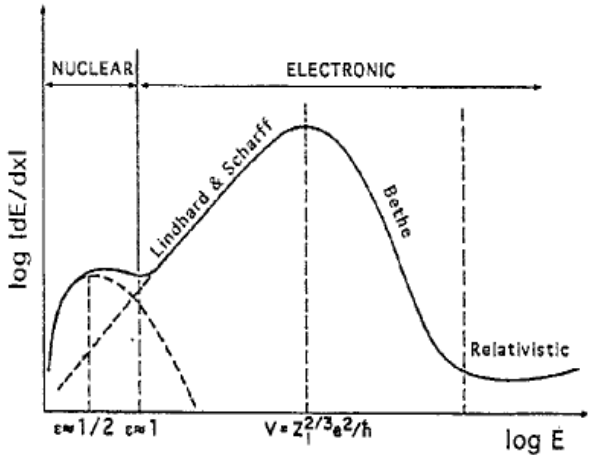

Figure 4: Stopping power of an ion as function of its energy E. At the lowest ion velocities ($\epsilon \leq 1$ Eq. 23) nuclear stopping dominates for heavy and medium mass ions (keV range and below), and is competitive for light ions. At higher velocities, for ($v \leq Z_1^{2/3} e^2/\hbar$) nuclear stopping decreases and electronic stopping becomes dominant (MeV range) according to Eq. (26) In this regime the projectile is preferable neutral. Beyond the stopping power maximum, the Bethe regime Eq. (27) is approached where the projectile is preferably stripped. In the extreme relativistic regime the electronic stopping power increases again [Be81]

where $Z = (Z_1^{2/3} + Z_2^{2/3})^{1/2}$ and ξ_e is a function of the atomic number Z_1. At very high projectile velocities ($v >> e^2/\hbar$) for protons and even higher heavier particles, the S_e described by Bethe's form:

$$S_e(E) = \frac{4\pi e_1^2 Ze}{mv}\left(\log\frac{2mv^2}{I} + correction\ terms\right) \tag{27}$$

where e_1 is the projectile charge, e the electron charge and I is the mean ionization potential. Note that the range of validity of Eq. (27) is outside of the scope of most sputtering experiments [Be81].

2.2 Classification of sputtering events

The atoms in the target surface can be sputtered, if the primary particles transfer during the process of a collision cascade sufficient energy to an atom near the surface, so that it can overcome the attractive surface binding energy and escape to the vacuum. Depending on the energy of the recoiling target atoms after collision with the projectile and on the spatial density of the recoils, it can be distinguished between different collision cascade regimes [Be91].

2.2.1 Single knock-on regime

In the single knock-on regime only small energy is transferred between the projectile and target atoms. The recoil atoms at the target surface may receive

sufficient energy to overcome the surface binding energy, and thus may be sputtered. The received energy is not enough to generate recoil cascades, then in this regime only few collisions can occur (Fig. 5a). The Single knock-on sputtering may be expected, if a target is bombarded under low energy or for light projectile such as H, He. In that case the projectile may be reflected from a sub-surface atom.

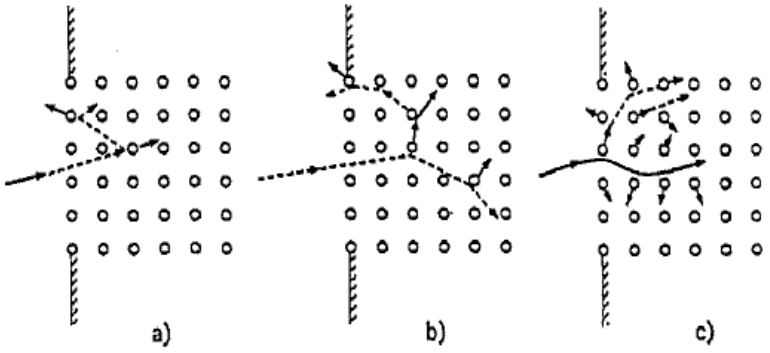

Figure 5: A schematic representation of sputtering by elastic collision: (a) the single knock-on regime; (b) the linear cascade regime; (c) the spike regime in which there is a high density of recoil atoms so that most atoms in a certain volume are moving [Be81]

2.2.2 Linear-cascade regime

If the target is bombarded with projectiles of medium or high masses with energies exceeding a few hundred eV, large energies are transferred to atoms in the surface target leading to the evolution of larger collision cascades; it can still be assumed that the collisions take place between a moving atom and an atom at rest (Fig. 5b). Such a cascade is termed linear because the solving of a Boltzmann transport equation describing the collision cascade is *linearized* under the assumption that only collisions between a moving atom and atom originally at rest occur. In this regime the sputtering yield Y_{lin} was predicted to scale linearly with the energy deposited in elastic collisions at the target surface [Si69], [Si81] :

$$Y_{lin} = \Lambda F_D\left(x = 0\right) = \Lambda\alpha\left(\frac{dE}{dx}\right) \tag{28}$$

Here, F_D is the energy deposited per unit depth at the target surface given by

$$F_D = \alpha N S_n\left(E\right) \tag{29}$$

And α is a dimensionless function of the incidence angle θ and the mass ratio M_2/M_1. In the linear cascade regime the dilute character of the cascade will

prevent a strict overlap, only the number of moving atoms is about twice as large as in the single knockon cascade.

2.2.3 Collision spike regime (nonlinear cascade)

At higher recoil densities, when the majority of atoms within the cascade volume are simultaneously in motion, the cascade is said to have entered the spike regime. In this case the projectile must have sufficiently high energy up to 10 keV and heavy atomic mass, to generate highly recoil densities of atoms in target surface (Fig. 5c). For such a spike regime, experiment shows and theory predicts that the sputter yield rises super-linearly with the energy deposited at the target surface, and thus such a cascade has been termed nonlinear [Si81a]. The difference between a linear collision cascade and a spike regime is that only a small fraction of the atoms are motion in a certain cascade volume in a linear cascade, whereas all atoms move in a certain spike volume. Experimental this difference is illustrated by bombardment with polyatomic projectiles [An75], [Sa005]. The formula of the sputtering yield in thermal spike regime has been estimated by Sigmund using thermodynamic concepts from kinetic gas theory [Si81]. The expression for the thermal sputtering yield is given by

$$Y_{th} = 0.0360 \frac{\lambda_\circ a^2 F^{*2}}{U^2} g\left(U/kT_\circ\right) \tag{30}$$

where $\lambda_\circ \simeq 24$, $a \simeq 0.219$ Å are Born-Meyer constants and k Boltzmann constant, U planar surface potential that confined an ideal gas (the surface binding energy), F^* is the energy deposited per unit track length at the surface $F^* \approx F_D$ and g a function given by

$$g\left(\xi\right) = \left(1 + \xi - \xi^2\right) Exp(-\xi) + \xi^3 \int_\xi^\infty dt \cdot e^{-t}/t \tag{31}$$

By comparing between the sputtering yield for linear cascade Eq. (28) and Eq. (30), the following observations may be made [Si81]:

- While Y_{lin} is proportional with the deposited energy F_D, Y_{th} varies more rapidly than proportional to F_D^{*2}, in view of the monotonic increase of $g\left(U/kT_\circ\right)$ with increasing F^*.

- The relative significance of the thermal and linear sputtering increase with increasing ratio of deposited energy and binding energy.

- For bombardment with polyatomic projectile (n-atomic), Y_{th} increases faster than n^2, while Y_{lin} is proportional to n at constant velocity.

3 Formation of clusters during the sputtering process

3.1 Experimental observation of sputtered clusters

Cluster ion emission has been studied for more than four decades [Ho58]. On the other hand, neutral sputtered clusters have been actively studied only for three decades after secondary neutral mass spectrometry SNMS (a technique able to detect effectively neutral sputtering species) was developed [Oe74], [Oe78]. Numerous studies have been devoted to investigate cluster emission in sputtering process at different bombarding condition. The most of these studies were conducted on metallic samples as model systems for purely collisional sputtering conditions. In the following text, some of the historical sequence on experimental investigation of sputtered clusters will be outlined.

A detailed representation of the experimental work in the area of molecular cluster sputtering until the end of the 1980*s* is found in an article of W. O. Hofer in [Be91]. Honig [Ho58] was the first to report on cluster during the sputtering of silver. He observed positively charged silver clusters up to 3 atoms when the sample surface was bombarded with noble gas ions at low energy ranging from 30 to 400 eV. Hortig and Müller [Ho69] observed negative clusters with a size up to 60 Ag_n^- atoms when they bombarded polycrystalline silver (which was partly covered in Cs in order to enhance negative formation) with 15 keV Kr^+. This record in cluster size was only broken by Katakuse et al .[Ka85], [Ka86], who found Cu_n^+, Ag_n^+ and Au_n^+ clusters containing up to more than 200 atoms sputtered under bombardment with 10 keV Xe^+ ions from the metal surface of copper, silver and gold, respectively. In fact, the secondary ion mass spectrometry (SIMS) suffers primarily from the strong matrix effects for secondary ion yield i.e. the flux of a specific kind of particles changes not only as a function of the surface concentration of this specific particle type, but mainly due to the presence of other elements at the surface. Due to this effect, a quantification based on the SIMS signal is difficult. Therefore, it is very essential to investigate the sputtered neutral species.

In order to detect the sputtered neutral species, several early attempts have been made to mass analyze the flux of sputtered neutral species. To post-ionize such species, electron-beam arrangements have been used by Honig [Ho58] and others [Sm63], as well as magnetically supported gas discharges by Cooper and co-workers [Wo64]. These studies succeeded in detecting mass spectrometric signals for sputtered neutral. However, the sensitivity was too low. Better sensitivity was obtained with the so-called glow discharge mass spectrometry (GDMS) described by Coburn and Kay [Co71]. In this method the plasma in a high frequency diode as employed for RF sputtering was used to ionize

neutral particles sputtered from the target under bombardment with plasma ions. Post-ionization was obtained via penning ionization.

$$X+A^* \rightarrow X^+ + A + e^-$$

Involving a high collision rate between sputtered neutrals X and metastable noble gas atom A*. Gerhard and Oechsner [Ge75b] have used a low pressure RF argon plasma maintained by electron cyclotron wave resonance to ionizing neutral particles and they succeeded in detecting clusters up to 3 atoms.

Gnaser et al. [Gn89] as well as Franzreb et al. [Fr90] have succeeded to determine masses and energy distributions of sputtered neutral clusters for several metals and semiconductors by using an electron beam to post-ionize the sputtered neutral species. Due to the relatively low ionization efficiency of both plasma and electron impact post-ionization methods, the size of sputtered neutral clusters detected experimentally was for a long time limited to very small clusters containing at most five atoms.

Only in the end of eighties in last century, the detection of larger neutral clusters became possible by the use of UV or VUV lasers to post-ionize the sputtered neutral species [Co91], [Wu93a], [Co93], [Co94], [Wa94] . In these experiments, it is of great importance that photo-ionization of the neutral clusters is achieved by absorption of a single photon. Therefore, a high ionization efficiency and low fragmentation rates have been achieved. It has been demonstrated that under these conditions the photo-ionization of sputtered neutral clusters can be saturated at moderate laser power densities, and the partial sputtering yields of clusters can therefore be determined from the measured data without prior knowledge of photo-ionization cross sections [Co91], [Wu93a]. From these investigations, the relative formation of clusters and the distributions of their kinetic energy were determined.

In the last two decades numerous experimental studies were accomplished to investigate the formation of cluster during sputtering process. In the following, we will briefly outline the most important results from the published data.

- It is well established that the neutral atoms and clusters are the main products of sputtering from the surface in case of metallic targets [Be75]. The contribution of charged particles from metal targets, i.e. SIMS ions only amounts from 10^{-3} to 10^{-4} depending on material and surface conditions.

- In both cases ionic (for large cluster size n) and neutral the sputtered cluster yields exhibit a power law dependence on the cluster size n (Fig. 6)

$$Y(n)\, \alpha n^{-\delta} \tag{32}$$

where n is a number of atoms in cluster. The exponent δ strongly depends on the bombarded material [Co93], [Wu96] as well as on the bombarding conditions such as energy and primary ion species [Wu93b], [Wa94], [Co94], while it is apparently independent of the crystallographic structure of the target material [Wu94]. Fig. 6 shows the cluster abundance distribution of ionic and neutral silver, the ionic clusters Ag_n^+ sputtered by 10-keV Xe^+ ions and the neutral clusters Ag_n sputtered by 5 keV Ar^+ ions . It is seen that the neutral clusters decreases relatively fast and the cluster ions exhibit a pronounced odd-even alternation (this behavior will be discussed in more detail in Section 7. 1. 2). The power law cluster distribution (Eq. 32) is found for a number of clusters (Al_n [Co93], [Wu96], Cu_n [Co93], [Co94] In_n [Ma94], [St002] , Ag_n, Ta_n and Nb_n [Wu96]). Therefore, this behavior seems to be a general feature of cluster emission in sputtering. The values of δ which have been determined experimentally using mass-spectrometry techniques are in range between 4 and 8, for those clusters containing up to approximately 40 atoms [Co91], [Wu93b]

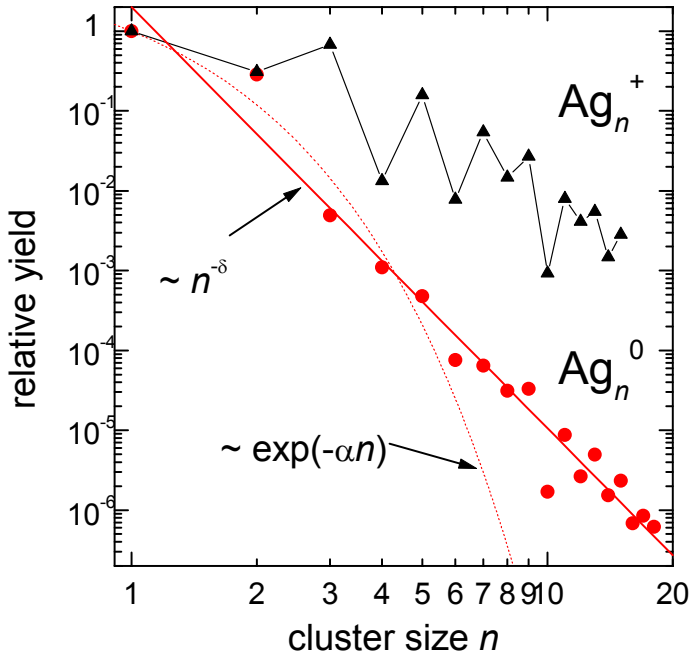

Figure 6: The relative yields of sputtered neutral and ionic silver clusters. The ionic clusters Ag_n^+ sputtered by 10-keV Xe^+ ions [Ka86] and neutral clusters Ag_n sputtered by 5 keV Ar^+ ions [Wu93a]

- So far no simple theoretical model of cluster formation in sputtering has

been able to reproduce both the power law cluster mass distributions and the high values of δ found experimentally. The only models predicting a power law mass distribution are the shock wave model of Bitensky and Parilis [Bi87], and the thermodynamic equilibrium model of Urbassek [Ur88]. However, the values of δ in these models are found around 2 and 7/3 respectively. This prediction is quite different in comparison with the high values of δ (ranging from 4 to 8) found experimentally. Quite recently, Rehn et al [Re001], and Staudt et al [St002] pointed out experimentally the formation of large sputtered clusters up to $n > 500$ atoms (Rehn) or $n > 50$ (Staudt) may obey the shock wave or thermodynamic model with an exponent δ of 2.

- High secondary ion yields are observed at the metal or organic surfaces bombarded with a chemically reactive projectiles such as O_2^+ [Wi78], N_2^+ [Ma86], [Ma87], CF_3^+ [Re87], SF_5^+ [Gh002] and SF_m^+ [Gh004] in comparison to rare gas ions.

- A new method has been developed to determine ionization probability $\alpha^{+,-}$, i.e. the probability that a sputtered particle becomes ionized in the course of the emission process. The technique is based on measuring in situ the yields of secondary ions and the corresponding sputtered neutral species [Wa94]. Investigations of metal surfaces (Ag, Ta, Nb and Ge) show that the ionization probability depends on cluster size n and varies for different metals [He2000]. The measured ionization probability α^+ is found to be below 10^{-3} for sputtered Ag, Ta, Nb and Ge atoms. This finding is in good agreement with the common sense that the formation probability for atomic ions ejected from the respective sputter cleaned metal surfaces is generally low. For small clusters containing less than 10 atoms, the ionization probability is found to increase strongly with increasing nuclearity of the sputtered cluster. This behavior was observed for all investigated metals, therefore may be considered as a general trend. For larger clusters containing more than 10 atoms, the ionization probability α^+ becomes fairly constant.

- In case of a clean metal surface the negative ionization probability α^- is found to be very small $\alpha^- << 1$, therefore the α^+ of positive ions represent the only major contribution of sputtered secondary ions [Wu93b].

- An empirical relation of exponents δ and total sputtering yields Y_{tot} (i.e. the average number of atoms sputtered per impinging projectile) was revealed for many combinations of projectile-target. The magnitude of the exponent is found to be inversely correlated with total sputtering yield (Y_{tot}) of the target in a way which is depicted in Fig. 7. It can be seen that large values of δ are connected with small values of Y_{tot} and vice versa. [Co93], [Wu96].

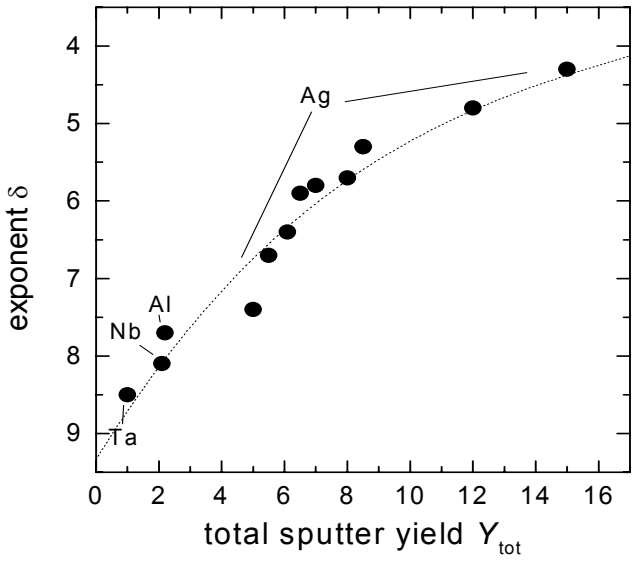

Figure 7: Power law exponent δ of experimental cluster yield distribution vs. total yield [Wu96]

- The use of polyatomic projectiles (clusters composed of several atoms) to bombard the target surface leads to non-linear enhancement effects, i.e. the total sputtering yield Y_{tot} may significantly exceed the sum of the yields induced by the constituent atoms arriving separately with the same impact velocity[An75].

3.2 Theoretical models of sputtered cluster

The modeling to describe the formation of clusters during the sputtering process has been developed for a long time in order to gain a better understanding of the mechanisms in this process and, to reproduce experimental quantities like the mass abundance distribution, relative sputtering yield, ionization probability as well as the kinetic energy of sputtered species. Several different theoretical models have appeared in literature. The most important of them will be briefly outlined in the following.

- **Direct emission mechanism (DEM)**

The principle idea in this model is based on the assumption that one single collision takes place between a recoil atom from the collision cascade in the target and a molecule already present at the target surface. These two atoms may leave the surface as a molecule under condition: the relative kinetic energy E_{cm}in the center-of-mass-system of the atoms must be low enough to

prevent fragmentation (lower than the dissociation energy D of the corresponding molecule), but the center-of-mass energy must be large enough to overcome the binding force between the molecule and the surface [Ge75a],[Be95]. This mechanism has been discussed in the literature several times starting with Benninghoven [Be73] followed by Oechsner et al.[Oe78], Sigmund et al.[Si86] and others. These studies have demonstrated that this mechanism can be applied for adsorbates and molecular solids but not for metals, since in metals and semiconductors the dissociation energy D of a dimer is typically smaller than the surface binding energy (sublimation energy) U_0. Therefore, the emission probability of an intact dimer is practically zero anyway under these conditions.

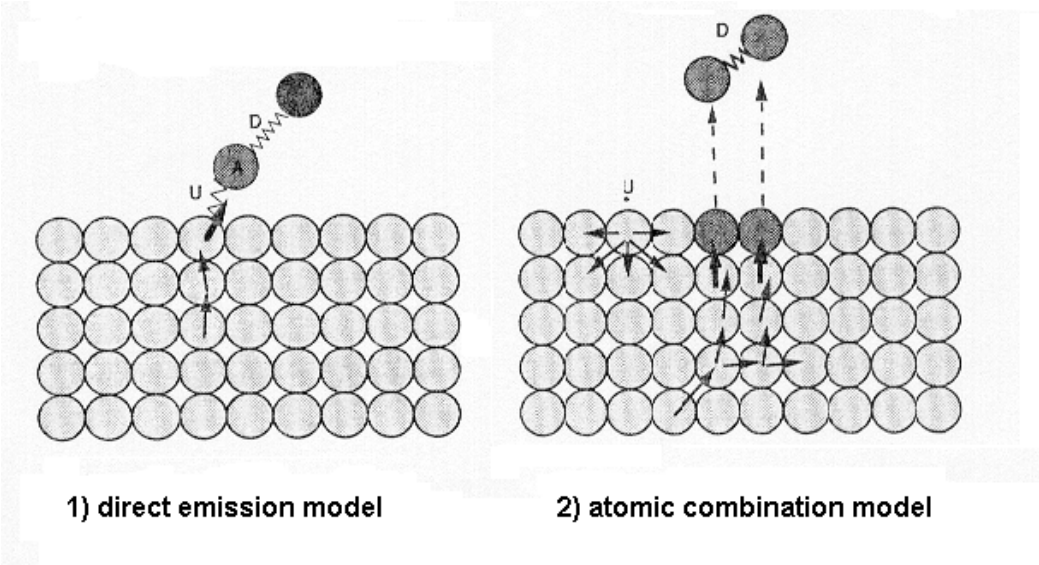

Figure 8: 1) In the direct emission mechanism energy is transferred in a collision to one constituent of a diatomic molecule at the surface, whose dissociation energy D is large compared with the surface binding energy U_0 of the molecule. 2) In the atomic combination model two atoms receive simultaneously almost parallel momenta leading to their emission. A dimer is emitted if the sum of the relative kinetic energies of the two emitted atoms is less than the dissociation energy of the dimer formed [Hu96]

- **Atomic combination mechanism (ACM)**

This model proposed that dimers or larger clusters are formed from independently ejected atoms, when they are emitted close enough in time and space and their relative kinetic energies are less than the binding energy of the corresponding clusters. The (ACM) model has been successfully applied by Gerhard and Oechsner [Ge75a], [Ge75b] to describe the yields of sputtered metal dimers and trimers for different targets as well as Können et al. [Kö74] have used it to evaluate the kinetic energy distribution of sputtered clusters. Wucher and Wahl [Wu96] have used the ACM to evaluate the yield for larger clusters in comparison with experimental results. Their studies demonstrated that at least for the

case of large clusters the ACM does not provide an accurate description of the cluster formation mechanism.

- **Thermodynamic model**

Urbassek et al [Ur88], [Ur96] pointed out the computer simulation results show that thermalisation may occur of the target surface after bombarded with energetic ions. This effect leads to the vaporization of a part of the irradiated material, with concomitant strong cluster abundance. The predicted cluster size distribution depends on the average energy density. For a small initial energy density, only a small number of atoms evaporate from the bombarded metal surface. For a high energy density, the solid atomizes, and clusters are formed with an exponential cluster distribution. For intermediate energy densities, prolific cluster formation is observed with a polynomial decay of the abundance distribution. These results are discussed in the light of the critical point of the gas-liquid phase transition. Depending on whether local thermodynamic equilibrium is established in part of the irradiated volume and on temperature with respect to the critical temperature when the system crosses the liquid-gas coexistence curve, the predicted mass distribution can obey a power law with an exponent of $-7/3$ or a combination of the two. This model was successfully applied to fit mass distributions of Ar_n^+, N_n^+, Ni_n^+ and $[Cs(CsI)_n]^+$ [Ur88].

- **Shock wave model**

This model is proposed to describe the formation of large clusters ($n > 3$) emitted when a high energy heavy ion interact with a solid surface [Bi87]. The analysis of both the experimental and theoretical results [Ho80], [Si74] has shown that the clusters are formed with greatest probability under heavy ion bombardment. This leads to a drastic increase of the sputtering yields due to the overlapping of elastic collision cascades. The overlap of the collision cascades and the formation of a high density energy deposition region could be the source of a shock wave [Bi87]. In fact, this model succeeds to predict a power law dependence of cluster yields $Y_n \; \alpha \; n^{-\delta}$, but it does not give the dependence of the exponent δ on bombardment conditions. The calculated values of $\delta \simeq 2$ are not in agreement with experimental data (where δ is ranging from 4 to 8) for metal sputtering [Co91], [Wu96]. Recently, Rehn et al [Re001], and Staudt et al [St002] pointed out experimentally the formation of large sputtered clusters up to $n > 500$ atoms (Rehn) or $n > 50$ (Staudt) may obey the shock wave with an exponent δ of 2

3.3 Computer simulation

Several methods have been developed to simulate sputtering processes that occur after interaction of the primary ions and the target surface. The developed simulation methods are based on two approaches: (i) binary collision

approximation (BCA) and (ii) molecular dynamics simulation (MD). Both the BCA and MD methods have been widely used for simulations of ion-solid interactions, Andersen reviewed this field in 1987 [An87]. Both methods will be briefly described in the following:

i) **Binary Collision Approximation**

The BCA was the first simulation model applied to ion-solid interactions. In this approach only one collision between two atoms is handled at a time. In between two binary collisions, the ion moves on a mean free flight path, the length of which can be chosen constant or exponential distributed depending on the particular algorithm [Ec91]. According to the target structure, two algorithms have been developed for the treatment of crystalline and amorphous or polycrystalline targets . For crystalline targets, the coordinates of all target atoms are known and generated during the trajectory. Besides conserving energy and momentum, such code also conserves the number of particles. The most widely used program of such code is MARLOWE [Ro74].

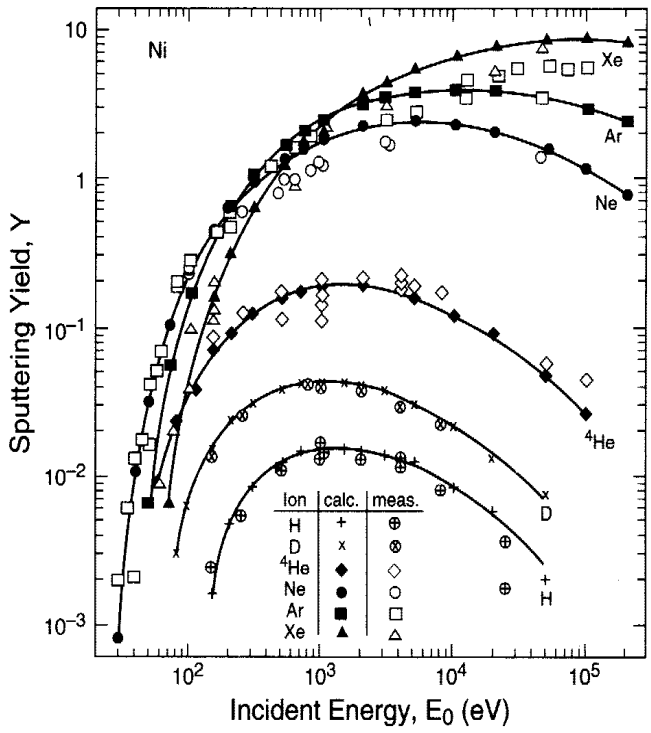

Figure 9: Comparison of TRIM calculations with experimental measurement of the sputtering yield Y, versus incident energy of various gas ions incident on a Ni target [Zi85]

For amorphous targets the atomic arrangement is random, therefore a stochastic algorithm is used to determine the locations of target atoms, select impact parameters and so forth. The impact parameters then are chosen randomly, the randomization of the sputtering conditions qualifies this method as a Monte Carlo method. Such code conserves energy and momentum in individual collisions, but does not conserve particle number. One principle example of such programs are the family of TRIM (transport of ions in matter) codes [Zi85]. TRIM is used to calculate all kinetic energy phenomena associated with the ion energy loss : target damage, sputtering, ionization and phonon production.

Fig.9 compares the TRIM calculated and experimentally determined sputtering yield Y versus incident energy of ions impinging normal onto the surface. It is seen that the agreement between TRIM and experimental data is excellent. In the present work we have used the SRIM2003 code to calculate the effective stopping power (dE/dx) and deposited energy (F_D).

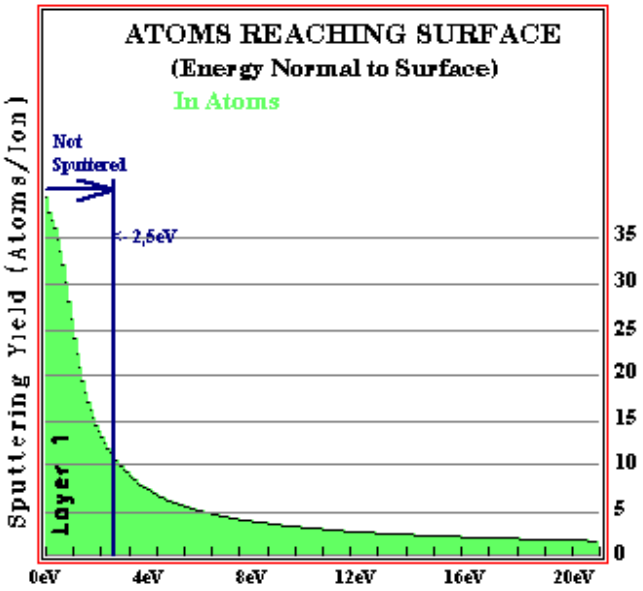

Figure 10: The cumulative energy distribution of particles arriving at a polycrystalline indium surface calculated using TRIM2003.

Fig.10 shows the cumulative energy distribution of all atoms reaching the surface of a polycrystalline indium target during 1000 individual trajectories after 10-keV Ar^+ bombardment, calculated using SRIM2003. The calculated sputtering yield is 10.4 atoms/ion for a surface binding energy U_0 of 2.5 eV. It can be seen as Eq. (3) in Section 2.1 that changes in the value of U_0 can cause substantial changes in the number of ejected particles.

Note that the binary collision approximation breaks down when the ion mean free path approaches the average atomic spacing in the target (spike regime). Under such conditions, the interactions between the ion and target atoms become a many body problem and an MD approach is required for an accurate simulation.

ii) **Molecular Dynamics (MD)**

Molecular dynamics can be described as the computation of the motion of a system of particles from the knowledge of the interaction forces between the particles. The dynamics of the system can be determined by solving the classical equations of motion (Newton·s law) for all atoms of the system simultaneously. In contrast to the BCA, this method can give insight into atomic scale processes during the collision as well as describe cluster emission phenomena which are in principle is impossible to model by other methods [Ur97]. By MD the spike regime is not more difficult to simulate than the linear sputtering regime. Cluster emission, or any other effect that depends on the details of the interatomic attraction is easy to calculate as soon as a potential is available which describes the attraction in the solid at the surface and in the cluster as well. As a consequence, a number of MD studies have been devoted to investigate the formation of clusters during sputtering process [Win78], [Ga78], [Ha81], [Ga88]. Theses studies demonstrated that, the most important parameter of MD is the selected potential function employed to describe the interaction between the primary ion and target atoms and among target atoms themselves. In this respect two kinds of potential functions have mainly appeared in literature: pair potentials and many-body potentials. Harrison and Delaplain [Ha76], were the first to report on the use of MD that include interatomic attractive forces (pair potential) to investigate the formation of sputtered copper clusters under argon bombardment. The total energy of a system of N particles at the nuclear coordinates $\{R_i\}$ interacting via a pair potential V can be written as

$$E(\{R_i\}) = \sum_{i}^{N} \sum_{J<I}^{N} V(r_{ij}) = \frac{1}{2} \sum_{i}^{N} \sum_{J \neq i}^{N} V_{ij} \; ; \qquad \mathrm{r_{ij}} = |Ri - Rj| \tag{33}$$

In atomic collisions with kinetic energies which are significantly higher than the binding energy, the repulsive potential during close approaches dominates the interaction. Consequently, purely repulsive potentials are sufficient to calculate the scattering during the collision. The pair potential model has been successful for some purposes, however this potential can not describe a solid and a small gas phase cluster at the same time. As the time dependent variation of the interaction potential is encountered and the potential function has to be switched at some stage during the sputtering process.

Two main classes of many-body potentials have been developed for use in MD simulations of ion-solid interactions. The first class of many body potential

is based on a tight-binding method [Ma89], that belongs to the approximations which attempt to calculate the interatomic forces by a quantum mechanical treatment of the electrons. The second class of many body potential is based on the so-called embedded atom method (EAM) [Ga88]. For systems with delocalized electronic states e.g. metal, the pair potential is complemented by the contribution of the embedding medium, which is determined by the surrounding. The total energy of such a system is given by

$$E(\{R_i\}) = \frac{1}{2}\sum_{i}^{N}\sum_{j\neq i}^{N} V_{ij} + \sum_{i}^{N} U_i \left[\sum_{j\neq i} g(r_{ij})\right] \tag{34}$$

the second term is the embedding function, where g is a function describing the local environment (for instance electron density) of atom i in terms of the position of its neighbors, and U is a function describing how the energy of atom i depends on its environment. Modern simulation employing EAM, have been widely used to describe atom- atom interaction. The findings by this method exhibit in many cases a good agreement with experimental data [Ga88], [Wu92].

3.4 Formation of sputtered clusters under reactive ion bombardment

After a series of experimental studies on the effect of different projectiles (noble gas or chemically reactive) on the ionic sputtered yields, it has been demonstrated that the use of electronegative elements like halogens (F_2^+, CF_3^+,...) [Re84], [Re87], Oxygen [Wi78] and nitrogen [Ma86], [Ma87] to bombard metal surface leads to a drastic increase of positive and negative secondary ion yields compared to those produced by noble gas projectiles. The enhancement of secondary ions by chemical reactive projectiles depends on the kind of bombarded surface. High secondary ion yields are observed for those elements that can completely oxidize and form strong ionic bonds with oxygen. However, the secondary ion yields may be decreased up to several orders of magnitude for those elements that form weak bonds with oxygen or those are only partially oxidized under O_2^+ bombardment. Since the ionicity of metal-fluoride bonds is considerably larger than that in metal oxides, one would expect higher secondary ion yields for these elements under bombardment with F_2^+ ions or projectiles containing fluorine. To indicate this point, Reuter and Clabes ([Re87], [Re88a], [Re88b]) have investigated experimentally the ionization probabilities and relative sputter yield which are produced from different targets metal bombarded with O_2^+, F_2^+ and CF_3^+ . Their studies demonstrated that the use of F_2^+ or CF_3^+ as projectiles lead to drastic increase of ionization probability and ionic sputtered yield for those element that have weak oxide bond with oxygen. In fact these observations of the enhancement of secondary ion yields by chemically reactive projectiles, cannot be simply explained on the basis of electron tunneling mechanisms. Therefore, several models have been proposed in order to rationalize the effects of reactive species on sputtered ion yields. The most important of them will be briefly outlined in the following.

- **The Bond-breaking model**

The idea of ionization by bond breaking started with the observation that the sputtered ion fraction is very sensitive to surface chemistry [Sl66], [Be75]. Slodzian [Sl75] was the first to suggest the bond-breaking concept to explain the large secondary ion emission observed during the sputtering of ionic solids. This model has been extended to explain the chemical effects on the yield of secondary ions and excited atom emission from oxides where the bonds are only partially ionic [Wi79]. Slodzian and Williams pointed out that the ionization of a sputtered atom via the breaking of the bond with electronegative atom (e.g. oxygen) at the surface, is very similar to the charge exchange mechanism in the Landau-Zener curve crossing model for atomic collisions.

On this basis M. L. Yu [Yu86] has proposed a model to examine the general features of the bond-breaking concept. The model assumes that the sputtering of an atom M^+ from an oxide molecule breaks the local surface oxide bond

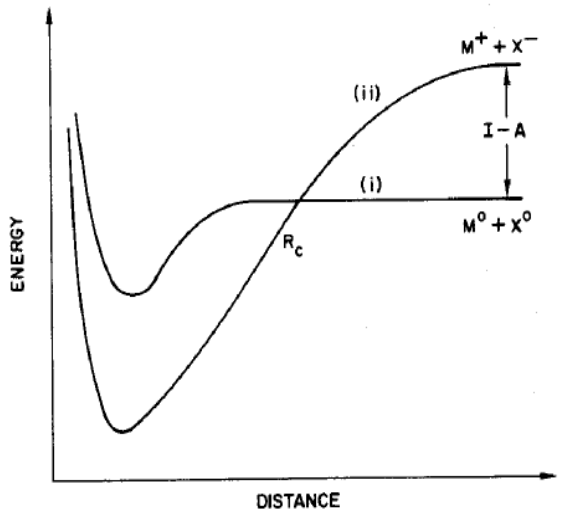

Figure 11: Schematic energy diagram showing the crossing of the covalent energy curve $M^{\circ}+X^{\circ}$ and the ionic potential energy curve $M^{+}+X^{-}$ at the crossing point R_c. In the bond-breaking model, charge exchange can occur at the crossing of these diabatic curves at the distance R_c [Yu87].

and creates a cation vacancy X on the surface. It is assumed that the cation vacancy during the sputtering of M^+ can trap the electron left behind, with an electron affinity A. Fig. 11 shows the diabatic potential-energy curves that can be employed to describe a charge exchange in a sputtering a process. Charge exchange can happen at the crossing of the diabatic covalent potential curve M^0+X^0 and the diabatic ionic potential curve $M^+ + X^-$ at a distance R_c from the surface. If there is no degeneracy, the ionization probability P^+ is given by the Landau-Zener formula:

$$P^+ = \exp(-\frac{2\pi H_{12}^2}{v\,|a|})|_{R+R_c} \tag{35}$$

where H_{12} is the transition matrix element, v is the velocity of the emitted particles, a is the difference in the first derivatives of the potential curves and R is the distance between the sputtered atom and the surface vacancy, all evaluated at R_c. Landau and Zener [Yu88] reported that the transition probability is determined by the magnitude of the wave function and the shape of the diabatic curves at crossing point, which is some distance away from the equilibrium position. Since the covalent force is very short ranged, Yu [Yu87] assumes that in the region of crossing the covalent potential energy curve (i) is independent of R and the ionic potential energy curve (ii) is determined by the Coulombic attraction between M^+ and the negatively charged vacancy. At infinity the ionic curve (ii) lies above the covalent curve (i) by I-A, where I is the ionization potential and A the electron affinity of the cation vacancy. At the crossing

point the Coulomb potential exactly balances this energy difference. Hence the crossing distance R_c simply equals $(I\text{-}A)^{-1}$ in atomic units.

In Eq. (35) P^+ depends directly on the velocity at the crossing point R_c, which is related to the emission energy E_1 through the energy conservation by

$$v(R_c) = \left[\frac{2\,(E_1 + I - A)}{m}\right]^{1/2} \tag{36}$$

where m is the mass of the sputtered atom (the isotope mass). From Eqs. (35), (36) it is indicated that, at very low emission energy E_1, the P^+ converges to a constant value corresponding to

$$v(R_c) = \left[\frac{2\,(I - A)}{m}\right]^{1/2} \tag{37}$$

For intermediate energies (few tens eV), P^+ approximates a power law dependence on E_1. At very high energy E_1, P^+ approaches an exponential dependence on $\exp(-\frac{v_0}{v_\perp})$, $v_\perp$: normal component of particle velocity and $v_0 \approx 10^7$ cm/s. In addition the model predicts that, P^+ will decrease linearly with the increase in the isotope mass. It is also obvious that the P^+ decreases rapidly (i.e. exponentially) with increasing ionization potential I . Yu [Yu87], [Yu86] demonstrated that a good agreement between the predictions of the bond-breaking model and experimental results for the dependence of the ionization probability P^+ on the atom's ionization potential I for 11 elements of the fourth period. Phenomenologically, the secondary ion yield I_M^+ of the atom M is the sum of the contributions from different bonding configurations i [Yu86], [Yu87] :

$$I_M^+ \alpha \sum_i f_i P_i^+ Y_i \tag{38}$$

Where f_i, P_i^+ and Y_i are the fractional concentration, ionization probability and partial sputtering yield of the M atoms bonded in the ith configuration. This model has been successfully applied to rationalize the oxygen enhancement effect observed in SIMS analysis where oxidation of metallic sample surface can enhance the secondary ion yield by several orders of magnitude over that obtained under rare gas ion bombardment on a clean metal surface [Ma87]. However, Wucher et al [Wu88] pointed out experimental the dependence of P^+ for Ta atoms sputtered from polycrystalline Ta on oxygen coverage is inconsistent with those obtained by band-breaking model, where $P^+ \alpha \exp(-\frac{v_0}{v_\perp})$. In fact, the band-breaking model is analogous to the electron tunneling model, with the valence band replaced by the level of the trapped electron in the cation vacancy. The comparison between these two models is found in more detail in ref. [Yu87].

- **Surface polarization model**

Williams et al. [Wi78] was the first proposed a local surface polarization model to rationalize oxygen enhancement of both positive and negative secondary ion yields emitted from the same ion-bombarded surface. When a metal surface is bombarded with oxygen, the oxygen atoms can be adsorbed on the surface or incorporated beneath the surface layer. The electric dipole moments of the metal- oxygen bonds hence orient both in and out of the surface. Williams and Evans [Wi78] have postulated that the existence of two types of site:

(i) an electron-emissive site giving high yields of negative ions and (ii) an electron-retentive site giving high yields of positive ions.

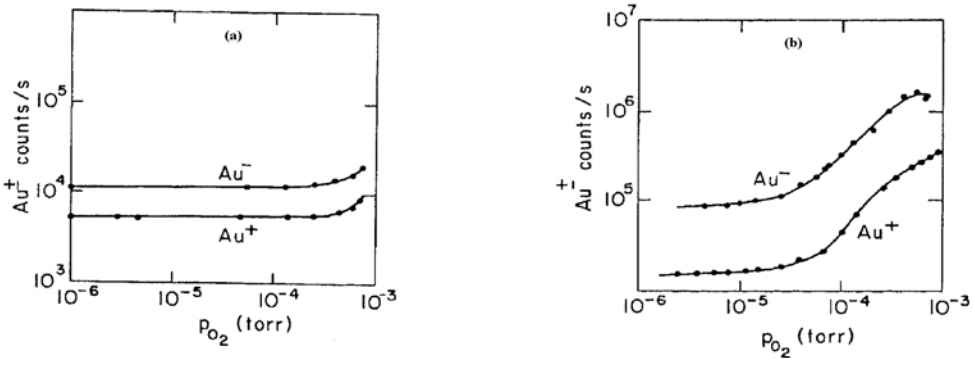

Figure 12: (a) Variation of Au^+ and Au^- yields with oxygen pressure under Ar^+ ions bombardment: Sample polycrystalline Au and (b) Variation of Au^+ and Au^- yields with oxygen pressure under Ar^+ ions: Sample Au-Al alloy [Wi78].

As a consequence, the adsorption of oxygen on the surface leads to create an electron-retentive site that favors the emission of positive secondary ions. In addition, the incorporation of oxygen beneath the surface creates an electron-emissive site that favors the emission of negative secondary ions. This model was used to explain why during the sputtering of Al- Au alloys under Ar^+ ions bombardment in the presence of oxygen [Wi78], the oxidation of Al enhanced the emission of Au^+ and Au^- ion yields. The Au^+ is assumed to be at the electron-retentive sites, while Au^- was formed at the electron-emissive sites. It should be noted that in the absence of aluminum the enhancement of Au^+ and Au^- ion yields is not observed (Fig. 12).

4 Experimental

4.1 Experimental setup

4.1.1 General description

The experiments are performed using a laser post-ionization reflectron time-of-flight mass spectrometer, the working principle of which will be described below. All components are housed in an ultrahigh vacuum chamber with a base pressure of several 10^{-9} mbar. A schematic drawing of the experimental arrangement is displayed in Fig. 13.

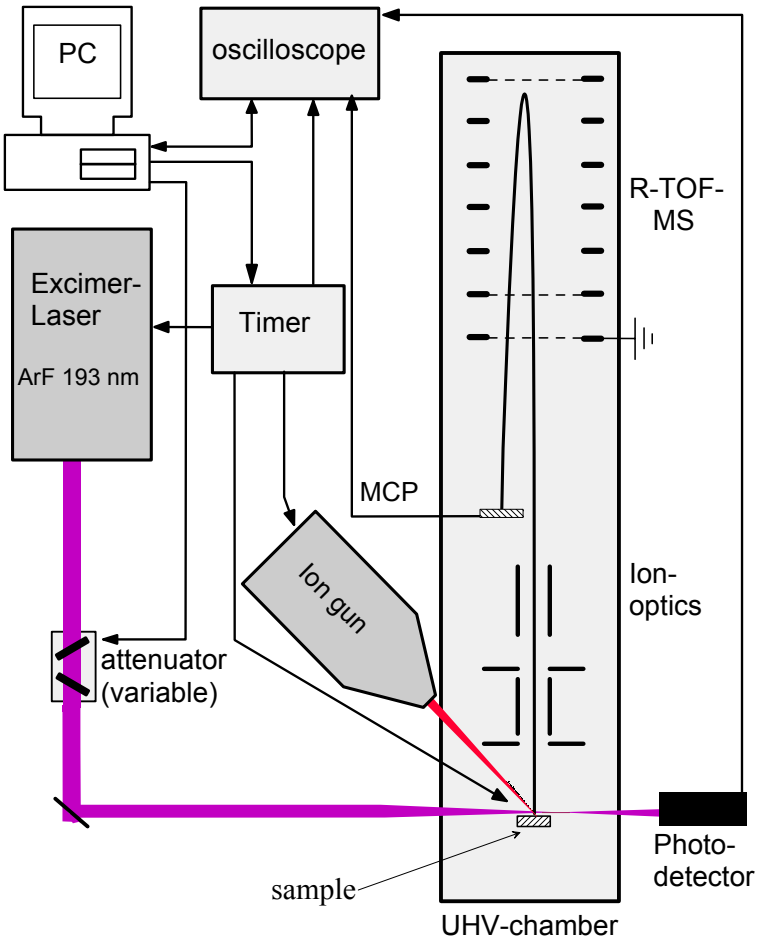

Figure 13: Figure 13: Schematic setup of TOF-SNMS-Laser- system

The system comprises of the following main parts :

- An ion source is generating projectile ions.
- An excimer laser used to post-ionize the neutral species that are sputtered from the bombarded surface.
- A time-of-flight mass spectrometer (TOF-MS) used to detect and analyze the sputtered species.

The investigated sample surface is bombarded with projectile ions generated by an ion source that is operated with different gases (Xe, SF_6 and SF_6/Ar). Mass separation of projectile ions is performed by means of a Wien filter. The primary ions impinge onto the surface under 45° with respect to the surface normal. Neutral species sputtered from the sample surface under different projectile ions bombardment are post-ionized by an intense UV laser beam at a wavelength of 193 nm. The ions produced by the photo-absorption process are swept into a reflectron time-of-flight (TOF) mass spectrometer by means of a pulsed electric field that is switched on about 20 ns after the ionizing laser. Secondary ions are detected by simply switching the ionization laser off and leaving the remainder of experiment unchanged. After the sputtered species are separated by TOF-MS, it will be detected by means of a Chevron stack of two microchannel plates (MCP) operated at an acceleration voltage (gain voltage) ranging from 1800 to 2200 V. The output MCP signals are converted to voltage and detected as a function of flight time by a digital oscilloscope. The resulting trace is stored in the computer where it is converted from a time-of-flight spectrum to a mass spectrum using the dependence $t\alpha\sqrt{m}$. The timing sequence between the different pulses (primary ion, target potential and ionizing laser) will be steered by a digital pulse generator. More details about the system components will be given in the following Sections.

4.1.2 Sample chamber

The sample chamber is made of a spherical high-grade steel recipient with a diameter of 20 *cm*. The chamber flanges are attached with, the time-of-flight mass spectrometer, ion source, sample manipulator, Quartz inlet window for laser radiation and turbo-molecular pump. In addition a CCD-Camera has been mounted on a conventional glass window in order to observe, adjust the target surface and the impact point of primary ion on the target surface. The investigated sample is mounted on a target holder fixed on a manipulator. The sample can be adjusted along axle (x) with accuracy of 0.1 *mm* and in two directions (y, z) perpendicularly to it with an accuracy of 0.01 *mm*. Likewise the sample is rotated around its longitudinal axis with an accuracy of 0.1°.

4.1.3 Vacuum system

The Pumping system consists of a rotary vane pump (Varian SD 301) working as forepump and a turbo-molecular pump (Leybold Heraeus Turbovac 450,

pumping speed 450 l/s) that is connected to the bottom part of the chamber. Additionally, differential pumping of the ion source by a small turbo-molecular pump (LH Turbovac 50) is provided. The residual gas pressure amounts to about $2-3\cdot10^{-9}$ mbar rising to $6\cdot10^{-9}$ mbar during the operation of the ion source.

4.1.4 Ion source

In order to sputter species from the target surface a commercial cold cathode plasma ion source (Type WF 421) developed by Wittmaack [Wi77] and marketed by Atomika company was used. As operating gases can be used O_2, H_2 and all noble gases. In the present experiments the ion source was operated with either monatomic gases Xe or polyatomic gas SF_6, as well as with a gas mixture of Ar/SF_6. Special advantages of such kind of the ion sources are:

i) It was designed to operate with noble and chemical reactive gases, in particular oxygen

ii) Low operation pressure within the ion source itself (typical $6\cdot10^{-6}$ mbar or less). Because of this, the gas load in the analysis chamber is drastically reduced in comparison to load imposed by ion source such as a duoplasmatron. This means that the pumps in a UHV system will not be overloaded even under long term operation of the source with noble gases.

iii) Consumables such as the cathodes, anodes and apertures are easily replaced through the rear flange without disassembling the ion source. In addition a gate valve in the beam line allows for such maintenance to be performed without venting the vacuum chamber on which the ion source mounted.

In order to control and adjust the rate flow of feed gas that passes to the plasma container in the ion source a regulator valve (UDV 135 Balzers) has been used. The gas pressure in the differentially pumped source volume is monitored by a vacuum gauge (Ionivac IM210). From the measured pressure ($P_2 = 5{\cdot}10^{-6}$ mbar), the known diameter ($d = 0.5$ mm) of the aperture between the plasma chamber and source volume and the pumping speed of the connected pump ($S = \frac{10l}{s}$) one can estimate the pressure in the plasma chamber (P_1) by:

$$(P_1 - P_2)\cdot C = S\cdot P_2 \Longrightarrow P_1\cdot C = S\cdot P_2 \tag{39}$$

where C the conductance through the aperture: $C = \frac{5l}{scm^{-2}}(\text{for Xe})\cdot\frac{\pi d^2}{4} = 98\cdot10^{-4}\frac{l}{s}$. Then $P_1 = \frac{S}{C}\cdot P_2 = 5\cdot10^{-3}$ mbar

The construction of the ion source is shown in Fig. 14, it consists of:

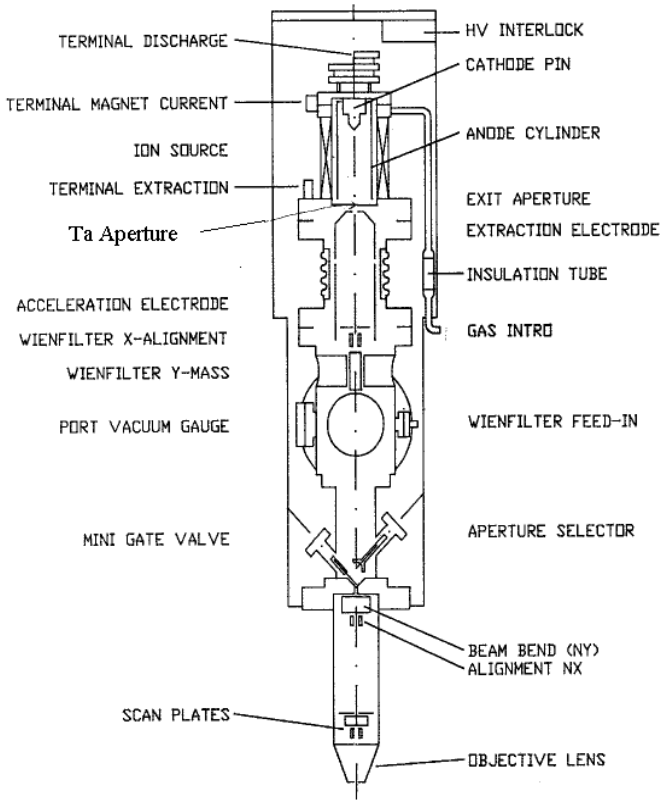

Figure 14: Schematic drawing of the ion source

i) Plasma ions generator (cathode, anode and discharge voltage)

ii) Extractor electrode

iii) Acceleration voltage

iv) Wien filter (mass ions separator)

iiv) Objective lens

The operating mechanisms of the ion source are described as follows: The ions are produced in a DC gas discharge that burn between a cathode (which looks like a pen) and a cylindrical anode surrounding the cathode. Additionally a permanent magnetic field provides for confinement of the plasma electrons. Likewise the electrons produced in the gas discharge are accelerated not directly on the anode due to the magnetic field, but a spiral course around the magnet field lines. This increases the residence time of electrons in plasma, therefore increasing the probability of producing further ions by electron impact ionization. The entire discharge is sustained by means of a high voltage of several hundreds volts. The generated ions are extracted by extraction voltage through

a tantalum aperture with a hole diameter of 0.5 mm. After long operation time the hole diameter of tantalum aperture will be increased that observe by instability in plasma and the increasing of discharge voltage therefore it has to be replaced by a new one. Extraction and acceleration electrode form a first electrostatic lens which is used to focus the extracted ions beam onto the aperture behind the Wien filter, in which the mass separation is accomplished. Fig. 15 shows typical values of Wien filter deflection voltage, which have been used to separate the components of projectile ions of SF_6 and Ar/SF_6.

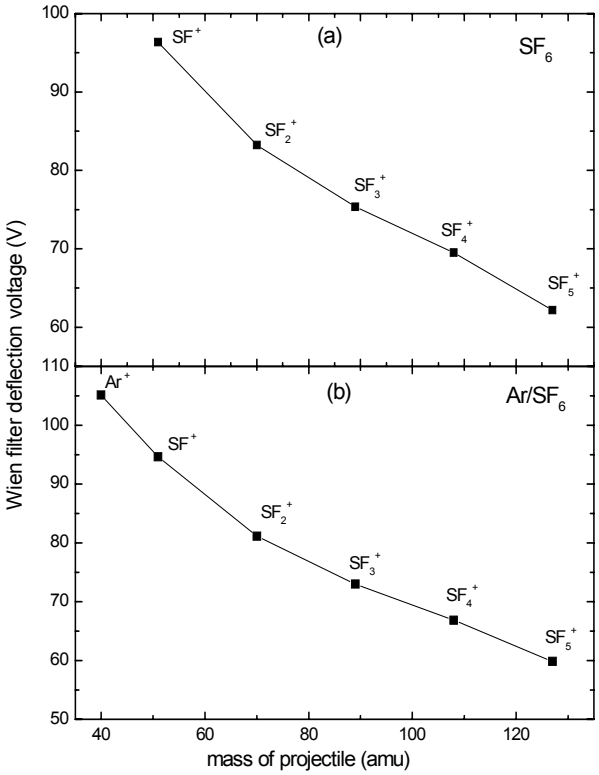

Figure 15: Wien filter deflection voltage as a function of projectile mass, in (a) and (b) the ion source was operated with SF_6 and Ar/SF_6, respectively.

In addition, by the Wien filter, it is possible to operate the ion source in a pulsed mode, using a fast switch (Behlke, Type HTS 31 GSM push-pull) that sets the duration of primary pulse bombardment. The bombardment pulse length is typically several of μs at a repetition rate of 10 Hz. Behind the Wien filter there is a mechanical aperture selector which can be used to vary the

diameter of the ion beam onto the sample surface and the bombardment spot size. To focus the ion beam, a second electrostatic lens (objective lens) is placed at the tip of the ion source.

Some notes on operating parameters of Atomika ion source :

- The magnitude of beam ion current drastically depends on stability of the ion generating plasma.

- The ion generating plasma is more unstable when the ion source is operated with pure SF_6 gas as compared to noble gases (Ar, Xe,...). This effect has been observed in plasma physics (instabilities in low pressure electronegative plasma). These observations suggest that the instability process is linked to the electronegativity since the discharge oscillates between higher and lower electron density states [Ch001], [Co003].

- When SF_6 is used as feed gas in the ion source, a cover of fluoride species are formed on anode due to reactivity of fluorine. Therefore the anode cylinder exhibits an insulating ring in the vicinity of the tip of the aluminum cathode and also an insulating layer near the top of the anode. The same phenomenon has been previously observed by Reuter and coworkers [Re88b], as well as Gillen [Gi003] who suggested that all source components are nickel-plated to reduce the attack by reactive fluorinated species.

In order to get more pressure stability and permit a rapid switching between different projectiles, the ion source is operated with a gas mixture of Ar/SF_6. The desired projectiles are then selected by means of the Wien filter. Typical operating parameters of the ion source with different operating gases are represented in the following table:

Gas	Xe	SF_6	Ar/SF_6
E (keV)	10	10	10
U_{ext} (V)	578	793	913
U_{obj} (kV)	8.2	8.1	7.3
P_2 (mbar)	$6 \cdot 10^{-6}$	$6 \cdot 10^{-7}$	$3 \cdot 10^{-6}$
I_m (A)	2.5	2.2	2.5
I_d (mA)	3	2.8	3
V_d (V)	650	650	660

Where U_{ext}: extraction voltage; U_{obj}: objective lens voltage; P_2: pressure in the differentially pumped source region; I_m: magnet current; I_d: discharge current; V_d: discharge voltage.

4.1.5 Target surface

The targets are a polycrystalline (silver and indium) sheets, specified by the manufacturer as 99.95% pure, introduced into the ultrahigh vacuum chamber after cleaning for few minutes in an ultrasonic bath containing isopropanol. The samples are sputter cleaned by dc ion bombardment prior to the data acquisition of each mass spectrum.

4.1.6 The actual target current

Primary ion currents of the order of nA were routinely measured by a digital multimeter with an inner resistance of 10 MΩ. This means, a current of 1 nA corresponds to a voltage reading of 100 nV. This is also the target potential which persists during the measurements. If that potential becomes significant, it acts to reduce the measured current due to the fact that secondary electrons released as a consequence of the ion bombardment are kept from leaving the surface.

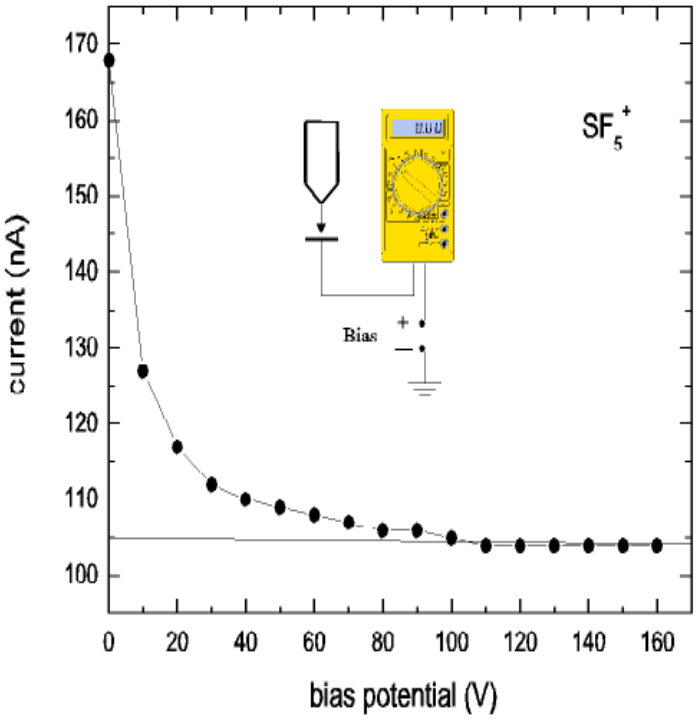

Figure 16: Measured target current as a function of bias potential.

If we want to exactly determine the magnitude of the primary ion current, the secondary electrons emitted from the target surface after bombardment

with energetic ions must be taken into account. For this reason, the actual ion current was estimated from target current measurements at variable positive bias potentials on the target to suppress secondary electron emission (Fig. 16). From Fig. 16, it is seen that the measured total current is rapidly decreasing with increasing the bias potential, until level off at saturated value i.e. the current magnitude becomes a constant with an increasing in bias potential. This ensures that the emitted secondary electrons are completely kept from leaving the surface. The actual ion current (I_P) is equal to the difference between the measured total current and secondary electron current (I_e). In the present work, it is found out that the actual ion current is lower than the total current by 25 % for monatomic ions (Xe^+) and 37.5 % for polyatomic projectiles SF_m^+ ($m = 1, ..., 5$). From these values, the ion induced electron emission yield (γ_e) can be determined as follows: the measured current I=I_p+I_e = 168 nA, the I_e obtained by extrapolating the curve in Fig. 16: I_e = 63 nA, therefore I_p = 105 nA $\Longrightarrow \gamma_e = \frac{I_e}{I_p} = \frac{63}{105} = 0.6$

4.1.7 Laser system

The sputtered neutral species that emitted from the bombarded surface will be post-ionized by an UV laser beam generated by a Commercial Excimer Laser (Lambda Physik, LPX 120i). An excimer laser is a pulsed gas discharge laser, which produces optical output in the UV region of the spectrum with different wavelengths depending upon the kind of gas filling. The name excimer comes from excited dimer that a diatomic molecule which exists only in an excited state, since the initial state does not exhibit potential minimum and it therefore not stable (Fig. 17). The dissociation upon relaxation from excited to ground state is automatically generating the population inversion necessary for laser action.

The active medium of an excimer laser is a mixture of rare, a halogen and a buffer gases. The gas mixture is rapidly recirculated across electrodes where a high voltage is applied to excite the gas molecules. The relaxation of the molecule from an excited state releases high intensity photons at a certain wavelength, two finely polished mirrors reflect this light back and forth within the gas medium to maximize the intensity of beam. The duration of the extracted laser pulse is determined by the high voltage circuitry producing the electrical discharge and amount to about 10-20 ns. The output wavelength of an excimer laser can be changed simply by changing the gas mixture. The laser mirrors have to be replaced and frequently polished in order to obtain maximum output energy. The most commonly used excimers are krypton fluoride (KrF, 248 nm), argon fluoride (ArF, 193 nm), and xenon chloride (XeCl, 308 nm) as well as the very short wavelength of the fluorine laser (F_2, 157 nm). In the present work, the laser was operated at a wavelength of 193 nm corresponding to a photon energy of 6.4 eV. Typical energy output from the laser at this wavelength is 170 mJ/pulse. The chemical reactions are described as follows:

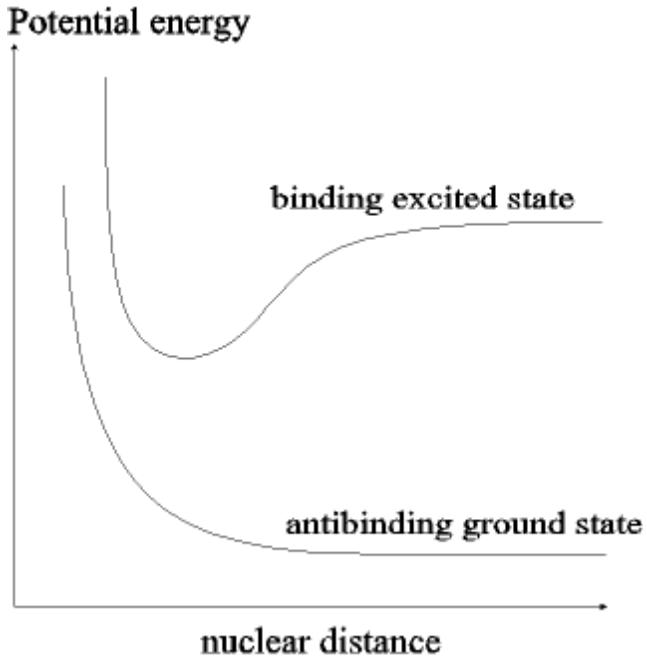

Figure 17: Schematic of potential energy of an excimer molecules.

$$\begin{aligned} \mathrm{R^+ + X^- + M} &\rightarrow \mathrm{RX^* + M} \\ \mathrm{R^* + X_2} &\rightarrow \mathrm{RX^* + X} \end{aligned}$$

where R the rare gas atom (argon), X the halogen atom (fluorine) and M an collision partner (called buffer gas, Ne or He) which exhausts the freed energy of the impact of R and X, and in such a way ensures that the formed molecules do not disintegrate again immediately. The actual laser transition is given by:

$$RX^* + \gamma \rightarrow R + X + 2\gamma$$

The excited ArF* molecule decays after several nanoseconds via emission of a photon into Ar and F. The components Ar and F are then available for another excitation cycle.

The spectral output of excimer lasers depend upon the specific gas filled and the selective properties of the laser resonator. In the simplest case of a free running excimer laser with a stable resonator, the spectral output is simply a property of the emission band of the excimer molecule. For ArF the output is a single peak with a width of approximately 500 pm. The relatively short pulse length leads to a high peak output power from excimer lasers. The following table contains the important parameters which we have set for using the laser:

gas filling	130 mbar halogen (5% F_2 in He), 250 mbar Ar,2620 mbar Ne
excimer	ArF*
pulse duration	$\sim$ 20 ns
repetition rate	10 Hz
discharge potential	24 kV

4.1.8 UV/VUV Detector

The laser pulse energy is measured by a UV/VUV detector, which was initially developed by D. Koch and described in his diploma thesis [Ko94]. The operation principle of the detector is based on the outside photoelectric effect at a solid cathode surface. The photo electrons released from a metal cathode are extracted towards an anode that is designed as a highly transparent grid. Then photoelectron current is detected as a voltage pulse across a 50 Ω termination resistor by means of an oscilloscope.

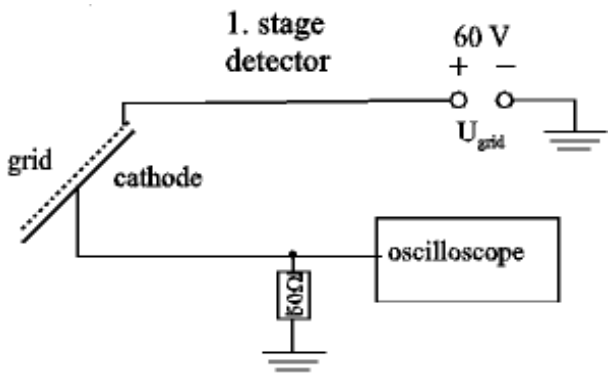

Schematic setup of photoelectric UV/VUV detector.

In order to reduce the space charge limitation of the electron current emitted at high energies M. Wahl has added another stage, where the light reflected by the cathode of first stage hits the cathode of the second stage. By this modification, the detection power range was drastically expanded. Therefore, the pulse laser energy can be measured over several orders of magnitude. The construction and characteristics of two-stage UV/VUV detector are described in more detail in [He96].

4.1.9 Optical components

In order to focus the laser beam over the sample, a planar -convex calcium fluoride (CaF_2) lens has been used. CaF_2 was used since this material has a particularly high transmission for ultraviolet light. Its focal length is about

23 cm at a wavelength of 193 nm. The lens is mounted on a vertically and horizontally adjustable rider, which can be adjusted with an accuracy of about 0.1 mm. To study the dependence of the photoion signals on the intensity of the ionizing laser, the laser pulse energy can be reduced in a controlled fashion by a stack of two variable dielectric attenuators located in front of the lens, which were tilted in opposite directions to compensate the beam walk off with increasing tilting angle. The transmission of the attenuators depends on the impact angle of the radiation. With a stepping motor controllable by a PC, the attenuators can be rotated moving in opposite directions around the same angle against the laser beam. By this method we are able to vary the laser beam intensity by several orders of magnitude.

4.2 Time-of-flight mass spectrometer (TOF-MS)

The principle of a time-of-flight mass spectrometer is based on the fact that particles, which have different masses and are accelerated in the same electric field, need different times to pass the same distance. In the simplest arrangement [Wi55] the flight pass is a single field-free drift zone of length L, and the flight time of a particle of mass m and energy E_{kin} is given by

$$t = \sqrt{\frac{L^2}{2E_{kin}}m}, \text{ hence } t\alpha\sqrt{m} \tag{40}$$

Here, $E_{kin} = E_0 + eU_0$ is the total kinetic energy, which is the sum of the initial energy and the gain eU_0 in the extraction field

Major advantages of this kind of mass spectrometer compared to others are: (i) It can take a complete mass spectrum in one single acquisition cycle. (ii) Unlimited mass range can be detected just by extending the flight time interval. This is particular advantageous for detection of large sputtered clusters. (iii) In contrast to quadrupole and magnetic sector analyzers, TOF transmission can be kept essentially constant even up to high mass resolution. [Br92] . The main disadvantage of a simple linear setup is the low mass resolution, which is given by

$$\frac{m}{\Delta m} = \frac{m}{(dm/dt)\,\Delta t} = \frac{t_{tot}}{2\Delta t} \tag{41}$$

where t_{tot} is the total flight time, Δt the temporal width of an ion peak registered at the detector. The most significant limitation to the mass resolution in a linear TOF setup is based on fact that secondary ions are not all emitted with the same energy but with a more or less broad energy distribution. Therefore, the ion initial energy distribution for ions of the same mass may cause a broadening of the ion packet as it travels from the sample to detector. As a consequence, ions emitted with low initial kinetic energy will trail behind ions of higher initial kinetic energy . It is obvious that the extent of the secondary

ion packet increases as the flight time/path increases, i.e. a longer flight path will actually not improve the mass resolution. In order to improve the mass resolution, Karataev et al. [Ka72] have developed an ion reflectron that consists of field-free drift regions combined with electrostatic mirrors. The conceptually simplest setup, which is also utilized here, comprises of two drift regions and one reflector. In its simplest form, the ion mirror utilizes one electrostatic field to reflect sputtered ions in order to compensate negative flight dispersion of the drift path with respect to initial kinetic energy and to provide positive time dispersion. The schematic structure of such ion reflector is represented in Fig. 18.

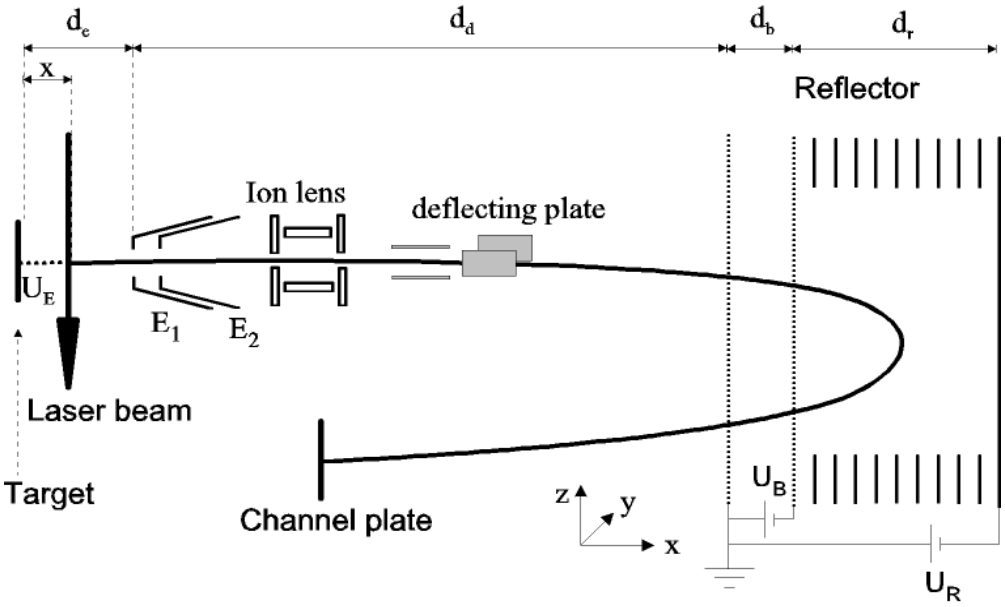

Figure 18: Schematically drawing of time of flight mass spectrometric detection of sputtered neutral, ionized atoms and clusters.

The dimensions of the present TOF apparatus are:

- extraction distance $d_e = 9.5$ mm
- drift distance $d_d = 650$ mm
- deceleration distance $d_b = 12.75$ mm
- length of the reflection distance $d_r = 102$ mm

The sputtered particles start from initial places (x_0, y_0, z_0) at a certain time t_0 with the energy E_0. In order to accelerate the sputtered particles towards the TOF, a high positive potential (U_E) of approximately 1.5 kV is

applied between target and first extraction electrode (E_1). In principle, the ion extraction optics is designed to allow a two-step extraction scheme involving two subsequent accelerating fields. This is necessary if the spectrometer is used in the so-called Wiley-Mclaren mode with one linear drift path. In the course of the present work, however, this option is not used and both extraction electrodes E_1 and E_2 are kept at ground potential. The ions are allowed to drift in two field-free regions of the total length d_d. To optimize the flight path, one electrostatic ion lens and two pairs of deflecting plates are used. Afterwards the sputtered particles pass the retarding field U_B and finally turn around in the reflection field U_R. The reflector consists of a number of metal rings, which are connected over resistors to produce a homogeneous electric field. By reflector and decelerating fields, the sputtered ions will be again accelerated to their original drift velocity to pass the second field-free zone on their way to the detectors.

In an idealized case the sputtered particles that have the same mass would appear in the TOF spectrum at the same time, but in the experiment this case is more complicated due to the fact that particles do not start from the same place. Parallel to the target surface (y, z) only particles, which are approximately situated below the circular opening of the extraction electrode E_1 can enter the TOF. A restriction of the direction perpendicular to the target surface (x) can be achieved by means of the flight time focusing properties of the spectrometer. The ions very close the surface ($x_0 < x_{min}$) pass through almost the total acceleration distance d_e and are not returned by reflector, but escape at the end of the reflector. The remaining ions, which are in a region $x_0 > x_{min}$ can reach the detector. x_{min} is thereby given by

$$\frac{d_e - x_{\min}}{d_e} \cdot U_E \leq U_R \tag{42}$$

However, the flight time strongly depends on the x_0 position (see Fig. 19). That means, the ions in area $x_0 >> x_{min}$ do not appear anymore in the actual peak, but are shifted up to higher flight times and contribute to the noise. The flight times of the particles passing through TOF subsections (Fig.18) are given by following equations [Wa91]:

$$t_e = \sqrt{\frac{2m}{e_0}} \frac{d_e}{U_e} \left(\sqrt{\frac{E_0}{e_0} + \frac{d_e - x_0}{d_e} U_E} - \sqrt{\frac{E_0}{e_0}} \right) \tag{43}$$

$$t_d = \sqrt{\frac{2m}{e_0}} \frac{d_e}{2\sqrt{\frac{E_0}{e_0} + \frac{d_e - x_0}{d_e} U_E}} \tag{44}$$

$$t_b = 2\sqrt{\frac{2m}{e_0}} \frac{d_b}{U_B} \left(\sqrt{\frac{E_0}{e_0} + \frac{d_e - x_0}{d_e} U_E} - \sqrt{\frac{E_0}{e_0} + \frac{d_e - x_0}{d_e} U_E - U_B} \right) \tag{45}$$

$$t_r = 2\sqrt{\frac{2m}{e_0}}\frac{d_r}{(U_R - U_B)}\left(\sqrt{\frac{E_0}{e_0} + \frac{d_e - x_0}{d_e}U_E - U_B}\right) \tag{46}$$

The total flight time of the sputtered particles from start position x_0 above the sample until they arrive at the MCP is given by

$$t_{tot} = t_e + t_d + t_b + t_r \tag{47}$$

The t_{tot} for particles with a certain mass m as a function of the start position x and the start energy E_0 can be calculated after input the values of different potentials (U_T, U_B and U_R). The results of the calculation for silver isotope mass ($m = 107$ amu) are represented in Fig. 19

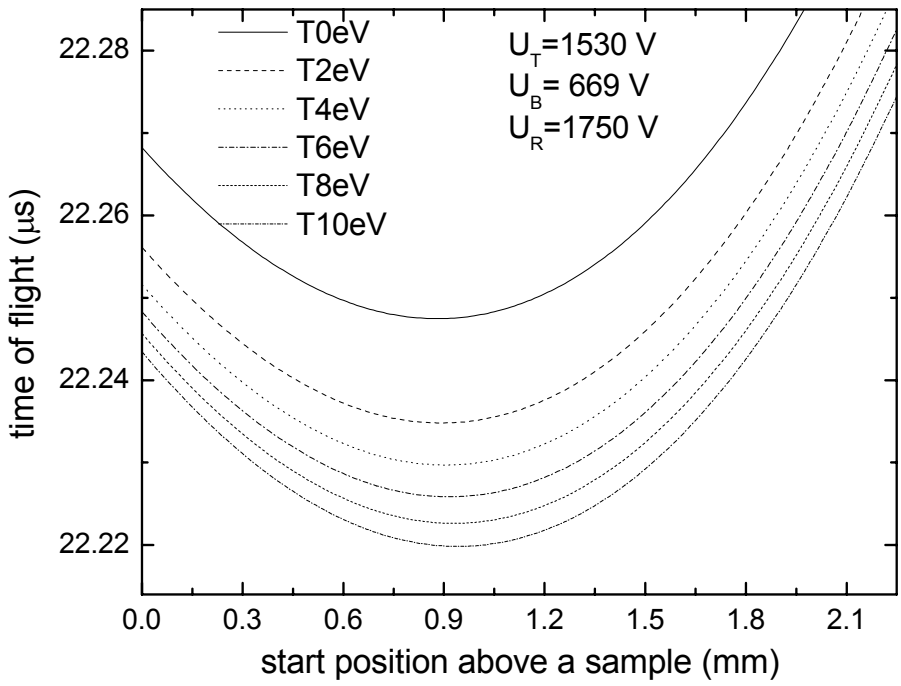

Figure 19: Flight time of extracted photoions across TOF spectrometer at different start energies vs. starting position along the extraction axis.

It is important to note that, the sputtered particles starting within a range around $x_0 = 1\ mm$ above the sample have very similar flight times. In this case the flight time is focused in first order, since its first derivative with respect to x is zero. If the second derivative vanishes, that means the flight time is

focused in second order (saddle point). In these experiments the time of flight mass spectrometer is operated only in first order focusing.

The TOF mass spectrometer has an acceptance range (A_{TOF})i.e., the range that sputtered particles can be accelerated into TOF and arrives at the detector. In the direction parallel to the sample surface (y), both locations as well as the extensions of A_{TOF} are determined by ion optical condition. In the direction along the surface normal, the range of acceptance depends on the potentials U_E, U_B and U_R that should be set on several values until obtaining a optimum mass resolution. In the case of SNMS measurements, the ionizing laser has to interact at a certain time with the sputtered particles. In this respect, the ionization volume i.e., the volume where the ionization laser interacts with the sputtered particles, must overlap with the acceptance volume of the MS. If saturation studies of the photoionization process are to be conducted (see below in section. 7), it must furthermore be ensured that the laser illuminates the entire acceptance volume with comparable intensity. If this condition is not fulfilled, so-called volume effects will appear upon variation of the laser intensity. That means the measured signals will increase with increasing laser intensity, even though the ionization process has already reached saturation in the center of the ionization volume, and, hence no saturation plateau like those visible in Fig. 26 will be observed. In principle, the size of the ionization volume can be determined by translating the tightly focused laser beam in directions along and perpendicular to the sample surface and recording the measured photoion signal as a function of the beam position. Such study has already been performed by Wahl [Wa95], on the same instrument as employed here. From this study, it has been demonstrated that the diameter of the sensitive volume has an extension of about 1 mm in all three dimensions.

4.3 Detection of the sputtered species

After the sputtered species are separated by TOF-MS, they are detected by means of a microchannel plate (MCP). MCP detectors are used in TOF-MS applications since they have a flat impact surface. Other Secondary Electron Multiplier (SEM) like the multi-dynode SEM or Channeltron have curved impact surfaces, generating a considerable impact time uncertainty [Gi2000a]. Essentially, an MCP is an array of continuous channels (secondary electron multipliers) oriented parallel to each other (Fig. 20a). The working principle of an MCP is based on the generation of secondary electrons, when the charged particles impinge with sufficiently high velocity at the input of the channel. The secondary electrons are accelerated by an electric field developed by a voltage applied across both ends of the MCP. They travel along the channel on parabolic trajectories until they in turn strike the channel surface, thus producing more secondary electrons. This process is repeated many times along the channel; as a result, this cascade process yields a cloud of several thousand electrons, which emerge from the rear of the plate (s. Fig. 20b). The gain of

the MCP detector is then defined as the average number of output secondary electrons per impinging ion. In the present work, two MCP behind each other have been used. Typically the plates are separated by distance of 100 μm.

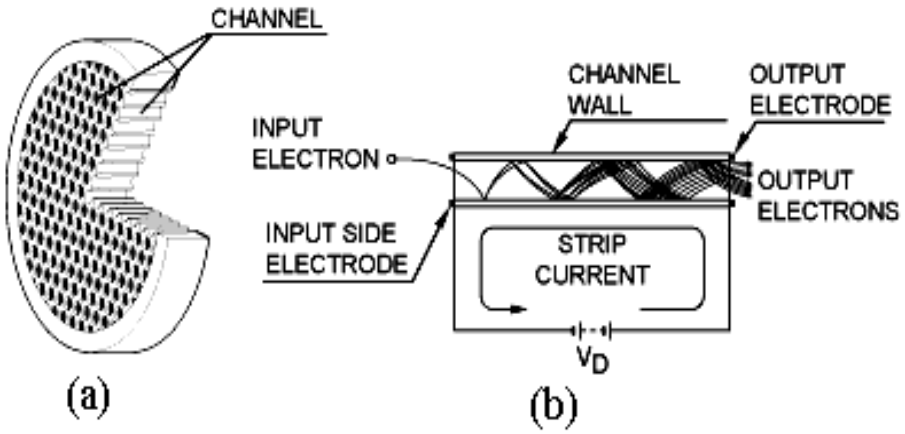

Figure 20: (a) and (b) cross section and multiplication process of MCP, respectively [Wi79b].

In order to obtain high gain output pulses, the MCP is assembled in Chevron arrangement mode. That means the channels of the two microchannel plates include a certain angle (typically 8°/8°). The concept behind this arrangement is to prevent positive ions produced at the output of the rear plate by electron impact ionization of residual gas atoms or by electron stimulated desorption from the channel walls from being accelerated along the channel and gain sufficient energy to generate a new cascade at the channel input. Such process would cause an electrical breakdown in the channel that could severely limit the dynamic range and as a worst case scenario destroy the detector. The gain of the MCP detector is determined by the applied voltage between both ends of the MCP. Typically the applied voltage is ranging from 1.8 to 2.2 kV.

At output side of the MCP, an electron collector made from stainless steel is installed. To create an accelerating voltage of 19 V between the output side of the MCP and the collector a 1 MΩ resistor is connected in series with the MCP stack. The voltage drop of about 19 V is generated due to bias current of 19 μA through the MCP stack. With the electron collector being at ground potential, and taking into account that the post-ionized ions are generated at 1 mm above the sample surface, the singly charged photoions strike the MCP surface with a total kinetic energy ranging from 3160 to 3560 eV (target potential 1360 V + gain voltage of MCP ranging from 1800 to 2200 V).

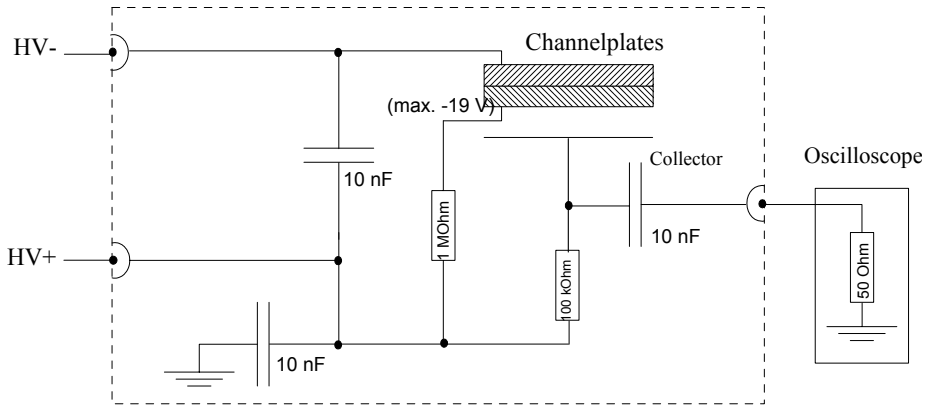

Figure 21: Schematic of MCP in Chevron arrangement

outside diameter	24.77 mm	electrode diameter	23.86 mm
sensitive diameter	18 mm	bias current	19 μA
border width	1.47	resistance	53 MΩ
pore size	10 μm nominal	time resolution	$\simeq$ 1 ns
electrode material	nichrome (80/20)	Max. Operating voltage	1000 V
center-to-center space	12 μm nominal	bias angle	$5^\circ \pm 1^\circ$

The specifications of the employed MCP's (Galileo: S1396)

The output current produced by the MCP is converted to a voltage by a 50 Ω resistor, which is then either recorded directly on a digital storage oscilloscope (analog detection mode) or fed into a discriminator (pulse counting mode). Time-of-flight mass spectra are recorded with a transient digitizer oscilloscope (LeCroy 9450) by averaging the recorded pulse spectrum over many instrument cycles (primary ion pulses and laser shots).

4.3.1 Analog mode

In the analog mode, the range of sputtered clusters detected will be small at most 8 atoms. That means, only atoms with a highest abundance of sputtered species will be recorded. It is well known in this mode that the observed MCP gain is determined by the ion-to-electron conversion efficiency upon impact of the ion at the front side of the detector and the secondary electron multiplication factor. Since the detected flight time peaks consist of many ions impinging simultaneously, the statistics of electron emission is not important and only average electron yields will be considered to describe the observed gain. According to the work of Seah [Se90], the observed MCP gain is given by

$$gain_{ana} = \gamma_1 \cdot \gamma^p \tag{48}$$

where $\gamma_1$denotes the average ion-induced electron emission yield at the conversion electrode, γ denotes the secondary electron emission at each of the subsequent amplification events and p is a statistical average of the number of electron induced amplification events at the channel wall. While γ_1 is determined by the detected ion species and the kinetic impact energy of the ions onto the detector, γ^p is solely determined by the MCP gain voltage and therefore independent of ion species and energy. Note that the factor γ_1 makes the MCP gain in principle dependent on the detected ion species.

4.3.2 Pulse counting mode

In the pulse counting mode, a discriminator is used as a single particle counter. The discriminator features a selectable minimum height of the accepted pulse (threshold limit about 1 mV). If an incident pulse is over the threshold limit, it will be converted into a standard TTL-pulse and recorded using the transient digitizer oscilloscope. If an incident pulse is under the threshold limit, it will be ignored. In this mode only single ion impact events are registered, hence, the statistics of the ion induced electron emission process become important. From ref.[St002] the formula describing the efficiency of secondary electron multipliers in this mode is given by a Poisson probability distribution

$$P\left(m, \gamma_1\right) = \frac{\gamma_1^m}{m!} \cdot e^{-\gamma_1} \tag{49}$$

where m is the number of electrons emitted per impact, γ_1 is the average ion induced electron yield as defined above. If we assume that every emission of at least one electron in the ion impact event will lead to a detected pulse in the discriminator, the detection probability is given by $1 - P(0, \gamma_1) = 1 - e^{-\gamma_1}$. The apparent detector gain in this operation mode is therefore:

$$gain_{pc} = \left(1 - e^{-\gamma_1}\right) \cdot \frac{\int U_{disc} \cdot dt}{50\Omega \cdot e_0} \simeq \left(1 - e^{-\gamma_1}\right) \cdot \frac{U_{disc} \cdot \Delta t_{disc}}{50\Omega \cdot e_0} \tag{50}$$

Typical values of γ_1 are of the orders of 1, $U_{disc} = 4$ V and $\Delta t_{disc} \simeq 10$ ns. Then $gain_{pc} = 0.63 \cdot \frac{4 \text{ V} \cdot 10 \text{ ns}}{50\Omega \cdot 1.6 \cdot 10^{-19} As} = 3 \cdot 10^9$.The apparent gain in the analog mode is given by

$$gain_{ana} = \frac{\text{average pulse height} \cdot \text{single pulse width}}{50\Omega \cdot 1.6 \cdot 10^{-19} As} = \frac{5 \text{ mV} \cdot \ 3 \text{ ns}}{50\Omega \cdot 1.6 \cdot 10^{-19} As} \simeq 2 \cdot 10^6 \tag{51}$$

The pulse counting mode therefore leads to a gain amplification factor :

$$F_{amp} = \frac{gain_{pc}}{gain_{ana}} \simeq 10^3 \quad \text{(crude estimate)} \tag{52}$$

The amplification factor (F_{amp}) between analog and pulse counting mode must be experimentally determined to compare the resulting yields measured in both modes. It should be noted that the amplification factor can be different for each

mass and depends on the microchannel plate gain voltage. From experimental data the amplification factor (F_{amp}) is determined by:

$$F_{amp} = \frac{S_x^{pc}}{S_x^{ana}} \tag{53}$$

Here S_x^{pc} is the integrated signal of species x in mass spectrum recorded in pulse counting mode and S_x^{ana} the same value in mass spectrum recorded in analog mode. The selected signals to determine the F_{amp} must be :

i) Detectable with enough signal-to-noise in analog mode

ii) Detectable in pulse counting mode, i.e. less than one ion of that mass produced per instrument cycle (primary ion and laser shot)

The latter condition is examined by inspecting the TOF peak of the selected mass in pulse counting mode averaged over many instrument cycles. The criterion is that the peak maximum in the averaged spectrum must be significantly below the standard TTL pulse height of about 4V. In practice, signals with peak maxima above I V were discarded.

Note that the acquisition of TOF spectra is different between both detection modes. In analog mode, a complete TOF or mass spectrum can in principle be acquired in one single instrument cycle (projectile ion and laser shot), the sensitivity being only limited by the signal to noise ratio. In pulse counting mode, on the other hand, a single instrument cycle leads to a recorded TOF signal which features a few standard TTL peaks. In this mode, a TOF spectrum is only generated by averaging the recorded signal track over many instrument cycles. The signal height detected in such a spectrum represents the probability to detect an ion in the time interval Δt_{disc} around a specific flight time, multiplied with the standard TTL pulse height.

4.3.3 Saturation of microchannel plates and blanking

Saturation of microchannel plates occurs when many particles with the same mass impact simultaneously on MCP, therefore the electron flow in the channels of MCP becomes too large and the gain of the MCP breaks down. This problem can be solved either by a reduction of the gain voltage or through blanking of major components from arriving at the MCP, if minor components of the mass spectrum are to be detected. In the latter case the gain voltage does not have to be reduced. In order to blank the ion packets, a set of deflection plates (length 30 mm) is placed before the MCP. By means of a digital delay generator (Stanford Research Systems; DG 535) in combination with a fast HV switch (Behlke), it is possible to apply a potential exactly on time that deflect ions of a desired mass range. The blanked ions impinge onto the edge of the screen (opening diameter of 25 mm) and are not detected by the microchannel

plate. The necessary potential at the deflection plate is approx. - 900 V. By this method, it is possible to select the desired blanking interval in the TOF spectrum with a time resolution of the order of 100 ns.

Other kind of saturation occurs in pulse counting mode due to the fact that an average $\gtrsim$ 1 ion is detected per shot and temporal width of discriminator pulse (10 ns). The mass spectrum is averaged over N shots and each single ion peak has a standard height of 4V. If at any position in the TOF spectrum an averaged signal height of 4 V is detected, that means that there is an ion pulse on every shot and, hence, saturation will occur. As mentioned previously, the criterion is that the peak maximum in the averaged spectrum must be significantly below the standard TTL pulse height of about 4V. In practice, signals with peak maxima above I V were discarded.

5 Methodology of the measurements

5.1 Time synchronization

The most critical part of the TOF-SNMS technique is the ability to steer the timing of the different pulses. The duration of the primary ion pulse t_p and the relative delay time t_d between primary ion and ionizing laser pulse are the most important parameters in a TOF-SNMS measurement. In contrast to the conventional TOF-SIMS procedure where t_p determines the flight time and, hence, the mass resolution of the spectrometer, in the SNMS technique this quantity (t_p) has practically no influence on the mass resolution. Instead, the interplay between t_p and t_d determines the character as well as the magnitude of the measured SNMS signal [Wu001].To achieve accurate timing to a sub-ns scale, the temporal sequence of the different pulses necessary to record a mass spectrum is generated by a digital delay generator (Stanford Research Systems; DG 535). It has an internal trigger output T_0 with variable adjustable frequency (in our case set to 10 Hz) and four further delay outputs from A to D, which can be adjusted with respect to each other with a time resolution of $10^{-12}s$.

The four freely programmable outputs A to D of the digital pulse generator are set as follows: the target potential is switched with output C, the laser is triggered on the output D, the output B determines the end of the ion pulse and is adjusted relative to C, and the output A determines the beginning of the ion pulse and is varied relative to B in order to generate primary ion pulses of selectable length (A-B). As a consequence, the additional TTL output AB, going high on A and low on B, is utilized to trigger the fast switching device which actually generates the ion pulse. In order to generate a short pulse on the target a home built device forming a TTL pulse with variable duration triggered by the C output is used. The output C is also used for synchronization of the LeCroy 9450 oscilloscope that is used as a digitizer. The oscilloscope is controlled by a PC through a GPIB interface. After the oscilloscope has been initialized by commands from the computer, it performs the data acquisition and average the recorded spectrum over a selected number of instrument cycles. During data acquisition the computer waits until the acquisition complete flag is set by the oscilloscope, after which the time of-flight spectrum is transferred to the PC. Settings for A and B pulse outputs on the timed delay generator depend on the mass and energy of the projectile ions, because these settings are determined by their velocity. Typical values of time delay for the outputs (A to D) of the digital delay generator are:

A = B - 12 μs 12 μs duration of primary ion pulse

B = C- 3. 4 μs 3. 4 μs delay between end of ion pulse trigger and target potential trigger (for Xe^+ and SF_5^+)

B=C-2.8 μs for [Ar^+, SF_m^+ $m = 1, ..., 5$)]

C = T_0 + 320 μs arbitrarily set, value must be large enough

D = C- 1.98 μs laser trigger about 2 μs before target trigger.

The primary ion pulse length was chosen to be long enough to ensure that the measured signals did not increase with increasing pulse length, thus indicating that species of all emission velocities are present in the ionization volume and interact with the ionizing laser. Typically the primary ion length necessary to fulfil that requirement is several μs.

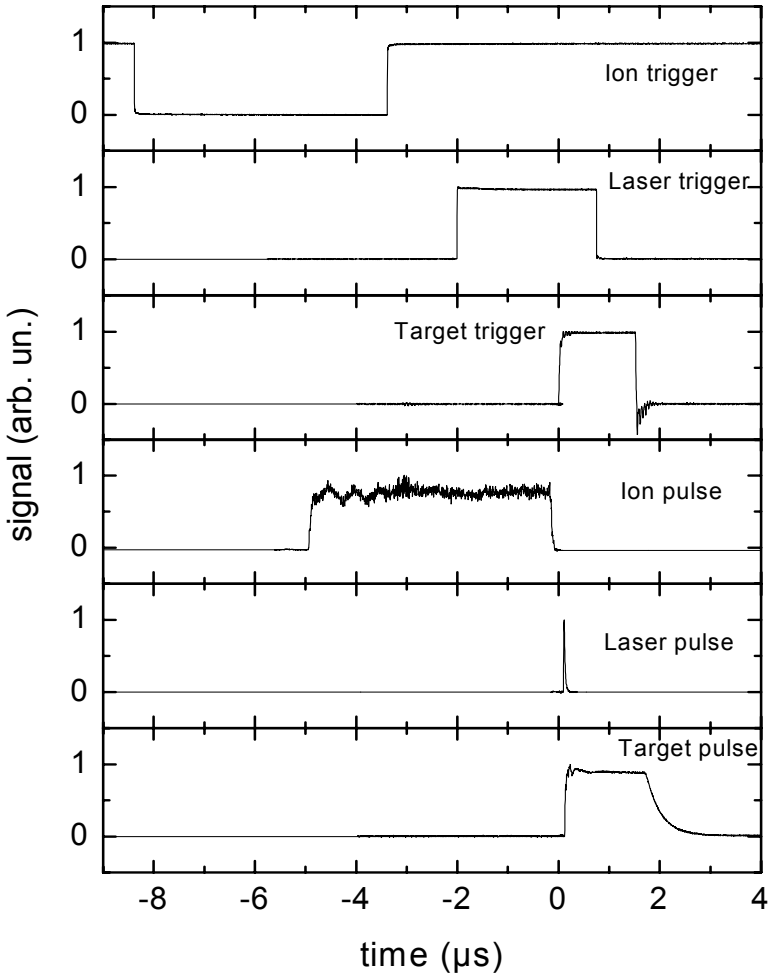

Figure 22: The timing sequence of the different pulses in TOF-SNMS measurements for Xe^+ at impact energy of 15 keV [Me001].

As mentioned above the setting of B depends on the mass and energy of projectile ions. This fact must be regarded here due to the use of different projectile ions. In principle, the time difference (C - B) must be adjusted to the projectile ion flight time between the ion gun pulsing plates and the

sample. This would ensure that the laser and target potential pulses are fired exactly at the end of the projectile ion pulse. For the sake simple switching between different projectiles, a fixed time delay of 3.4 μs (for the Xe^+ and SF_5^+ experiments on Ag) or 2.8 μs (for the Ar^+, SF_m^+ experiments on In and Ag) was applied in the present experiments. Due to the different flight times of the different projectiles, this may lead to either

- a shortened, projectile ion pulse length t_p^{eff} (effective length), if (C - B) is smaller than the actual ion flight time and, hence, the laser (and target potential) is fired before the end of the projectile ion pulse. In this case sputtered particles with emission velocities below $v_{min} = \frac{r}{t_p^{eff}}$ are discriminated from detection or

- a delay time t_d between the end of the projectile ion pulse and the laser (and target potential) pulse, if B - C is longer than the projectile ion flight time. In this case, sputtered particles with velocities above a maximum value $v_{max} = \frac{r}{t_d}$ are discriminated from detection, because these species will already have left the ionization volume at the firing time of the laser.

The detected signal represents an integral over the number density of the sputtered particles in the ionization volume located at distance r from the surface, i.e.,

$$S = \int_{v\,\mathrm{min}}^{v_{\mathrm{max}}} \frac{f(v)}{v} dv = \int_{r/t_p^{eff}}^{r/t_d} \frac{f(v)}{v} dv \tag{54}$$

Here, $f(v)$ denotes the emission velocity distribution of the sputtered particles. In principle, it is desirable to set $t_d = 0$ and t_p^{eff} long enough to contain all relevant emission velocities in the detected signal. For $r \simeq 1$ mm, typically $t_p^{eff} \simeq 2$ μs suffices [Wu001] to fulfill that condition. In this case, the integral in Eq. (54) practically extends from zero to infinity. With a non-zero value of t_d or too short values of t_p^{eff}, on the other hand, signal losses result, the magnitude of which depend on the actual values of the t_d, t_p^{eff}, r and the shape of $f(v)$. The timing sequence depicted in Fig. 22 was measured using the same experimental setup as employed here with 15-keV Xe^+ projectiles [Me001]. For these conditions, a setting of C -B = 3.4 μs apparently leads to perfect timing, i.e. $t_d = 0$ and $t_p^{eff} = t_p$. Based on this information, the values of the t_p^{eff}, t_d and the resulting values of v_{min} and v_{max} are calculated for different projectiles under the timing settings employed here. These values can now be employed to estimate the resulting signal losses. For that purpose, we insert the Thompson velocity distribution

$$f(v) \alpha \frac{v^3}{\left(v^2 + v_b^2\right)^3} \tag{55}$$

where v_b is a characteristic emission velocity :

$$v_b = \sqrt{\frac{2U_0}{m}} \tag{56}$$

Inserting the appropriate values for sputtered indium atoms (m = 115 amu, $U_0 \simeq Us$ = 2.6 eV) we find the detected signal fractions indicated in the last columns of the tables . It is seen that the signal measured under Ar^+ bombardment may be underestimated by about 50 %, for all other cases the possible signal loss is smaller than 10 %

At B = C- 3. 4 μs

projectile	t_f (μs)	t_p^{eff}	t_d (ns)	v_{min} ($\frac{m}{s}$)	$v_{\max}$ ($\frac{m}{s}$)	fraction
Xe^+	4.16	4.24	0	230	∞	1
SF_5^+	4.10	4.3	0	232	∞	1

At B=C-2.8 μs

projectile	t_f (μs)	t_p^{eff} (μs)	t_d (ns)	v_{min} ($\frac{m}{s}$)	$v_{\max}$ ($\frac{m}{s}$)	fraction
SF_5^+	4.1	3.7	0	270	∞	1
SF_4^+	3.78	4.0	0	250	∞	1
SF_3^+	3.43	4.3	0	232	∞	1
SF_2^+	3.04	4.5	0	222	∞	1
SF^+	2.6	12	200	83	5000	0.90
Ar^+	2.3	12	500	83	2000	0.50

An important question in this context concerns the time zero marking the start of the flight time measurements of the detected ions. For detection of sputtered neutral particles, two cases must be distinguished [Wu001]:

i) If the post-ionization laser is fired later than the pulse switching the extraction field on, the starting point of the flight time measurement is determined by the firing time of the laser, since this time marks the creation time of the detected photoions.

ii) If the ionization laser is fired before the ion extraction field is switched on, the starting point of the flight time measurement is given by the switching time of the extraction field rather than by the firing time of the laser. Under this condition, the temporal width of the laser pulse does not have any influence on the mass resolution, since the extraction potential is only switched on after the end of the laser pulse

By varying the delay time between C and D and recording the measured flight time of a particular ion species, one can therefore precisely determine exact synchronization of laser and target pulses by means of transition between cases i) and ii)

5.2 Method

In this section basic principles of measurements in the laser SNMS technique employed in the present work are described. The time-of-flight mass spectrometry TOF is employed here to detect and analysis both of secondary ions and neutral species sputtered from the bombarded surface. The main goal of such an experiment is to determine the ionization probability $\alpha^{+,-}$, i.e. the probability that a sputtered particle becomes ionized in the course of the emission process. Therefore, it is necessary to perform the detection of sputtered neutral species and the corresponding secondary ions under exactly the same experimental conditions with respect to detection sensitivity, accepted fractions of emission angle and velocity distributions etc. To achieve that purpose, the sample is bombarded with a pulsed ion beam, during the primary ion pulse the sample is held at ground potential in order to ensure that the spatial region between the surface and extraction electrode E_1 (Fig. 18) is field free. The sputtered neutral species are post-ionized by the laser which is fired immediately after the primary ion pulse. The resulting photoions are extracted by the electric field which is switched on shortly (about 20 ns) after the ionizing laser pulse. As discussed above this ensures that, the starting point of the flight time measurement is given by the switching time of the extraction field rather than by the firing time of the laser. Moreover, the use of this timing sequence ensures that the temporal width and the shape of the flight time peak recorded for particles of a particular mass are exclusively determined by the time refocusing properties of the reflctron TOF spectrometer and, in particular, do not depend on the temporal width of the ionization laser.

As mentioned previously (Section. 4. 2) the ionization volume must overlap with the acceptance volume of the TOF-MS. During acquisition of mass spectra of sputtered neutral species the laser beam was defocused such that the ionization volume is entirely determined by the acceptance volume of the mass spectrometer. By increasing the laser intensity, it is possible to determine a saturated signal of post-ionized neutral particles with neutral ionization probability $\alpha^0 = 1$ in case of single photon ionization (Indium sample). Due to the fact that the cross section dimensions of the laser beam $\geqslant 1$ mm the transportation of particles into and out of the ionization volume during the firing time of the laser pulse can be neglected. Therefore, in this case the measured signal is representative of the number density of sputtered neutral particles present within the ionization volume at the firing time of the laser.

For detection of secondary ions, the ionization laser is simply switched off, while all other parameters (ion bombardment, target voltage, TOF spectrometer settings, etc.) remain unchanged. In this case the experiment will detect the secondary ions that have been sputtered during the primary ion pulse (the extraction field was switch off) and migrated into the ionization volume. Since

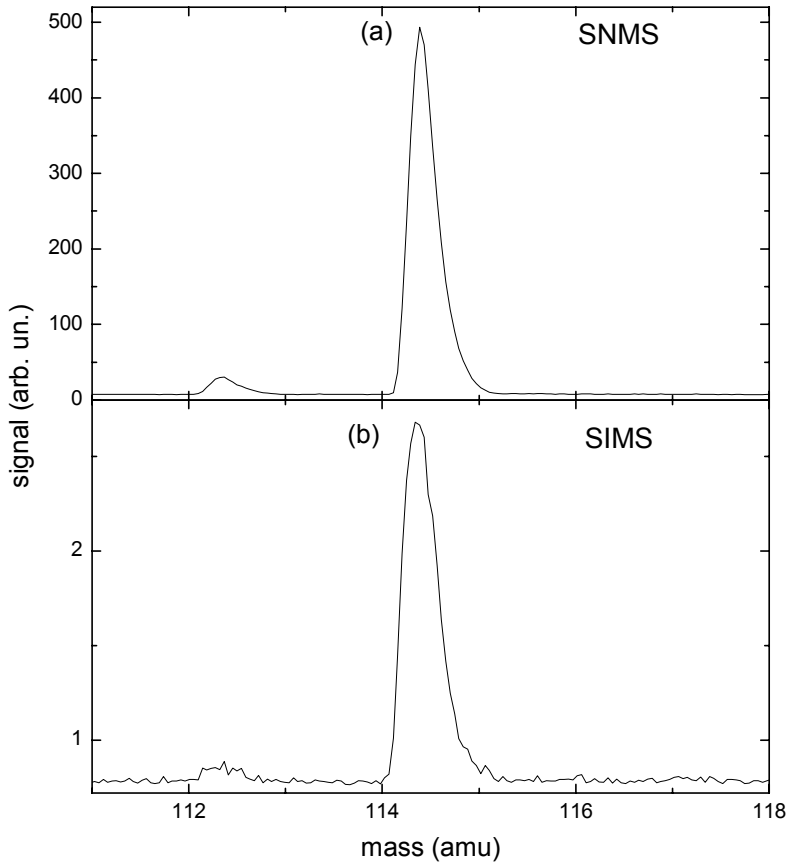

Figure 23: TOF-mass spectrum of sputtered indium atoms recorded (a) with and (b) without ionization laser.

the extraction region above the surface is originally field free, these ions emerge from the surface in the same way as the sputtered neutral particles. Upon switching the extraction field on, those ions present in the ionization volume are swept into the TOF spectrometer and are detected in exactly the same way as the post-ionized neutrals. It should be noted that the width of the time peaks of secondary ions measured in this way is independent of the primary ion pulse length, and one can therefore utilize long pulses of primary ions ensuring that the ionization volume is completely filled with sputtered particles (ions and neutral) of all emission velocities. Under these conditions, the measured ion signal is representative of the number density of secondary ions present within the ionization volume. Moreover, since the instrument cannot distinguish between post-ionized neutrals and secondary ions present within the

ionization volume, the transmission and detection efficiency of both species are identical. Under such conditions the ionization probability is directly determined from the ratio between the secondary ion signals (measured without the ionizing laser) and the saturated secondary neutral signals without any further correction. More details about the principle of this technique are found in refs. [Wu2000], [Wu001].

For comparison between SNMS and SIMS mass spectra Fig. 23 shows an example which was obtained on sputtered indium atoms. It is seen that the mass spectral characteristics of secondary ions and post-ionized neutral particles are identical. In particular the same microsecond long projectile ion pulse was used, a procedure which is in pronounced contrast to the generally employed operation mode of a TOF-SIMS spectrometer. Due to the delayed extraction mode applied here, the TOF signals exhibit the same, sharp flight time peaks as those of post-ionized neutrals. It is evident that the time resolution of the measured SIMS spectrum is solely determined by switching of the extraction field and has nothing to do with the projectile ion pulse length. Moreover, SNMS and SIMS spectra exhibit almost identical flight times and peak shapes, indicating a good spatial overlap of sensitive volume and ionization laser.

6 Photoionization

In this work, neutral atoms and clusters sputtered from a metal surface are ionized due to the interaction with ultraviolet laser irradiation. In the case of clusters, also photon induced fragmentation can occur. To describe the ionization and fragmentation process of sputtered atoms and clusters in a simple theoretical model [Wa94], only three different possible linear processes must be considered, which are:

- Ionization of a neutral cluster.
- Fragmentation of a neutral cluster after absorption of photons.
- Fragmentation of an ionized cluster by absorption of a further photon.

In the case of an indium sample, all sputtered neutral species can be ionized by absorption of a single photon. Hence, the ionization process can be easily saturated at moderate laser power density. The respective rates of single photon ionization are proportional to the corresponding interaction cross-section of the respective cluster and to the irradiating laser power density:

$$R_{I,F_\circ,F_I} = \frac{P_L}{h\nu}\sigma_{I,F_\circ,F_I} \tag{57}$$

P_L	:	laser power density
$h\nu$	:	photon energy
σ_I, $\sigma_{F_\circ}$, $\sigma_{_{F_I}}$	:	cross section for ionization, neutral and ionic fragmentation, respectively

For simplicity, the temporal laser pulse profile is assumed to be rectangular, i.e. during the laser pulse duration Δt the laser power density will be constant. In addition all higher order absorption processes are neglected in the present treatment. Then, the rate equations describing the number density of neutral ($\rho_\circ$) and positively charged clusters (ρ_I) within the volume of interaction between laser beam and sputtered species read:

$$\frac{d\rho_\circ}{dt} = -\left(R_I + R_{F_0}\right)\rho_\circ(t) \tag{58}$$

$$\frac{d\rho_I}{dt} = R_I\rho_\circ(t) - R_{F_i}\rho_i(t) \tag{59}$$

With the boundary conditions $\rho_\circ(t=0) = \rho_\circ$ and $\rho_I(t=0) = 0$, the differential equations 58 and 59 can be easily solved yielding

$$\rho_\circ\left(t\right) = \rho_\circ \cdot \exp\left(-\frac{\left(\sigma_I + \sigma_{F_\circ}\right)t}{h\nu}P_L\right) \tag{60}$$

and

$$\rho_I\left(t\right) = \rho_\circ \cdot \frac{\sigma_I}{\sigma_I + \sigma_{F_\circ} - \sigma_{F_I}} \cdot \left[1 - \exp\left(-\frac{\left(\sigma_I + \sigma_{F\circ} - \sigma_{F_I}\right)t}{h\nu}P_L\right)\right] \cdot \exp\left(-\frac{\sigma_{F_I}t}{h\nu}P_L\right) \tag{61}$$

the number of non-fragmented photoions created within the interaction volume ΔV during the laser pulse duration Δt, and hence the signal measured at a specific laser power density P_L, given by

$$S\left(P_L\right) = \rho_I\left(\Delta t\right) \cdot \Delta V \tag{62}$$

From given dependencies of the photoion signal (Eqs. 60 and 61), in special case, if no fragmentation occurs, i.e. $\sigma_{F_{\circ,I}} \ll \sigma_I$, that leads to the usual saturation behavior of a single photon ionization process according to

$$S\left(P_L\right) = \rho_\circ \cdot \Delta V\left[1 - \exp\left(-\sigma_I\frac{\Delta t}{h\nu}P_L\right)\right] \tag{63}$$

then:

$$S\left(P_L\right) = S_{sat}\left[1 - \exp\left(-\sigma_I\frac{P_L}{h\nu}\Delta t\right)\right] \tag{64}$$

where $S_{\ sat}$ is the saturation signal. In the present work we have two cases

(i) For neutral sputtered silver particles in particular atoms, dimers, tetramers and sexamers the energy of ionizing laser is not sufficient to permit single photon ionization of these species and, hence, the post-ionization process is not saturated. As a consequence, these species are ionized by two photon ionization absorption. In this case the $S(P_L)$ is given by

$$S(P_L)\,\alpha \exp -\sigma_I \frac{P_L^2}{h\upsilon}\Delta t \tag{65}$$

In order to calculate the sputtering yield the measured data must be corrected for the known post-ionization efficiency. Such data is found in ref. [Wa94] where the neutral sputtered silver particles have been post-ionized by a 157 nm VUV laser beam that has a photon energy of 7.9 eV.

(ii) For sputtered neutral indium particles, the laser power density is enough to drive photoion signals for all atoms and clusters to saturation mode. Therefore, the dependence of measured signal on laser power density will be in good agreement with Eq. (64), more details about this point are found in Section 7. 1. 2.

7 Results

In the present chapter the obtained experimental results will be presented. There are three main parts describing the investigations of the bombarded surfaces by mass spectrometry and by X-ray photoelectron spectroscopy (XPS).

Firstly, the formation of sputtered indium clusters under bombardment with Ar^+ and SF_m^+ ($m = 1, ..., 5$) ions is investigated. In order to obtain information about the relative abundance of clusters among the flux of sputtered particles independent of their charge state, mass spectra of both secondary ions and sputtered neutral particles were recorded. In these experiments, a photon energy of the ionizing laser (6.4 eV) at wavelength of 193 nm is larger than the ionization potential of indium atoms (5.79 eV) and all indium clusters. Therefore, the photo-ionization of all neutral species is achieved by absorption of a single photon (SPI) and, hence, a high ionization efficiency and low fragmentation rates have been achieved. It has been demonstrated that under these conditions the photo-ionization of sputtered neutral clusters can be saturated at moderate laser power densities, and the partial sputtering yields of clusters can therefore be determined from the measured data without prior knowledge of photo-ionization cross sections [Co91], [Wu93a].

Secondly, we expand our experiments to investigate other metal surfaces to understand the effect of reactive ion bombardment on the formation of sputtered clusters. In this case a silver surface has been investigated under bombardment with Xe^+ and SF_5^+ ions. The goal of these experiments is to determine the influence of the polyatomic projectiles SF_5^+ on the partial sputtering yields as well as to investigate the question whether the relative contribution of clusters in the sputtered flux is enhanced under SF_5^+ in comparison with monatomic Xe^+ ions. Expanding on this study, the role of fluorine projectile nuclearity in sputtering of silver has been investigated by bombarding the target surface under SF_m^+ ($m = 1, ..., 5$).

Finally, an X-ray photoelectron spectrometer (XPS) has been used in order to investigate the change of chemical state of metal silver subjected to SF_m^+ ($m = 1, ..., 5$) and to determine the concentration of fluorine at the bombarded surface as a function of the projectile nuclearity.

7.1 Sputtering from indium under bombardment with SF_m^+ ($m = 1, ..., 5$) and Ar^+ projectiles

In the present chapter, the experimental data on the formation of sputtered indium clusters under bombardment with SF_m^+ ($m = 1, ..., 5$) and Ar^+ ions will be presented. By comparing the secondary ion yields with those of the corresponding neutrals, it is possible to unravel the behavior of the partial sputtering yields and ionization probabilities as a function of the fluorine content and nuclearity of the projectile. Such information is needed in order to obtain a better understanding of the formation mechanisms of sputtered cluster ions under bombardment with chemically reactive polyatomic projectiles. Indium is selected as target material since:

(i) It is well known that, rare gas ion bombardment of an indium surface produces large amounts of In_n clusters [St002]

(ii) The photoionization of sputtered neutral indium atoms and clusters is easily saturated using single photon-ionization at a convenient wavelength of 193 nm [St002].

7.1.1 Experimental conditions

A polycrystalline metallic indium sample is bombarded under 45^o incidence with Ar^+ or SF_m^+ ($m = 1, .., 5$) ions at 10 keV impact energy. As mentioned previously (in Section. 4. 1. 4), the ion beam current generated by the plasma cold cathode ion source drastically depends on the conditions of the ion generating plasma which tends to be unstable when the ion source is operated with pure SF_6 gas. In order to achieve enhanced stability and permit a rapid switching between different projectile ions, the ion source is therefore operated with a gas mixture of 50% Argon and 50% SF_6 and the desired projectiles are selected by means of a Wien filter. Fig. 24 displays the spectrum of a gas mixture Ar/SF_6 that is recorded by means of a quadrupole mass spectrometer operated in residual gas analysis mode.

It is seen that, besides H_2O, Ar and SF_6 related fragments have been observed. In an attempt to determine quantitatively the contribution of different species in the gas mixture we have integrated the signal intensity of Ar^+ and SF_3^+, SF_4^+ and SF_5^+, respectively. The results are displayed in the following table:

species	Integrated signal
Ar^+	45
SF_5^+	61
SF_4^+	6
SF_3^+	9

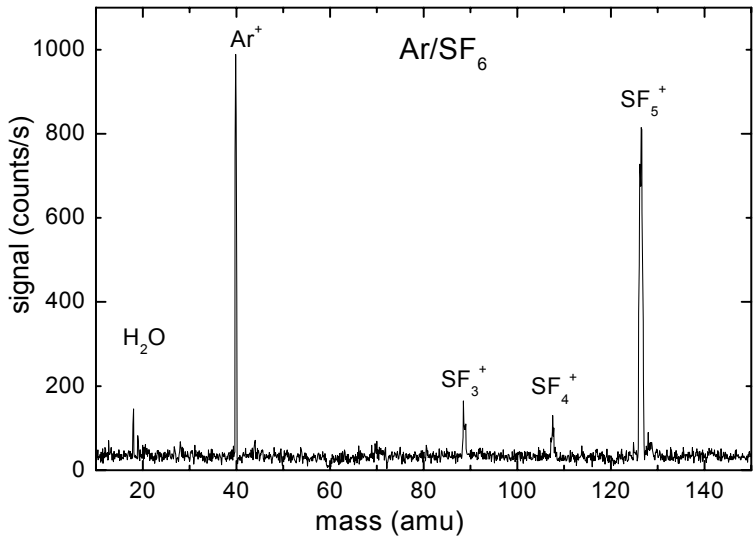

Figure 24: Spectrum of a gas mixture of Ar and SF_6 recorded by a quadrupole mass spectrometer. Vacuum pressure $5{\cdot}10^{-8}$ mbar.

It is well known that due to different cross sections for electron impact ionization each gas has a special gas correction factor (R_g) with respect to the standard gas (nitrogen). Therefore, the integrated signal is divided by 1.29 for Ar^+ and by 2.2 for the sum of all SF_m^+ species, where 1.29 and 2.2 the R_g values for Ar and SF_6 respectively [Ba83]. The abundance of Ar and SF_6 in a gas mixture is found to be 50% and 50% respectively. The typical ion currents of different projectiles that are delivered under these conditions are displayed in Fig. 25.

Under these conditions the ion source has been operated for long time (at least two months) without the need to change the cathode or anode, which have to be frequently replaced by new ones when pure SF_6 is used as feed gas. Other advantage of these conditions is the high stability of the produced ion currents due to the stability of the ion generating plasma in the ion source. More specifically, during operation time of four hours, the ion current is varied (higher or lower) in range of 5 % with respect to initial ion current. Note that the ion currents have been measured several times and it is found that in all cases the same behavior as displayed in Fig. 25 has been observed. The operation parameters of the ion source with a gas mixture of Ar and SF_6 is found in Section. 4. 1. 4.

From the projectile current spectrum (Fig. 25) some observations can be made:

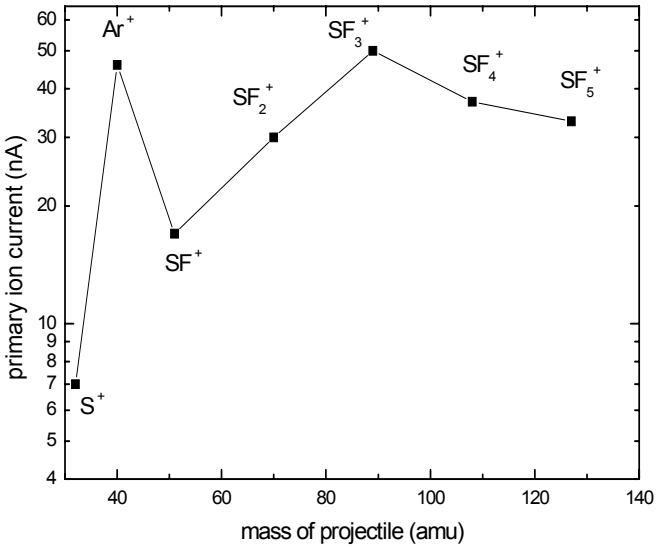

Figure 25: Projectile ion current delivered by the ion source operated with a mixture of Ar and SF_6 gas versus mass of different projectiles (Ar and SF_m^+ with $m = 1, ..., 5$) [Gh004].

(i) The SF_3^+ projectile has the largest primary ion current, while its apparent abundance in the gas spectrum does not exceed 6 %. This finding indicates largely different cracking patterns between the gas discharge operational in the ion source and in the electron impact of the residual gas analyzer. Hence, we must conclude that the ionization and dissociation processes occurring in the plasma are far more complicated than a simple electron impact process.

(ii) The summed projectile currents of SF_6 constituents are three times higher than the Ar current, although Ar and SF_6 are equally abundant in the gas mixture.

7.1.2 Dependence of measured signal on laser intensity

In order to determine at which laser power density the saturation of ionization process of post-ionized species is achieved, the dependence of measured signals on power density of the ionized laser was investigated. For this purpose, the laser pulse energy could be reduced in a controlled fashion focusing by a stack of two variable dielectric attenuators located in front of the lens (more details about the experiments procedure are found in Section. 4. 1. 9). The laser intensity was monitored either by a home made photoelectric detector (described in Section 4. 1. 8) that is mounted on the window of UHV chamber or directly by pyroelectric Joulemeter JD500.

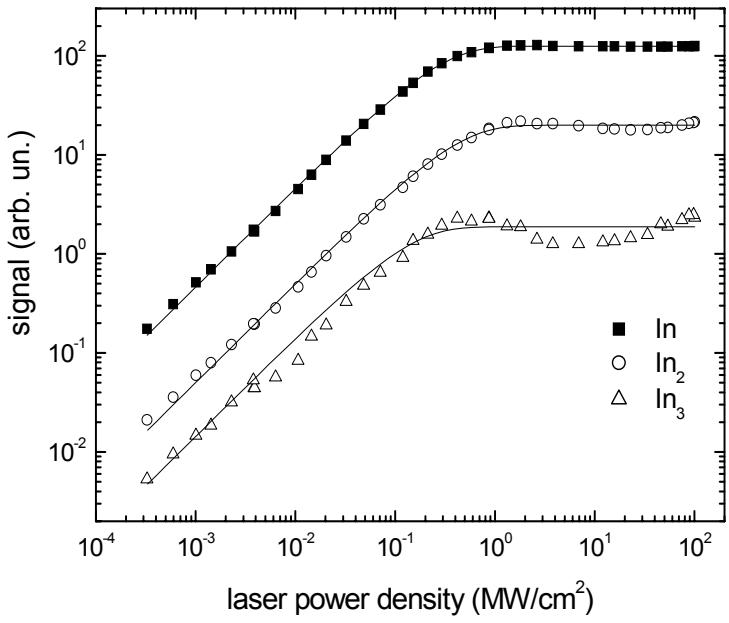

Figure 26: Integrated signal of post-ionized neutral In_n clusters versus power density of the ionizing laser. The indium surface was bombarded with 10-keV Ar^+ ions.

Fig. 26 shows the dependence of the measured integrated mass signals of sputtered neutral In, In_2 and In_3 on the peak power density of the ionizing laser. The latter values are calculated from the measured pulse energy by assuming a rectangular temporal laser pulse profile of 20 ns duration and a measured beam cross section of about 2.5 mm^2 in the interaction region located about 1 mm above the surface. As mentioned in Section. 6, the measured signal as a function of the laser power density should by given by :

$$S\left(P_L\right) = S_{sat}\left[1 - \exp\left(-\sigma_i \frac{\Delta t}{hv} P_L\right)\right] \tag{66}$$

From the saturation curves depicted in Fig. 26, it is seen that, in the regime of low laser power density P_L the measured signals increase linearly with increasing P_L, a behavior which is expected for a single photon absorption process according to Eq. (66). At power density values around or below 10^6 W/cm^2, the signals level off due to the saturation of the photoionization process. If the P_L is increased further, the measured signal is found to turn over and decrease again. This behavior can be attributed to the onset of multiphoton fragmentation processes which require the simultaneous absorption of more than one photon and can therefore be assumed to play only a minor role at low P_L. For dimers and trimers, it is apparent that the measured signals increase again at large power densities. This behavior is surprising because one would expect decrease of the measured signals with increasing P_L due to the fragmentation process. It is of interest to note that there is a nice plateau of the In signal over about 2 orders of magnitude in P_L .Thus indicating that the volume effects are absent and cluster signal increase can only be induced by signal contributions from multiphoton fragmentation (dissociative ionization) of larger sputtered clusters. By applying a least squares fit of Eq. (65) to the measured data, the saturated signals S_{Sat} and the photo absorption cross section σ_i can be obtained as fitting parameters. The resulting fit curves are included in Fig. 26 as solid lines and the corresponding values of the single photoabsorption cross section are displayed in the following table :

Indium atoms	photoabsorption cross section σ_i (cm^2)
In	1.7x10^{-16}
In_2	1.2x10^{-16}
In_3	3.6x10^{-16}

Interestingly, it is found that the photoabsorption cross section of indium atoms is larger than that of dimers. This behavior is quite different from that observed for other sputtered metal clusters [Wu96]. Staudt [St002] has previously made the same observation in a similar study. The reason for the unexpected ordering of the cross sections is not clear at the present time.

7.1.3 Neutral clusters

Mass spectra of post-ionized neutral atoms and clusters that are sputtered from a clean polycrystalline indium surface under bombardment with 10-keV Ar^+, SF_5^+ SF_4^+, SF_3^+, SF_2^+ and SF^+ projectiles are illustrated in Fig. 27.

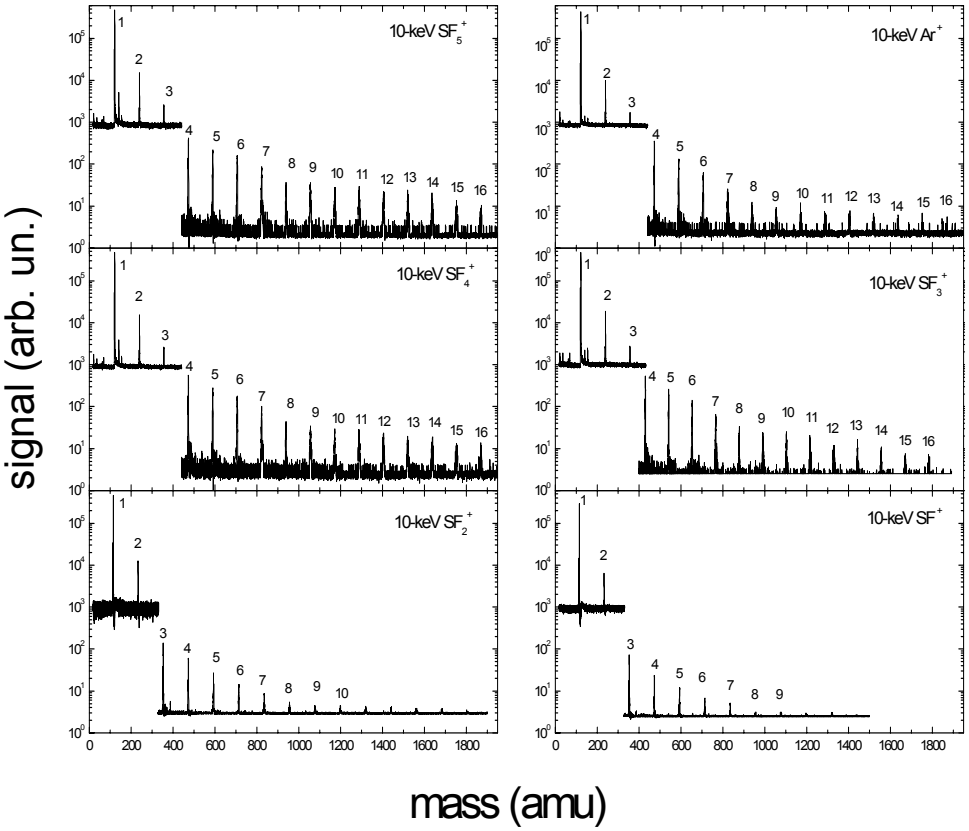

Figure 27: Mass spectra of post-ionized neutral atoms and clusters sputtered from a polycrystalline indium surface under bombardment with 10-keV Ar^+ and SF_m^+ ($m = 1, \ldots, 5$) projectile ions incident under 45^o with respect to surface normal. Post-ionization laser: 193 nm, ≈ 2 x 10^7 Wcm^{-2} [Gh004].

The mass spectrum is recorded at a resolution of about $m/\Delta m = 400$, which appears to be approximately constant across the whole spectrum. Depending on the signal level, the different traces depicted in each panel were recorded with direct charge digitization or single ion pulse counting, respectively (more details about both detection modes are found in Sections. 4. 3. 1, 2). In addition, the signals of sputtered monomers and dimers were blanked from reaching the

detector during acquisition of the pulse counting spectra of larger clusters in order to avoid detector saturation. The two kinds of mass spectra are connected together at the indium tetramers signal because the intensity of this peak was still large enough to be measured directly in the analog mode and, on other hand, was small enough to be detected in the pulse counting mode without saturating the ion counting scheme. Every pulse counting spectrum is averaged over a number of 1000 instrument cycles (primary ion pulses and laser shots). Spectra measured in the analog mode has been averaged over 100 of such pulse counting TOF spectra. As mentioned previously (in Section. 4. 3. 2) the amplification factor (F_{amp}) between analog and pulse counting mode must be determined to compare the resulting yields measured in both modes. In the present experiments, the amplification factor is found to be:

$$F_{amp} = \frac{S_{In_4}^{\text{pulse counting}}}{S_{In_4}^{ana\log}} = 600 \tag{67}$$

It is seen that sputtered neutral clusters containing up to 16 atoms can be identified under bombardment with SF_5^+, SF_4^+ and SF_3^+, whereas Ar^+, SF_2^+ and SF^+ projectiles allow the detection of clusters containing up to 12 atoms. Note that the spectra obtained under SF_5^+ and SF_4^+ are almost identical. While the mass spectrum obtained under Ar^+ bombardment is relatively clean, small peaks corresponding to In_nF and In_nS clusters are observed under SF_m^+ bombardment. The formation of these molecules is caused by a projectile induced S and F contamination of the surface. The magnitude of the corresponding signals is almost negligible for sputtered neutrals but quite strong in the secondary ion spectra. As observed previously under rare ions bombardment [St002], the signal of In monomers is most intensive in comparison with the other cluster peaks. Moreover, the signal intensity of sputtered In_n clusters is found to strongly decrease with increasing cluster size n.

In order to obtain a more quantitative evaluation, Fig. 28 shows the integrated signals of sputtered neutral clusters - normalized to the primary ion current as a function of the cluster size. Since all other experimental parameters are identical (in particular for SF_m^+ projectiles), the resulting signal variation directly represents the variation of the respective partial sputtering yields under bombardment with different projectiles. It is apparent that the yields of neutral indium atoms and dimers sputtered from an indium surface under Ar^+ bombardment are smaller compared to those produced under SF_m^+ cluster ions by factors ranging from 1.8 to 2.7 for atoms and from 1.6 to 2.9 for dimers. Among the SF_m^+ projectile series, a strong enhancement in sputtered cluster abundance is observed with increasing projectile fluorine nuclearity m. The magnitude of this enhancement is found to increase with increasing cluster size n . As will be discussed in more detail below, these findings can in principle

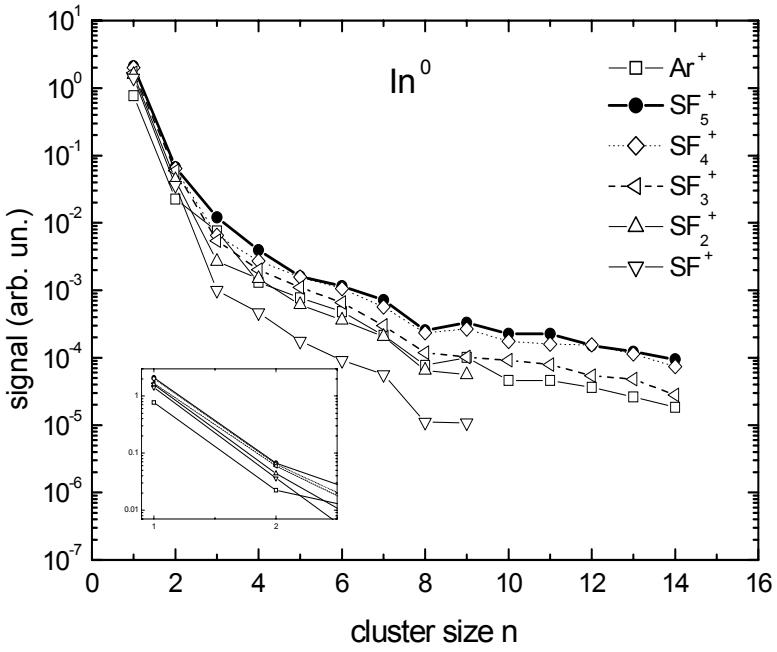

Figure 28: Integrated signal of post-ionized neutral In atoms and In_n clusters sputtered from a polycrystalline indium surface under bombardment with 10-keV Ar^+ and SF_m^+ $(m = 1, ..., 5)$ ions versus cluster size n. The data have been normalized to the primary ion current in order to allow direct comparison between different projectiles [Gh004].

be caused by an independent variation of the total sputter yield or the occurrence of non-additive enhancement effects in collisional spikes. Interestingly, the relative cluster yield distribution produced by Ar^+ bombardment is almost identical to that observed for SF_5^+ , but markedly different from that measured for SF^+. This finding appears surprising since the mass of Ar^+ is significantly smaller than that of SF_5^+, but quite close to that of SF^+.

7.1.4 Secondary cluster ions

As has been discussed already in Section 5. 2, the secondary ion spectra were recorded under the same experimental conditions as the sputtered neutrals, except fact that the post-ionization laser was switched off. Mass spectra of secondary cluster ions ejected from an indium surface under bombardment with 10-keV Ar^+, SF_5^+ SF_4^+, SF_3^+, SF_2^+ and SF^+ ions are displayed in Fig. 29.

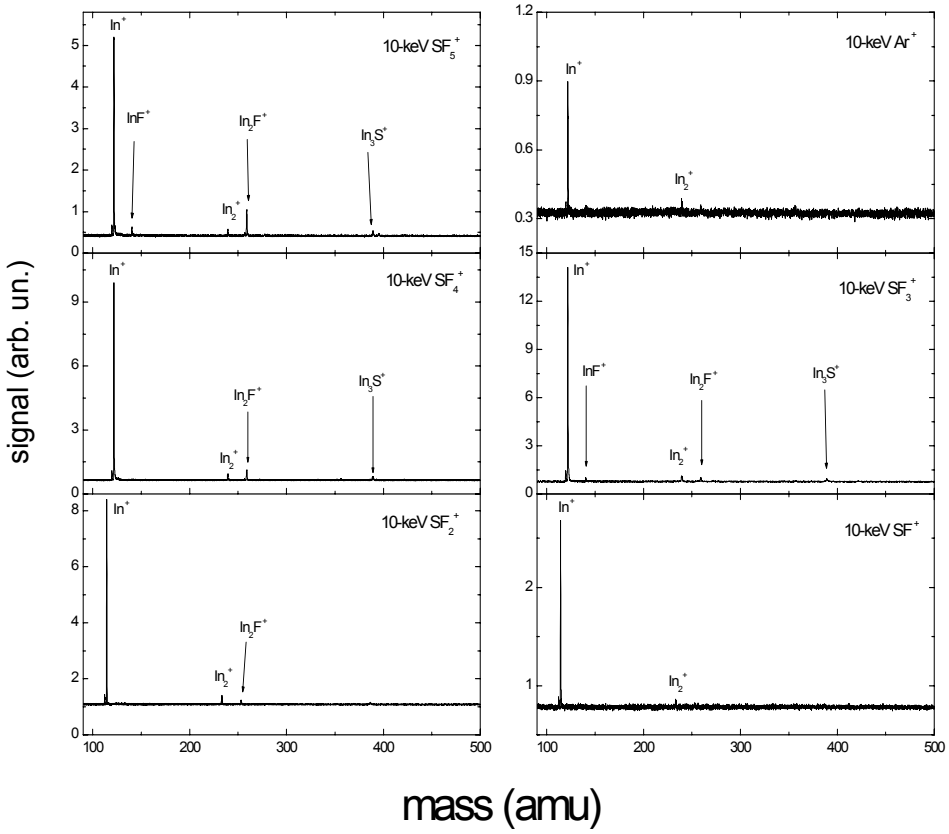

Figure 29: Mass spectra of positive secondary cluster ions sputtered from a polycrystalline indium surface under bombardment with 10-keV Ar^+ and SF_m^+ $(m = 1, \ldots, 5)$ projectile ions incident under 45^o with respect to surface normal.

All spectra were recorded in the analog detection mode for small clusters up to 4 atoms and in the pulse counting mode for larger clusters. Fig. 29 displays only spectra that are recorded in the analog mode for small mass range. As a general observation, it is seen that in all spectra the intensity of

the monomer signal is much higher than that of larger cluster ions. This finding is in good agreement with data measured under 15 keV-Xe^+ bombardment at higher primary ion current density [St002]. The signal intensities of monomers and large cluster ions under SF_m^+ $(m = 1, .., 5)$ projectiles bombardment are higher than those produced by Ar^+, although the Ar^+ primary ion current is larger than those of SF_m^+ (except SF_3^+) projectiles. Comparing the In^+ signals produced by SF_3^+ and Ar^+ find a factor 20, although the primary ion currents of both projectiles are comparable (see Fig. 25). As an important observation, it can be seen that while the signal intensity of InF^+ is much smaller than that of In^+, the larger heteronuclear clusters In_2F^+ and In_3S^+ are higher than the corresponding homonuclear clusters In_2^+ and In_3^+ respectively. This finding indicates the presence of a projectile induced F contamination of the surface. Apparently, the effect of reactive ion bombardment on the enhancement of secondary ions is more pronounced for cluster ions with small abundance.

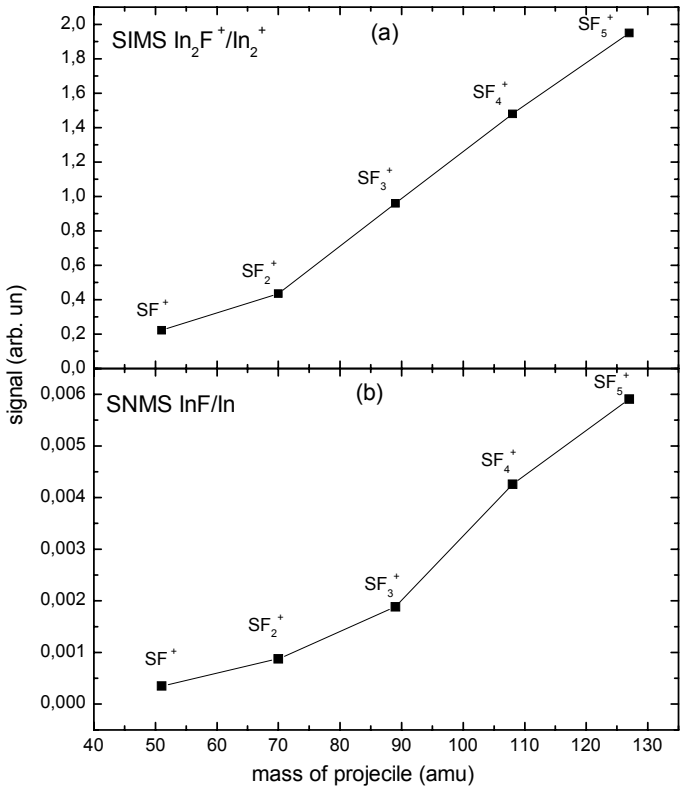

Figure 30: (a) The ratio between the integrated signal of In_2F^+ and In_2^+ and (b) the ratio between the integrated signal of InF and In as a function of projectile mass.

In an attempt to determine the relative concentration of F atoms (c_F^S) on the bombarded surface, we calculated the ratio of integrated signal of In_2F^+ and In_2^+ for different projectiles. The results are displayed in Fig. 30(a). We have selected the SIMS dimer signals to integrate because the In_2F^+ constitutes a prominent peak in all spectra. According to the cluster formation model [Wu87], the sputtered yield is related to the concentration of an elements into the sample surface. By apply this concept in our case we found out:

$$Y_{InF}\alpha c_{In}^S \cdot c_F^S \tag{68}$$

where $c_{In}^S + c_F^S = 1$. In addition;

$$Y_{In_2F}\alpha (c_{In}^S)^2 \cdot c_F^S \tag{69}$$

In case of positive secondary ions

$$Y_{In_2F^+}\alpha (c_{In}^S)^2 \cdot c_F^S \cdot \alpha_{InF}^+ \tag{70}$$

here, α_{InF}^+ is positive ionization probability of InF

$$Y_{In_2^+}\alpha (c_{In}^S)^2 \cdot \alpha_{In_2}^+ \tag{71}$$

A ssuming the variation of α^+ as a function of c_F^S to be similar for both molecules, we obtain. From Eqs. (70, 71)

$$c_F^S \alpha \frac{Y_{In_2F^+}}{Y_{In_2^+}} \tag{72}$$

It is seen that the In_2F^+/In_2^+ ratio is increased directly with increasing fluorine nuclearity in the projectiles, indicating that a higher uptake of fluorine takes place for SF_5^+ projectiles than SF_3^+. These results suggest that the highest secondary indium ion signal measured with SF_3^+ projectiles does not relate to the highest concentration of F atoms on the target surface. This will be discussed in more detail in Section 7. 1. 5. Moreover, to determine the concentration of F atoms from sputtered neutral clusters, we calculate the ratio between the integrated signal of InF and In as a function of projectile mass. The result is displayed in Fig. 30(b). It is seen that the ratio of InF to In also increases directly with increasing fluorine nuclearity of the projectile. From Fig. 30, it is note that the variation of both signal ratios with m is similar. In particular, we find that c_F^S increases about 10-fold between SF^+ and SF_5^+ projectiles. Moreover, it is seen that SF_3^+ bombardment apparently does not produce a larger fluorine surface concentration than SF_5^+. The implication of that finding will be discussed in more detail in Section 7. 1. 5.

The integrated signals of secondary In^+ ions and In_n^+ cluster ions - normalized to the primary ion current - are shown in Fig. 31. As for the sputtered neutral particles, the difference between the curves directly represents the variation of the respective secondary ion yields induced by the different projectiles

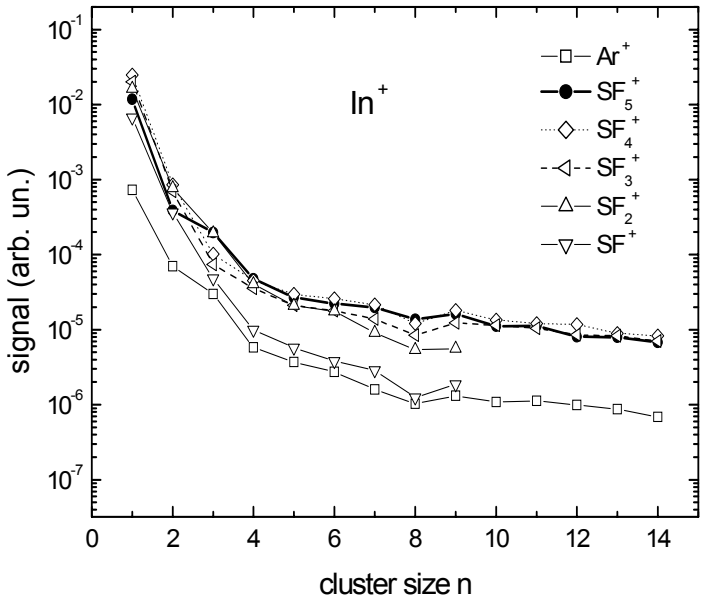

Figure 31: Integrated signal of positive secondary In^+ and In_n^+ cluster ions sputtered from a polycrystalline indium surface under bombardment with 10-keV Ar^+ and SF_m^+ ($m = 1, ..., 5$) ions versus cluster size n. The data have been normalized to the primary ion current in order to allow direct comparison between different projectiles [Gh004].

The first important observation is that in all cases of SF_m^+ projectile bombardment the yields of secondary ions are higher than those produced under Ar^+ bombardment. A second important observation is that - upon transition from Ar^+ to SF_m^+ - the yield increase of secondary ions is much more pronounced than that of the corresponding neutral species. From Fig. 28 and Fig. 31, it is seen that the magnitude of the enhancement is small for sputtered atoms and dimers and increases with increasing sputtered cluster size.

7.1.5 Ionization probabilities

The ionization probability represents one of the most important parameters in secondary ion mass spectrometry (SIMS). It is defined as the probability that a sputtered particle becomes ionized (positive or negative) in the course of the emission process and can be determined experimentally as follows. The measured SNMS signal of secondary neutral particles of a sputtered species X is given by:

$$S(X^0) = I_P \cdot Y_{X^0} \cdot \eta_X^0 \cdot \alpha_X^0 \tag{73}$$

I_P : primary ion current
α_X^0 : postionization probability
$\eta_x{}^0$: geometry and transmission factor

Y_{X^0} : partial sputtering yield of neutral species X that is given by

$$Y_{X^0} = Y_X \cdot \left(1 - \alpha_X^+ - \alpha_X^-\right) \tag{74}$$

where α_X^+, α_X^- denote the positive and negative ionization probabilities, respectively. In the case of metal surfaces the negative ionization probability is found to be very small $\alpha_X^- \ll 1$. Therefore, it will be neglected in the further calculations. The measured positive secondary signal is given by

$$S(X^+) = I_P \cdot Y_X \cdot \alpha_X^+ \cdot \eta_X^{(+)} \tag{75}$$

Due to the fact that neutral and positive sputtered species are measured under exactly experimental conditions, we can assume $\eta_X^0 = \eta_X{}^+$. In addition, $\alpha_X^0 = 1$

for the measured signal of SNMS in saturation mode. Then:

$$\frac{S\left(X^0\right)}{S(X^+)} = \frac{\left(1 - \alpha_X^+\right)}{\alpha_X^+} \tag{76}$$

$$\alpha_X^+ = \frac{S\left(X^+\right)}{S\left(X^+\right) + S\left(X^0\right)} \tag{77}$$

Eq. (77) can now be utilized to evaluate the ionization probabilities of indium atoms and clusters generated by different projectiles. The results are displayed in Fig. 32.

It is seen that the ionization probability produced under Ar^+ bombardment is small compared to that observed under SF_5^+, $SF_4^+$and SF_3^+ impact. Moreover, all ionization probabilities are small compared to unity, and the neutral yields are therefore directly representative of the respective partial sputtering yields. Note that the largest enhancement of the ionization probability is observed for In atoms. For clusters, the enhancement is smaller and almost independent

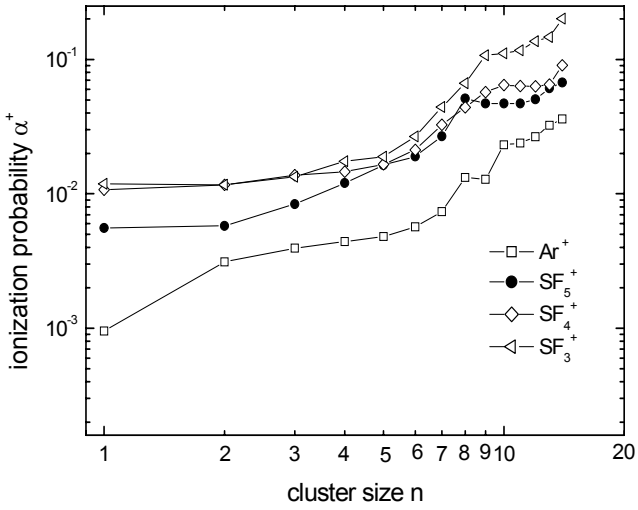

Figure 32: Ionization probability of In atoms and In_n clusters sputtered from a polycrystalline indium surface under bombardment with 10-keV Ar^+ and SF_5^+ $(m = 1, ..., 5)$ ions versus cluster size [Gh004].

of the cluster size. We attribute this enhancement to a chemical matrix effect induced by the incorporation of fluorine from the projectile into the surface. In this context, it is interesting to note that the ionization probabilities exhibit an ordering according to $\alpha_x^+\left(SF_3^+\right) > \alpha_x^+\left(SF_4^+\right) > \alpha_x^+\left(SF_5^+\right)$. At first sight, this result is surprising because one would intuitively expect the highest ionization probability for the projectile containing the largest number of fluorine atoms (SF_5^+). More specifically, one would assume a monotonic dependence on the surface concentration of fluorine, which must under sputter equilibrium conditions be determined by a balance between implantation and re-sputtering of F atoms described by

$$Q^+ = Q^- \tag{78}$$

Here Q^+ is the rate of implantation of F atoms into the target surface that writes as follows :

$$Q^+ = J_p \cdot m \tag{79}$$

Where J_p and m are the primary ion current density and the fluorine nuclearity of the projectile, respectively. Q^- is the rate of resputtering of S and F atoms from the surface that is given by

$$Q^- = Y_{(F)} \cdot J_p \tag{80}$$

$Y_{(F)}$ denote the partial sputtering yields for F atoms, which under sputter equilibrium conditions can be written to first approximation as

$$Y_{(F,S)} = Y_{tot}\left(SF_m^+\right) \cdot c_F^S \tag{81}$$

where Y_{tot} denotes the total sputtering yield. By substituting Eqs. (79, 80, 81) into Eq. (78) we obtain

$$c_F^S = \frac{m}{Y_{tot}\left(\mathrm{SF}_m^+\right)} \tag{82}$$

The last equation describes the equilibrium surface concentration of F atoms as a function of fluorine nuclearity m and total sputtering yield Y_{tot}. The relative variation of Y_{tot} between different projectiles can be determined from the weighted sum of neutral signals $S(n)$ normalized to the primary ion current presented in Fig. 28 according to

$$Y_{tot} \propto \sum_n n \cdot S\left(n\right) \tag{83}$$

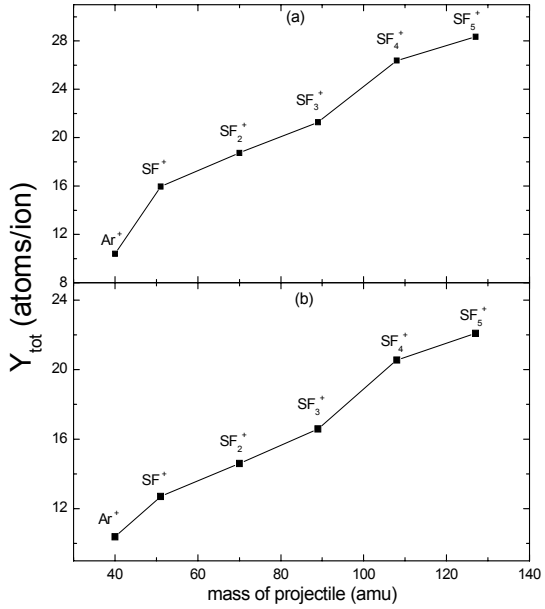

Figure 33: a) Total sputtering yield of polycrystalline indium under bombardment with different 10-keV projectile ions as a function of projectile mass [Gh004]. b) The same data after corrected with respect to the yield produced by Ar^+ ions.

The resulting total sputtering yield as a function of the projectile size is shown in Fig. 33(a). In order to arrive at absolute values, the data have been normalized to a yield value of 10.4 atoms/ion which was calculated for 45°, 10-keV Ar^+ impact using the SRIM 2003 computer simulation package [SRIM]. This was done since no experimental data on indium sputtering yields are available in the range around 10-keV impact energy either for Ar^+or SF_m^+ projectiles.

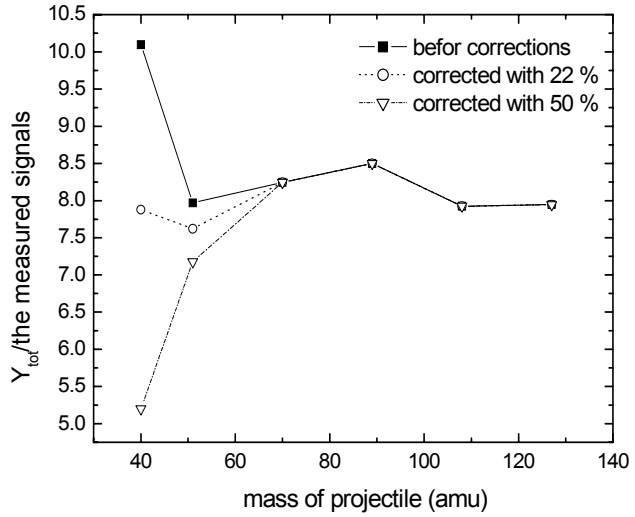

Figure 34: The ratio of the total sputtering yield calcualted by SRIM program and the sum of neutral signals calcuated by Eq. (83).

As mentioned previously (in Section. 5. 1) the measured signals under Ar^+ bombardment may be underestimated by factor of 50 % due to the problem of the timing sequence. That means the total sputtering yields for all constituents of SF_m^+ projectiles should be lower by factor of 2 than the data depicted in Fig. 33(a). To clarify this point, Fig. 34 displays the ratio of the total sputtering yield calculated by SRIM and the sum of neutral signals calculated by Eq. (83). An important observation on the data of Fig. 34 (sold line) is for all SF_m^+ projectiles, the magnitude of the ratio ranging from 8 to 8.5, whereas for Ar^+ the ratio increasing up to 10.25. This means that the measured signals under Ar^+ bombardment is underestimated. However, if we calculated the measured data for Ar^+ with correction factor of 50 % (Fig. 34 dash dot line), the ratio of the total sputtering yield and the measured signals with Ar^+ is clearly lower than the magnitude ratio for all projectiles. This indicates that with correction factor of 50 % the measured signals with Ar^+ is overestimated and in this case the total sputtering yield produced by SF_m^+ projectiles is lower than that estimated by SRIM program. On the basis of these observations, we expect that the the measured signals under Ar^+ bombardment may be underestimated by factor of 22 % rather than 50 %. This assumption is based on the fact that the calculation of signal loss (as described in Section. 5. 1) is inversely depended on the magnitude of r. Therefore, if the magnitude of r is increased the signal loss decreases.

The total sputtering yield and the respective corrected data are displayed in Fig. 33(a) and (b), respectively. It is seen that in both case the total sputtering

yields are larger for SF_m^+ compared to Ar^+ projectiles and increase linearly with increasing projectile fluorine nuclearity. Both findings may be qualitatively interpreted in terms of the fact that our experiments have been performed under identical total kinetic energy of the impinging projectiles. Upon impact, the cluster projectiles disintegrate, and the kinetic energy of each individual constituent atom is lower for larger projectile clusters. According to linear cascade theory [Si81a], the sputtering yield should be roughly proportional to the energy F_D deposited close to the surface. In order to estimate the variation of this quantity for different projectiles, we calculate its depth distribution $F_D(x)$ from the normalized vacancy distribution $f_{vac}(E_0, x)$ calculated for every projectile constituent separately using the SRIM computer simulation code. Assuming a linear superposition of effects induced by each projectile constituent, the resulting value of F_D at the surface ($x = 0$) imposed by the impact of an SF_m^+ projectile is determined as

$$F_D(x=0) = m \cdot f_{vac}^F\left(E_0^F, x=0\right) \cdot E_0^F + f_{vac}^S\left(E_0^S, x=0\right) \cdot E_0^S \qquad (84)$$

where E_0^F and E_0^S reflect the kinetic energy partition between F and S projectile constituents, respectively. The magnitude of E_0^F and E_0^S will be estimated from the kinetic energy partition according to:

$$E_0 = (M_S + mM_F)\frac{1}{2} \cdot V^2 \qquad (85)$$

Where E_0 the total kinetic impact energy (10-keV), M_S and M_F the atomic mass of S and F atoms respectively, V is the impact velocity . The kinetic energy of S and F atoms is given by

$$E_0^S = M_S \cdot \frac{1}{2}V^2 \qquad (86)$$

$$E_0^F = M_F \cdot \frac{1}{2}V^2 \qquad (87)$$

from Eqs. (85, 86 , 87) we obtain

$$E_0^S = \frac{M_S}{M_S + mM_F} \cdot E_0 \qquad (88)$$

$$E_0^F = \frac{M_F}{M_S + mM_F} \cdot E_0 \qquad (89)$$

The resulting energies of S and F atoms for different projectiles calculated by equations (88, 89) are displayed in the following table:

Projectiles	E_0^S keV	E_0^F keV
SF_5^+	2.5	1.5
SF_4^+	3	1.75
SF_3^+	3.6	2.13
SF_2^+	4.5	2.7
SF^+	6.27	3.72

In evaluating Eq. (84), the calculated distributions $f_{vac}(x)$ were averaged over a surface layer of $\Delta x = 2$ Å. The resulting values of F_D calculated for 10-keV Ar^+ and SF_m^+ projectiles impinging under 45° are depicted in Fig. 35.

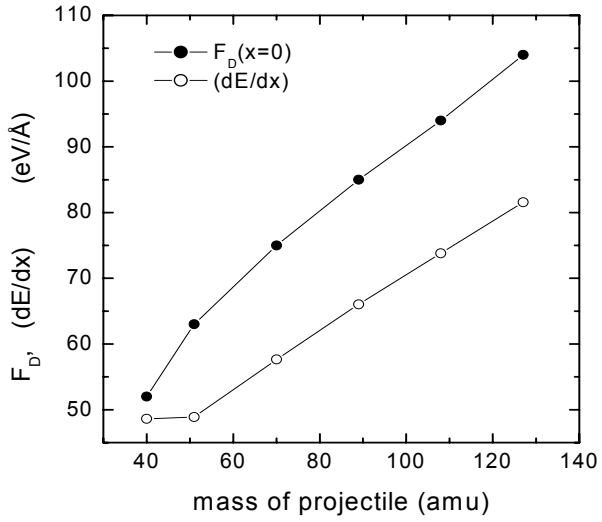

Figure 35: Energy F_D deposited at the surface and effective projectile stopping power (dE/dx) for impact of different 10-keV projectiles onto indium as a function of projectile mass. The data have been calculated using the SRIM2003 computer simulation package [Gh004].

It is evident that at constant impact energy all SF_m^+ clusters deposit more energy at the surface than the Ar^+ projectile. Moreover, a larger projectile deposits more of its energy closer to the surface, thereby producing a higher sputtering yield. Both predictions are in good agreement with our experimental observations depicted in Fig. 33. According to linear cascade theory, the deposited energy should be proportional to the projectile stopping power $(dE/dx)\,|_{E_0}$. Since both quantities are determined in the SRIM simulation code, we can compare their projectile dependence as shown in Fig. 35. In order to calculate the effective stopping power, the same summation procedure as outlined in Eq. (84) is employed. It is seen that for SF_m^+ projectiles the linear dependence on fluorine nuclearity m is observed in both cases. Interestingly, the proportionality constant

$$\alpha = \frac{F_D\,(x=0)}{(dE/dx)\,|_{E_0}} \tag{90}$$

appears to be smaller for Ar^+ (1.0) than for SF_m^+projectiles (1.3). According to theory, this quantity should increase with increasing mass ratio between target and projectile (Fig. 36).

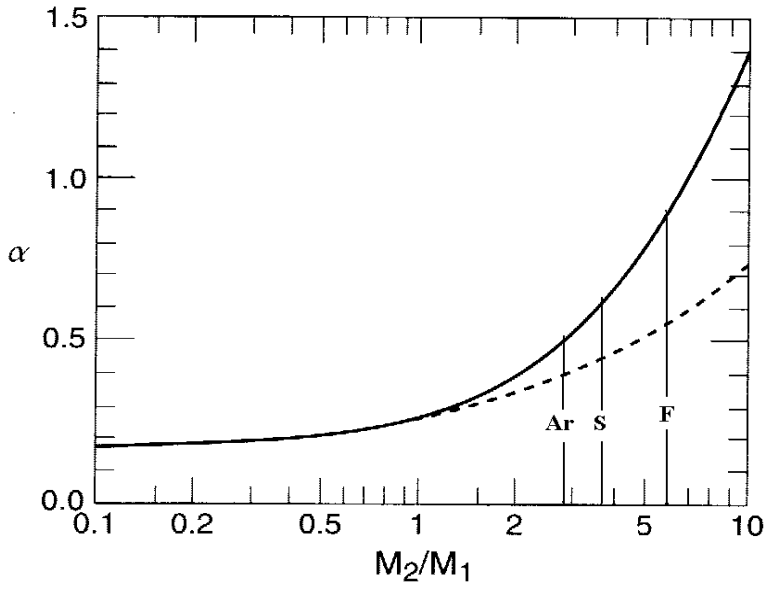

Figure 36: Factor α dependence on mass ratio M_2/M_1. Full-drawn line: theoretical, evaluated for elastic scattering only no surface correction applied. Dashed curve, interpolated from experimental sputtering yields for 45 keV Ar^+ ions on Si, Cu, Ag and Au. The difference is mainly due to the neglect of the surface correction at large mass ratios [Si81a]

The fact that we observe a higher α for SF_m^+ therefore provides a good indication that the stopping of an SF_m^+ projectile is equivalent to the sum of the stopping of its constituents. A similar finding has been reported for Au_n^- projectiles implanted into various metal and semiconductor target materials [An003].

The sputtering yield data depicted in Fig. 33a) can now be used to estimate the fluorine uptake of the surface as a function of projectile fluorine nuclearity m. After evaluating Eq. (81) for different values of m, it is found that the maximum fluorine uptake should occur for SF_5^+ (Fig. 37). In contrast, the maximum ionization probability is measured for SF_3^+ . As a consequence, we have to conclude that either the ionization probability does not strictly monotonously depend on the surface concentration of fluorine, or that other factors must also play a role in the formation of secondary ions at SF_m^+-bombarded surfaces.

In fact, a similar observation as made here has been previously reported by Reuter and coworkers [Re87], [Re88b] who demonstrated that an increase of the surface fluorine uptake by bleeding F_2 into the vacuum chamber does not necessarily enhance the secondary ion yields. Moreover, they found that the ionization probabilities of atoms sputtered from metallic targets under CF_3^+ bombardment were higher than or at least equal to those found for O_2^+ projectiles. When comparing our results with those obtained in refs. [Re87], [Re88b], it is of interest to note that

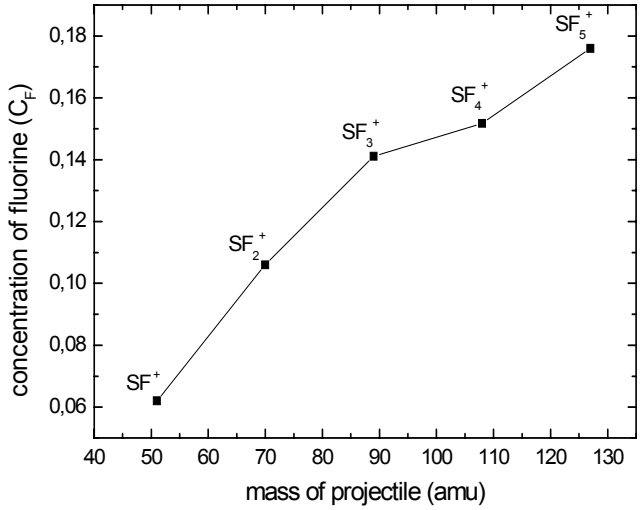

Figure 37: Concentration of fluorine onto the target surface calculated by Eq. (82) as a function of projectile mass.

(i) the primary ion current delivered from the ion source was largest at CF_3^+([Re87], [Re88b]) and SF_3^+ (our case)

(ii) the highest ionization probabilities have been observed for CF_3^+ ([Re87], [Re88b]) and SF_3^+ (our case).

We deduce from these results that the projectile XF_3^+ (X= C, S,...) must have some specialty that makes it the most abundant ion in the plasma on one hand and the most effective projectile for the production of secondary ions on the other hand.

7.1.6 Partial sputtering yields

In order to discuss the efficiency of different projectiles with respect to cluster production in sputtering, we first define relative partial sputtering yields of In_n clusters as

$$Y_{In_n}^{rel} = \frac{Y_{In_n}}{Y_{In_1}} \tag{91}$$

The yield enhancement of a sputtered cluster containing n atoms as a function of the projectile fluorine nuclearity m is then described by an enhancement factor

$$k_{1,m}(n) = \frac{Y_{In_n}^{rel}(SF_m^+)}{Y_{In_n}^{rel}(SF^+)} \tag{92}$$

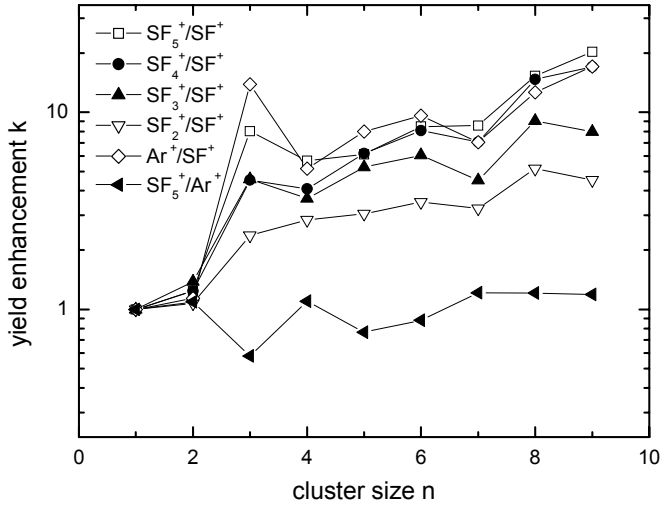

Figure 38: Enhancement factor k [see Eq. (92) for definition] for partial sputter yields of In_n clusters upon transition from SF^+ to SF_m^+ and Ar^+ projectiles as a function of cluster size n [Gh004].

The resulting values are plotted as a function of the cluster size n in Fig. 38

For the set of SF_m^+ projectiles, it is seen that the enhancement observed with increasing m is more pronounced for larger sputtered clusters. The largest effect is observed for In_9, the production of which is enhanced about 20 times as much as the total sputtering yield upon transition from SF^+ to SF_5^+ projectiles.

It should be noted that the increase observed for all sputtered clusters larger than dimers is non-additive in the sense that the value of $k_{1,m}$ is larger than the atom ratio $(m+1)/2$ between SF_m^+ and SF^+ projectiles. Since our work was performed under conditions of constant total impact energy rather than constant impact velocity, the values of k determined here cannot be directly compared to what has frequently been described as non-additive cluster yield enhancement measured for constant impact energy per constituent projectile atom [Be97], [Be00a], [Be00b]. In any case, the data presented in Fig. 38 provide clear evidence that the efficiency of cluster production is significantly increased during the progression from SF^+ to SF_5^+ projectiles.

In principle, this finding is expected since it has been frequently observed that the relative abundance of sputtered clusters is correlated with the total sputtering yield [Wu002]. More specifically, the cluster abundance distribution is changed in favor of large clusters with increasing total yield as long as atomic projectiles are used. For polyatomic projectiles, it has been demonstrated that this correlation may not be valid any more if the total yield significantly exceeds about 30 atoms/ion, indicating a transition into the "spike" regime of sputtering [He003]. Since all sputter yield values determined here are below that limit, our

data fit well into this picture.

Interestingly, the enhancement factors measured for Ar^+ with respect to SF^+ projectiles are practically identical to those determined for SF_5^+. Hence, SF_5^+ is not more efficient in producing sputtered clusters than Ar^+, but more efficient than SF_m^+ with smaller m. Particularly the former finding appears surprising, since the monoatomic Ar^+ projectile will penetrate deeper into the solid, leading to less deposition of energy immediately at the surface. As a consequence, the total sputtering yield imposed by Ar^+ impact is smaller than those induced by SF_m^+ projectiles (cf. Fig. 33). The well-known scaling of the cluster yield distribution with total sputter yield [Wu002] would therefore predict a pronounced enhancement between Ar^+ and SF_5^+. The fact that this is not observed may relate to the incorporation of projectile species into the surface. To clarify this point some more, we employ simple statistical considerations, which state that the yield of a sputtered In_n cluster should follow the indium surface concentration as $\left(c_{In}^S\right)^n$. Therefore, if c_{In}^S is reduced due to an S or F surface contamination, cluster formation will be suppressed, the effect being the more pronounced the larger the sputtered cluster. For an In_9 clusters, a contamination induced reduction of c_{In}^S by 20 % ($c_{In}^S = 0.8$) would already lead to an order of magnitude decrease in relative cluster yield. The resulting yield reduction may in principle counterbalance the enhancement induced by the larger total sputtering yield.

7.1.7 Conclusion

The use of SF_m^+ ($m = 1, \ldots, 5$) cluster ion projectiles to bombard an indium surface leads to a drastic increase of the ionization probability of sputtered In atoms and In_n clusters as compared to Ar^+ ion bombardment at the same kinetic energy. This effect is attributed to a chemical matrix effect due to fluorine incorporation into the target surface. The largest value of the ionization probability is found for a projectile fluorine nuclearity of $m = 3$. This finding suggests that the formation of secondary ions cannot solely be determined by the fluorine surface concentration.

The total sputtering yield is found to be larger for SF_m^+ than for Ar^+ projectiles and to increase linearly with increasing m. Both findings are shown to be in agreement with the prediction of linear cascade theory. For SF_m^+ projectiles, the relative abundance of clusters in the total flux of sputtered particles is found to increase with increasing m, the enhancement being larger for larger sputtered clusters. This finding is in accordance with the general correlation between cluster abundance distribution and total sputtering yield which has been found for many target materials under bombardment with monoatomic projectiles. From these observations, we conclude that non-linear effects do not play a dominant role for the system and impact energy studied here. No

significant increase of relative cluster abundances, on the other hand, is found between Ar^+ and SF_m^+ projectiles, although the total sputtering yield induced by SF_5^+ projectiles is almost 3-fold larger than that induced by Ar^+. We suggest that this finding may be caused by the surface contamination under SF_m^+ bombardment which acts to suppress the formation of larger clusters.

7.2 Formation of sputtered silver clusters under bombardment with Xe^+ and SF_5^+ ions

As already outlined in the introduction, silver represents an interesting target metal for investigations performed here, since a large database on cluster sputtering under atomic projectile bombardment exists for that material. In particular, it has been established experimentally that rare gas ion bombardment of polycrystalline silver surfaces produces the highest relative cluster abundance in the sputtered flux that has been observed for metallic targets under comparable bombardment conditions. If heavy projectiles such as Xe^+ are employed with kinetic impact energy above 10 keV, our group has demonstrated that more than 50 % of all emitted Ag atoms leave the surface in a bound state, i.e., in form of Ag_n clusters [St2000]. The size distribution of the emitted clusters has been found to be dominated by dimers ($n = 2$) with a relative abundance of several 10 % (normalized to that of monomers). All relative yields of larger clusters with $n \geq 3$ are found to be at least one order of magnitude smaller and decay towards larger sizes according to a power law $n^{-\delta}$, the exponent δ ranging from about 7.5 to 3.7 depending on the bombarding conditions. The smallest value of δ, corresponding to the highest relative abundance of large clusters in the sputtered flux has been observed for 15-keV Xe^+ impact [St2000]. In this work; Staudt et al. have found a variation of the power law exponent δ depending on the sputtered cluster size : for $n \leq 30$, a value of $\delta = 4$ was measured, while for $n > 30$ the decay become much less pronounced, now corresponding to a value of of $\delta \simeq 2$.

Based on that experience, it is of great interest to determine whether bombardment with a polyatomic projectile may even further enhance the relative clusters abundance. In this context, SF_m^+ ions represent a particularly useful class of projectiles, since SF_5^+ has virtually the same mass as Xe^+. In a first step, we will therefore compare the Ag_n cluster abundance distributions generated by isoenergetic SF_5^+ and Xe^+ and relate them to the difference in total sputter yield. The results of that study, which was performed in collaboration with the Arifov institute of Electronics of the Uzbekistan Academy of Science and historically constitutes our first experiments on sputtered metal cluster yields under SF_m^+ bombardment, will be described in this chapter.

7.2.1 Experimental conditions

In the present experiment a polycrystalline metallic silver sample is bombarded under 45° incidence with Xe^+ or SF_5^+ ions at 10 keV impact energy. The cold cathode plasma ion source was operated with either pure Xe or SF_6 gas and under optimized conditions delivers a total beam 330 nA (Xe^+) and 77 nA (SF_5^+), respectively. Mass spectra of neutral particles sputtered from the surface are recorded by post-ionization of ejected neutral species using an intense UV laser pulse. The ionizing laser was again operated at $\lambda = 193$ nm. Note that in this experiment due to the high ionization potentials of Ag and Ag_2 (≈ 7.6 eV) the photoionization efficiency is not saturated and the measured signals of post-ionized neutral Ag atoms and Ag_2 dimers therefore strongly depend on the laser power density. The pulse energy of the laser was therefore carefully monitored and kept constant within a few percent by means of an optical feedback loop.

It should be noted at this point that the use of 193 nm postionization constitutes a major drawback of the experiments on silver and was the original reason why we chose indium as a target material in the preceding chapter. For silver, we could in principle change the ionizing laser to a wavelength of 157 nm, where the corresponding photon energy (7.9 eV) would be sufficient to allow single photon ionization of all sputtered Ag_n species. While this was done in previous studies performed in our group [Wa94], [St2000] it was not possible here due to the fact that the Atomika ion source needed to generate the SF_m^+ ions and VUV laser generating the 157 nm radiation are physically attached to two different TOF system. Since transport of VUV radiation over long distances is problematic, we therefore chose to revert to the more readily available UV wavelength of 193 nm, thereby sacrificing the possibility of single photon ionization for sputtered Ag and Ag_2 species. The results obtained this way can still be quantified due to the fact that the measured spectra under rare gas ion bombardment can be compared to those obtained earlier using a different ion source and 157 nm postionization.

7.2.2 Neutral clusters

Fig. 39 shows raw data, i.e., mass spectra of post-ionized sputtered neutral atoms and clusters which have been ejected from a polycrystalline silver surface under bombardment with 10-keV Xe^+ and SF_5^+ ions under otherwise identical experimental conditions. The mass spectra were recorded at a resolution of about $m/\Delta m = 350$, which appears to be approximately constant across the whole spectrum.

Depending on the signal level, the different traces depicted in each panel were recorded with direct charge digitization or single ion pulse counting, respectively. The conversion factor F_{amp} between both spectra was determined

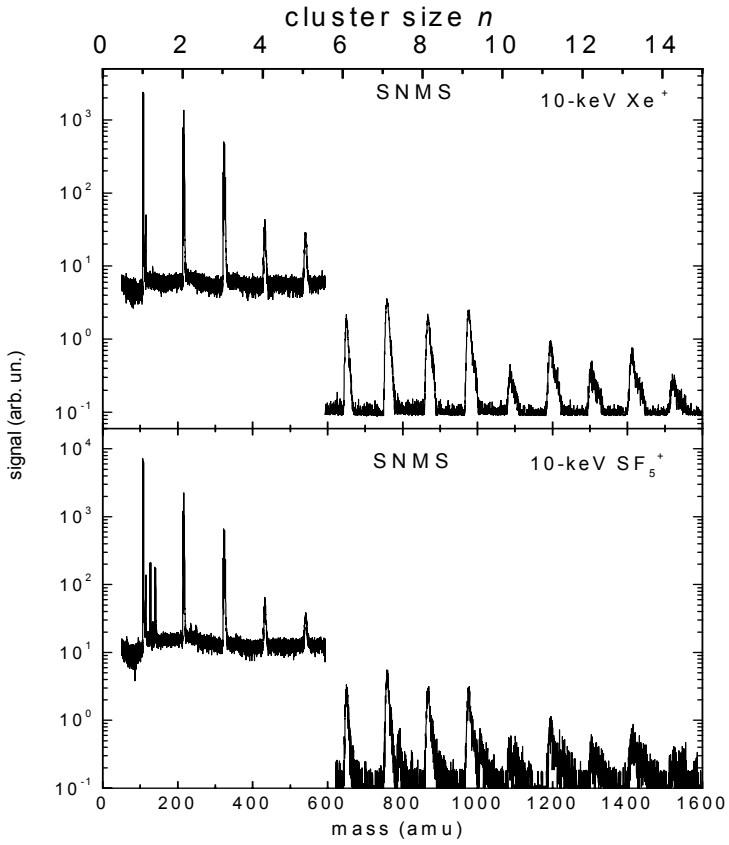

Figure 39: Mass spectra of post-ionized neutral atoms and clusters sputtered from a polycrystalline silver surface under bombardment with 10-keV Xe^+ and SF_5^+ ions incident under 45° with respect to surface normal. Post-ionization laser: 193 nm, $\approx 10^7$ Wcm^{-2}. The data have been normalized to the primary ion current in order to allow direct comparison between the two projectiles.

from the overlapping signals of Ag_5 and Ag_6 leading to an average value of $F_{amp} = 550 \pm 50$. In addition, the signals of monomers and dimers were blanked from reaching the detector during acquisition of the pulse counting spectra in order to avoid detector saturation. It is seen that in both cases sputtered neutral clusters containing up to more than 14 atoms can be observed. While the spectrum obtained under Xe^+ bombardment is relatively clean, small peaks corresponding to Ag_nF and Ag_nS clusters are observed under SF_5^+ bombardment which are caused by a projectile induced contamination surface. As already observed for the indium sample, the magnitude of these signals is negligible for sputtered neutrals but quite strong in the secondary ion spectrum.

Both spectra depicted in Fig. (39) have been normalized to the primary ion current in order to allow direct comparison between the two projectiles. Due to the fact that the total signal heights observed in both spectra are compa-

rable, it is evident that the respective partial sputtering yields do not change significantly between Xe^+ and SF_5^+ projectiles.

For a more quantitative evaluation, Fig. 40 shows the integrated signals, again normalized to the primary ion current, as a function of the number of atoms in the sputtered cluster.

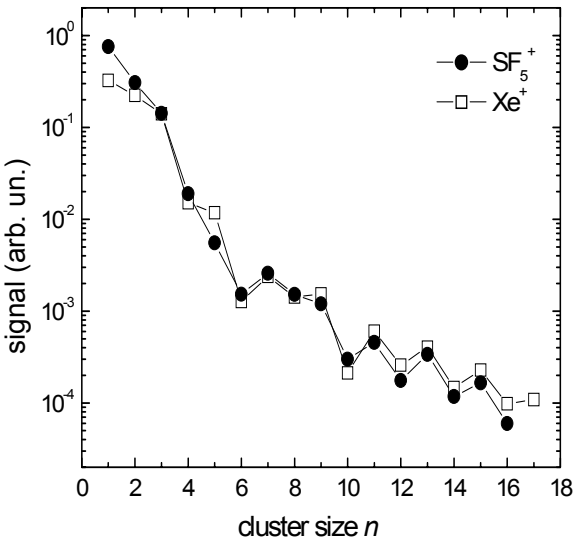

Figure 40: Integrated signal of post-ionized neutral Ag atoms and Ag_n clusters sputtered from a polycrystalline silver surface under bombardment with 10-keV Xe^+ and SF_5^+ ions versus cluster size n. The data have been normalized to the primary ion current in order to allow direct comparison between the projectiles [Gh002].

It is apparent that the partial sputtering yields of silver atoms and dimers sputtered from a polycrystalline silver surface are enhanced by factors of 1.5 and 1.2, respectively, while the yields of larger clusters remain practically unchanged upon switching from Xe^+ to SF_5^+. This observation clearly indicates that the total sputtering yield under SF_5^+ bombardment is comparable to that induced by Xe^+ bombardment. It also coincides with what would be expected from a linear addition of the yields arising from the constituent atoms of the SF_5 projectile impinging with the same velocity (using literature data [An81] measured for Ne and Ar instead of F and S projectiles, respectively), thus indicating that any non-linear enhancement of the total sputtering yield under SF_5^+ bombardment is small.

7.2.3 Secondary cluster ions

The mass spectra of positive secondary atomic and cluster ions sputtered from a polycrystalline silver surface under bombardment with 10-keV Xe^+ and SF_5^+ ions are displayed in Fig. 41.

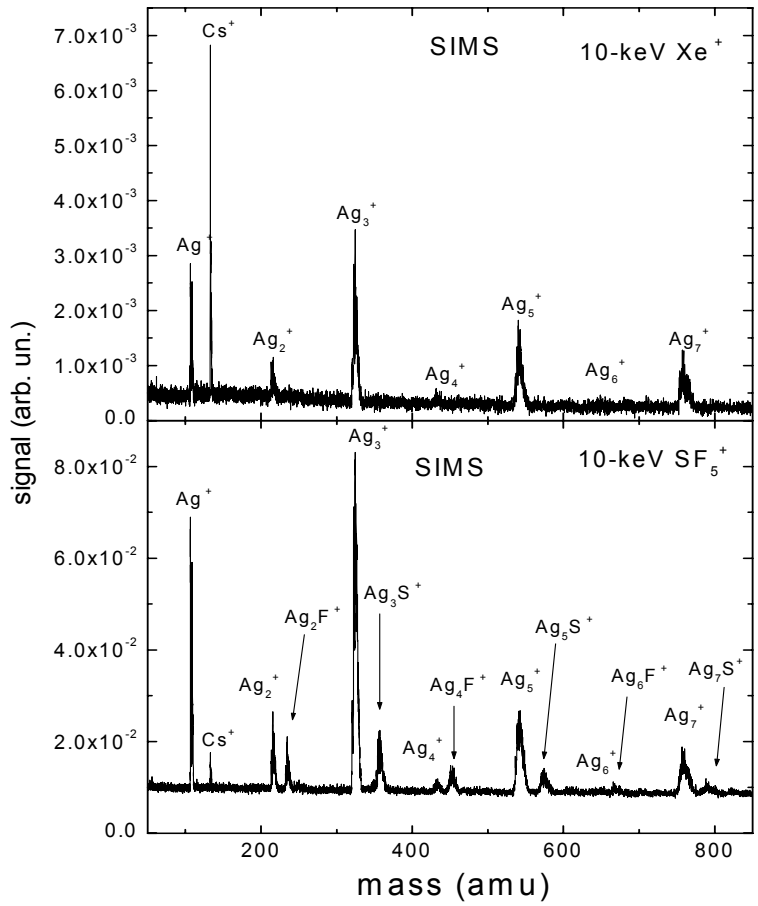

Figure 41: Mass spectra of positive secondary atomic and cluster ions sputtered from a polycrystalline silver surface under bombardment with 10-keV Xe^+ and SF_5^+ ions incident under 45° with respect to surface normal. The data have been normalized to the primary ion current in order to allow direct comparison between the two projectiles.

The mass resolution visible in the SIMS spectra is similar to that observed in SNMS spectra ($m/\Delta m = 350$). The spectra are recorded in the analog mode for small clusters and in the pulse counting mode for larger clusters. We display here only the mass spectra recorded in the analog mode in order to obtain a

good picture and to clear the small peaks of Ag_nF^+, Ag_nS^+. It is seen that Ag_n^+ cluster ions up to $n = 7$ are clearly observed for both projectiles.

From both mass spectra (Fig. 41) two characteristics can be recognized. There are:

(i) a sharp decrease in the ion intensity at special cluster numbers, for instance Ag_4^+ and Ag_6^+

(ii) oscillation in the ion intensity at odd-even cluster nuclearity, i.e., the ion intensity of odd-numbered clusters is larger than that of the adjacent even-numbered clusters. This behavior has been previously observed for sputtered coinage metal (Cu, Ag and Au) cluster ions under rare ions bombardment. Such behavior can be explained on the basis of an electronic shell model [Ka86], [Ka85]. According to this model, the stability of the cluster is mainly determined by the spin pairing of valence electrons in the cluster. Therefore, clusters containing an even-number of valence electrons (odd n) are more stable compared to those having an odd-number of electrons (even n). The results are of interest since the calculated ionization potential of silver clusters exhibits a similar alternation [Ba71], [Ja92]. In these comparisons, it is important to note that in the size range covered by Fig. 41 the intensity of neutral clusters (Figs. 39, 40) drops monotonously with increasing cluster size and is therefore not the contributing factor in producing the observed alternation of the ion intensity (Figs. 41, 42).

From Fig. 41 some important observations could be recorded :

i) The intensities of Ag^+ atom and Ag_n^+ cluster ions by Xe^+ bombardment are quite low compared with those by SF_5^+ bombardment, although the primary ion current of Xe^+ is higher 4 times than that of SF_5^+.

ii) In the mass spectrum recorded with SF_5^+ projectiles, cluster ions of Ag_nF^+ and Ag_nS^+ were formed due to the contamination of the target surface by fluorine or sulfur of projectile ions. In this respect, it is important to note that, for very small cluster ions abundance (Ag_4^+ and Ag_6^+)the signals are smaller than those of the corresponding of heteronuclear cluster ions (Ag_4F^+ and Ag_6F^+). This finding indicates that the effect of reactive ion bombardment on the enhancement of the secondary cluster ions is being large for clusters with small abundance.

iii) In both spectra, a Cs contamination is observed. The origin of this contamination must be due to some cesium contaminated the system from previous work, since otherwise there is no cesium present in the target. It is seen that in the mass spectrum recorded under Xe^+ bombardment the cesium signal is higher than that of Ag^+ atom, while this signal is

lower than that of Ag^+ atom with SF_5^+ bombardment. In order to clarify this point, we have calculated the cesium yield in two spectra by integrating the signals and normalized the integrated values to the primary ion current. The resulting values are found to be comparable in both cases,indicating that the yield of cesium ions is not influenced by SF_5^+ bombardment and confirm that the observed signal of cesium is just a SIMS effect. Also, Cs is known to be sputtered with a very large ionization probability [Me001]. Therefore, a large Cs^+ signal in a SIMS spectrum does not necessarily indicate a sizeable surface contamination.

Fig. 42(a) shows the integrated secondary ion signals of Ag^+ ions and Ag_n^+ cluster ions - normalized to the primary ion current - as a function of cluster size. Due to the normalization the difference between the curves directly represents the variation in secondary ion yields induced by the different projectiles.

The first important observation is that the secondary ions exhibit a much more pronounced yield increase than the corresponding neutral species. In order to determine exactly the relative variation of secondary ion yields between Xe^+ and SF_5^+ projectiles, the integrated signals $S(n)$ normalized to the primary ion current presented in Fig. 42(a) are summed according to

$$Y_{ions} \propto \sum_n n \cdot S(n) \tag{93}$$

where n is the number atoms in the cluster ion. After evaluating Eq. (93) for each projectile, it is found that the total ion yield for SF_5^+ projectiles is 16 times higher than that of Xe^+.

A second important observation concerns the relative intensities of clusters with respect to that of the monomer. From Fig. 40 and Fig. 42, it is seen that the relative yields of clusters are practically identical for SF_5^+ and Xe^+ projectiles. For the case studied here, the relative abundance of sputtered clusters is evidently not enhanced when polyatomic projectiles are used instead of atomic ions. Many experiments on cluster formation in sputtering have indicated that the abundance pattern of sputtered clusters is correlated with the total sputtering yield in such a way that higher sputtering yields lead to an increased abundance of large clusters [Wu97]. Since the total sputtering yield is not significantly changed, one would therefore expect comparable abundance distributions under Xe^+ and SF_5^+ bombardment. At least for the bombarding conditions employed here, a non linear (or non additive) enhancement of the formation of large clusters under bombardment with a polyatomic projectile - as has frequently been reported in the literature [Be97], [Be00a] - is clearly not observed.

The same work related to investigate the influence of polyatomic projectiles SF_5^+ on the secondary ion yields in comparison with monatomic projectile

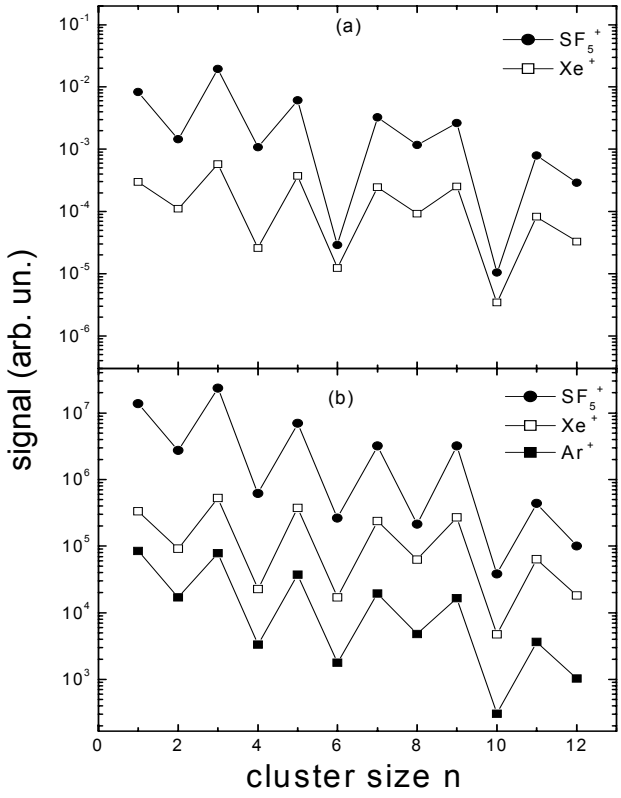

Figure 42: (a) Integrated signal of positive secondary Ag^+ and Ag_n^+ cluster ions sputtered from a polycrystalline silver surface under bombardment with 10-keV Xe^+ and SF_5^+ ions versus cluster size n. (b) The same data under bombardment with 11-keV Ar^+, Xe^+ and SF_5^+ ions [Gh002]. In (a) and (b) the data have been normalized to the primary ion current in order to allow direct comparison between different projectiles. The data in (b) have been measured in Arifov Institute at Tashkent (Uzbekistan).

such as Ar^+ and Xe^+ have been carried out in Arifov Institute at Tashkent (Uzbekistan) [Gh002]. In this work a double focusing arrangement consisting of a magnetic sector and an electrostatic prism was used to detect ionic clusters, which are sputtered from a polycrystalline silver sample under bombardment with Ar^+, Xe^+ and SF_5^+ ions impinging under 45° with respect to the surface normal. The primary ions are generated by an electron impact ion source with axial symmetric magnetic field delivering total beam currents of about 0.6 μA for Ar^+, Xe^+ and SF_5^+ ions. In order to permit a rapid switching between different projectile ions, the ion source was operated with a gas mixture of Argon, Xenon and SF_6, and the desired projectile was selected by means of a Wien filter. The energy of the primary ions was kept constant at 11 keV. The setup

is mounted in an ultrahigh vacuum (UHV) chamber with a base pressure of about 10^{-9} mbar. During the experiments, the working pressure rises to about $2 \cdot 10^{-7}$ mbar due to the operation of the gas ion source.

The results of this work are displayed in Fig. 42(b) that shows the integrated signals of Ag^+ ions and Ag_n^+ cluster ions sputtered under11-keV Ar^+, Xe^+ and SF_5^+ bombardment, normalized to the primary ion current. At first sight, it is seen that the same qualitative observations are made with both experimental setups. In view of the largely different mass spectrometric techniques employed in both setups, this finding is re-assuring. In order to calculate the variation of ion yields between different projectiles, the same summation procedure as outlined in Eq. (93) is employed. It is found that the ion yields produced by SF_5^+ are 200, 19 times higher than that of Ar^+ and Xe^+ respectively. These findings are again in good agreement with our results.

From the comparison of secondary ions with the corresponding neutral data, it is immediately evident that the strong yield enhancement observed for secondary ions cannot be due to increased partial sputtering yields, but must be caused by a more efficient ionization of the sputtered atoms and clusters under SF_5^+ bombardment. Under Xe^+ bombardment, the secondary ion signals are significantly below those of post-ionized neutrals, thus indicating a relatively low ionization probability which is typical for rare gas projectiles impinging onto a relatively clean metallic sample. It should be noted again that although the neutral and ion spectra depicted in figures (41, 39) have been recorded under otherwise identical experimental conditions, the relative signal height does not necessarily reflect the ionization probability, since the post-ionization process leading to the detection of the neutral species is not always here saturated. This is particularly true for atoms and dimers which are ionized by a two-photon absorption process. Nevertheless, it is evident that the ionization probability is strongly enhanced under SF_5^+ bombardment. In view of the large chemical matrix effects generally observed in SIMS, this finding is not surprising.

It is known that the presence of electronegative species at the surface often significantly enhances the formation probability of positive secondary ions, an effect that is frequently called the "chemical enhancement effect" in SIMS[Yu93]. Since the bombardment with SF_5^+ projectile ions will inevitably lead to a fluorine contamination at the surface, an enhancement of the ionization probability is therefore likely to be expected. The ionization probability of silver atoms and clusters sputtered under rare gas projectile bombardment has been determined to vary from around 10^{-4} for monomers to several 10^{-2} for large clusters ($n > 5$) [He2000]. The data displayed in Fig.(40), which are in qualitative agreement with this finding, now indicate that a sizeable fraction of the clusters sputtered under SF_5^+ bombardment leaves the surface as positive secondary ions.

7.2.4 Conclusion

The experiments reveal that the bombardment of a clean silver surface with SF_5^+ projectile ions leads to a drastic increase of the ionization probability of sputtered Ag atoms and Ag_n clusters as compared to rare gas ion bombardment at the same kinetic energy. The partial sputtering yields, on the other hand, which may be taken as representative of the collisional formation mechanisms of sputtered clusters, remain practically unchanged. More specifically, the mass distribution of sputtered particles does not change in favor of large clusters between SF_5^+ and Xe^+ projectiles. One must therefore conclude that - at least in the impact energy region explored here - non linear enhancement effects due to the polyatomic nature of the SF_5^+ projectile do not occur. In particular, a drastically increased abundance of large clusters that has been observed in other experiments using polyatomic projectiles seems to be absent for the impact of SF_5^+ onto silver.

7.3 Cluster sputtering from silver under bombardment with SF_m^+ $(m = 1, .., 5)$ projectiles

Expanding on the comparison between Xe^+ and SF_5^+ projectiles presented in the preceding section, this chapter is devoted to a more systematic investigation of the role of projectile fluorine nuclearity in sputtering of silver. Also in these experiments, the Atomika ion source was operated with pure SF_6 gas.

7.3.1 Experimental conditions

Fig. 43 shows the residual gas spectrum recorded in the main UHV chamber by a quadrupole mass spectrometer under these operating conditions. As already seen for the gas Ar/SF_6 mixture (Fig. 24), the intensity of the SF_5^+ is much higher than other fragments SF_6 and the intensity of SF_3^+ is higher than that of SF_4^+.

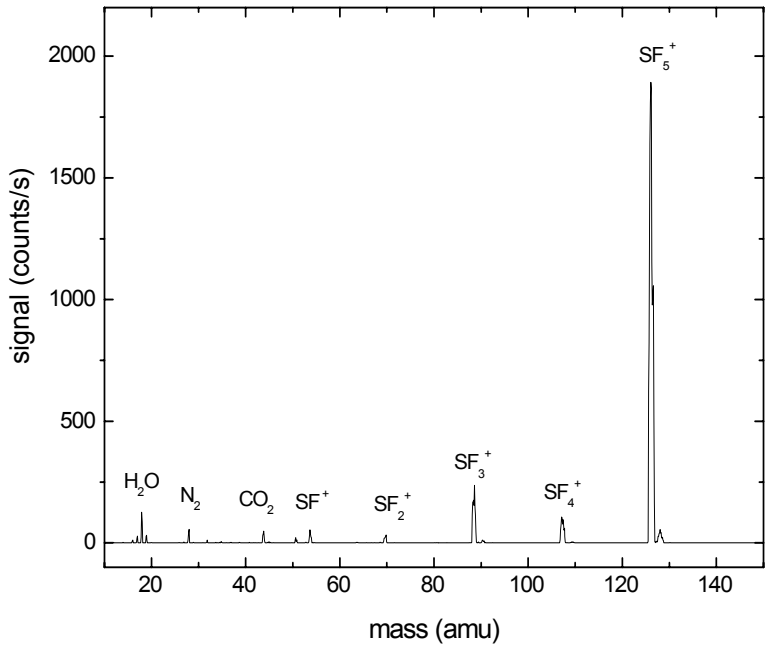

Figure 43: Mass spectrum of pure SF_6 gas recorded by a quadrupole spectrometer : vacuum pressure $5{\cdot}10^{-8}$ mbar.

The integrated abundance of each fragments ion are displayed in the following table

SF_6 fragment ion	SF_5^+	SF_4^+	SF_3^+	SF_2^+	SF^+
relative abundance	84.67	4.7	9.1	1	0.53

As mentioned above, the use of pure SF_6 as feed gas of the plasma ion source leads to instabilities in the plasma discharge. This behavior, which has been observed for electronegative gases, leads to a discharge oscillation between higher and lower electron density states [Ch001]. In order to overcome that problem, the ion source was operated with a lower gas pressure corresponding to ($6 \cdot 10^{-7}$ mbar in the differentially pumped source region) than in the normal case with rare gas ($6 \cdot 10^{-6}$ mbar). Measured under these conditions, the frequency of the plasma oscillations is observed to decrease, thus making useful experiments with the extracted ion beam possible. The same observations have been previously pointed out by Chabert et al. [Ch001] and Corr et al. [Co003]. They demonstrated that the frequency of the oscillations in the discharge plasma of SF_6 or oxygen increases with increasing gas pressure according to a power law described by approximately $p^{1.5}$, $p^{0.5}$ for oxygen and SF_6 (Fig. 44) respectively . According to last estimate in the case of SF_6 the oscillation frequency at pressure $6 \cdot 10^{-7}$ mbar is lower by three times than at pressure of $6 \cdot 10^{6}$ mbar.

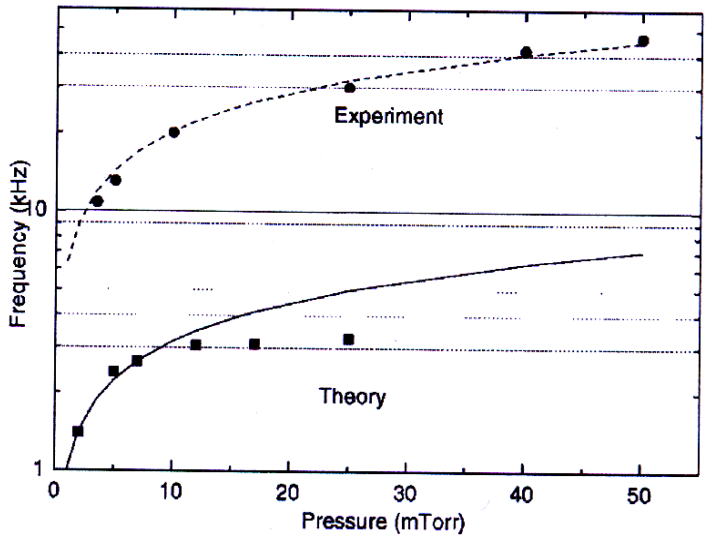

Figure 44: Frequency of the instability as a function of pressure: measured (circles) and calculated (squares). The curves are proportional to the square root of pressure $\sqrt{p}$ [Ch001].

The operation of the ion source under these conditions is not so easy, because the breakdown of discharge current and the rise up of discharge voltage will rapidly take place, if the pressure in the differentially pumped source region passes below a critical limit which corresponds to around $9 \cdot 10^{-7}$ mbar.

Fig. 45 displays the typical ion beam currents of different projectiles that are delivered under these conditions. It is seen that the projectile ion current

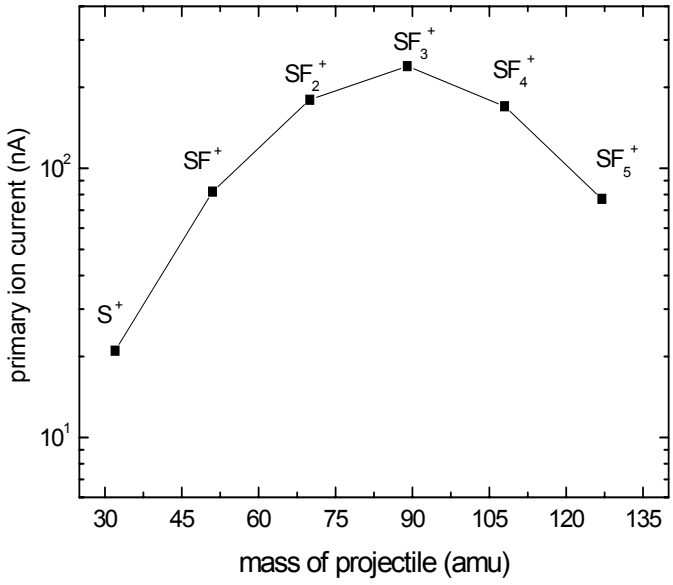

Figure 45: Projectile ion current delivered by the ion source operated with pure SF_6 gas versus mass of different projectiles (SF_m^+ with $m = 1, ..., 5$).

increases with increasing projectile nuclearity, until maximal for SF_3^+ projectile then decreases with further increase of projectile mass. The same observations on generating primary ions containing fluorine by using a plasma ion source similar to that employed here have been previously made by Reuter ([Re84], [Re87], [Re88a]), who has used different feed gases (CF_4, CF_4/O_2, CF_4/N_2 and C_nF_{2n+2} with $n = 3$) and Coburn [Co77]. In all cases, CF_3^+ was the predominant species extracting from the ion source.

7.3.2 Neutral clusters

Fig. 46 shows mass spectra of post-ionized sputtered neutral atoms and clusters emitted from a polycrystalline silver surface under bombardment with 10-keV SF_m^+ (with $m = 1, .., 5$) ions. For comparison, the spectrum obtained with 10-keV Xe^+ projectiles is also included.

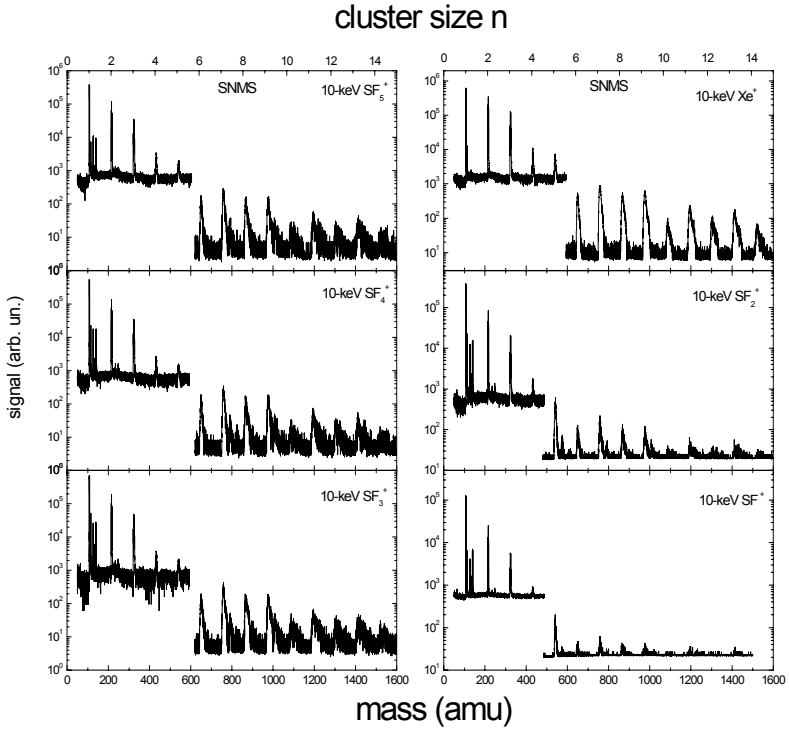

Figure 46: Mass spectra of post-ionized neutral atoms and clusters sputtered from a polycrystalline silver surface under bombardment with 10-keV Xe^+ and SF_m^+ ($m = 1, \ldots, 5$) projectile ions incident under 45^o with respect to surface normal. Post-ionization laser: 193 nm $\approx 10^7$ Wcm^{-2}.

Again, the different traces depicted in each panel were recorded with direct charge digitization or single ion pulse counting, respectively. As before the conversion factor F_{amp} between both spectra was determined from the overlapping signals of Ag_5 and Ag_6 leading to average value of $F_{amp} = 550 \pm 50$

In addition, the signals of sputtered monomers and dimers were blanked from reaching the detector during acquisition of the pulse counting spectra of larger clusters in order to avoid detector saturation. It is seen that sputtered neutral clusters containing up to 14 atoms can be identified under bombardment with Xe^+, SF_5^+, SF_4^+ SF_3^+ and SF_2^+, whereas with SF^+ projectiles clusters

containing up to 11 atoms can be detected. As a general observation, the signal intensity of clusters recorded under SF_m^+ bombardment is rapidly decreasing with increasing cluster size n. As mentioned previously, the mass spectrum obtained under Xe^+ is relatively clean, while small peaks corresponding to Ag_nF and Ag_nS clusters are observed under SF_m^+ bombardment.

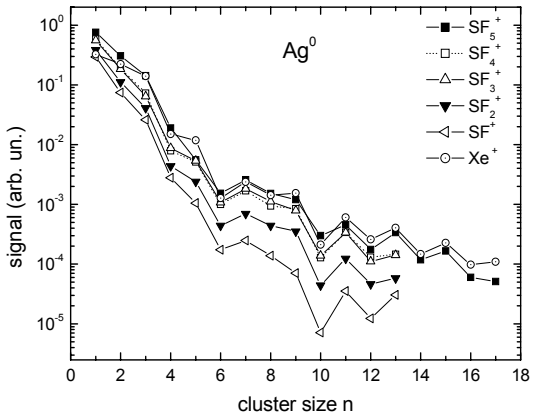

Figure 47: Integrated signal of post-ionized neutral Ag atoms and Ag_n clusters sputtered from a polycrystalline silver surface under bombardment with 10-keV Xe^+ and SF_m^+ ($m = 1, ..., 5$) ions versus cluster size n. The data have been normalized to the primary ion current in order to allow direct comparison between different projectiles.

For a more quantitative evaluation, Fig. 47 shows the integrated signals of sputtered neutral clusters normalized to the primary ion current as a function of cluster size. Since all other experimental parameters are identical, the difference between the curves directly represents the variation of the respective neutral yields induced by different projectiles. It is apparent that the yields of neutral silver atoms and clusters ejected from a silver surface under SF_m^+ bombardment increase systematically with increasing projectile nuclearity m. In addition, the enhancement of sputter yields between different projectiles is small for Ag atoms and dimers and increases with increasing sputtered cluster size n. These findings are in accordance with those already observed for sputtered indium In_n clusters. As mentioned in section 7. 2. 2, it is evident that the partial sputtering yields of silver do not change significantly between Xe^+ and SF_5^+.

7.3.3 Secondary cluster ions

Mass spectra of secondary cluster ions emitted from a polycrystalline silver surface under bombardment with 10-keV Xe^+ and SF_m^+ ions are illustrated in Fig. 48.

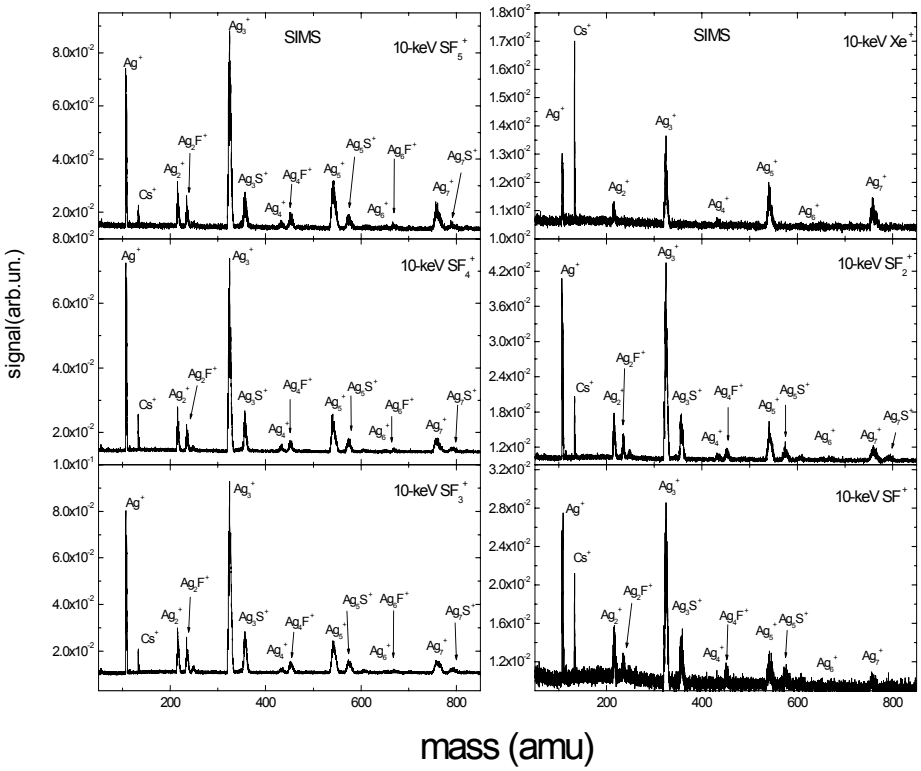

Figure 48: Mass spectra of positive secondary cluster ions sputtered from a polycrystalline silver surface under bombardment with 10-keV Xe^+ and SF_m^+ $(m = 1, \ldots, 5)$ projectile ions incident under 45^o with respect to surface normal. The data have been normalized to the primary ion current in order to allow direct comparison between the different projectiles.

At the first sight, it is important to note that the spectra are very similar for different projectile ions. All spectra are recorded in the analog detection mode for small clusters up to 7 atoms and in the pulse counting mode for larger clusters. We display here only the spectra recorded in the analog mode. The data have been normalized to the primary ion current in order to allow direct comparison between the different projectiles. It is seen that the intensity of Ag_n^+ clusters ions induced by SF_2^+ , Xe^+ and SF^+ are quite low compared with those by SF_5^+, SF_4^+ and SF_3^+ bombardment. As the indium case, maximum intensity is observed for SF_3^+ projectile ions.

It is of interest to note that the F and S atoms are mainly combined with even and odd cluster ions respectively. On the other hand, none of them combines with the monomer. This effect can be attributed to the different electron configuration between odd and even clusters. Since odd-n clusters have an even number of valence electrons, whereas even-n clusters have an odd number of

valence electrons. Therefore, an F atom gains one electron and forms a strong bond with even clusters, since the remaining even number of electrons is spin-paired and therefore bonding in character. On the other hand, an S atom gains two electrons and forms sulfuric components with odd Ag_n^+ cluster ions, again leaving, the remaining even number of valence electrons in a spin-paired state.

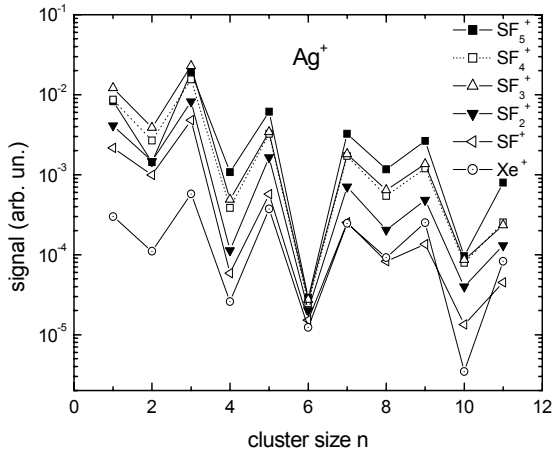

Figure 49: Integrated signal of positive secondary Ag^+ and Ag_n^+ cluster ions sputtered from a polycrystalline silver surface under bombardment with 10-keV Xe^+ and SF_m^+ ($m = 1, ..., 5$) ions versus cluster size n. The data have been normalized to the primary ion current in order to allow direct comparison between different projectiles.

By comparison between SIMS and SNMS spectra (Fig. 48 and Fig. 46), it is noted that AgF and AgS clusters appear in the SNMS spectra, whereas none of them are observed in the SIMS spectra. About the reason for this finding we can only speculate. It is conceivable that the Ag donates one 5s electron to the AgF bond and, hence, AgF is a stable molecule with strong ionic bond character Ag^+F^-. On the other hand, the formation of AgF^+ takes that bonding e^- away that leads to the AgF^+ being unstable. Similar behavior occurs between an S atoms and the Ag i.e., AgS is stable, whereas AgS^+ is unstable.

Fig. 49 shows the integrated signals of secondary Ag^+ ions and Ag_n^+ cluster ions normalized to the primary ion current as a function of cluster size. As for the sputtered neutral clusters, the difference between the curves directly represents the variation of the respective secondary ion yields produced by the different projectiles. The first important observation is that in all cases of SF_m^+ projectile bombardment the yields of secondary ions are higher than those produced under Xe^+ bombardment. A similar enhancement was observed when a Si (100) surface is bombarded with SF_5^+ and SF^+ in comparison to Xe^+ [Ya98]. A second important observation is the secondary ions yields of monomers and dimers under SF_3^+ bombardment are higher compared to

those produced by other projectiles. This finding is surprising because one would intuitively expected the highest secondary ion yields for the projectile containing the largest number of fluorine atoms (SF_5^+).

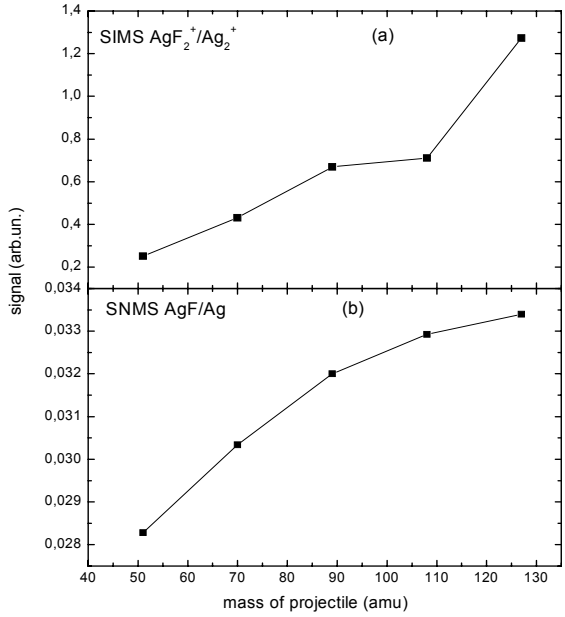

Figure 50: (a) The ratio between the integrated signal of Ag_2F^+ and Ag_2^+. (b) The ratio between the integrated signal of AgF and Ag as a function of projectile mass.

In order to determine approximately the equilibrium concentration of fluorine on the silver surface, we normalize the integrated signal of Ag_2F^+ to that of Ag_2^+ cluster ions. The results, depicted in Fig. 50(a), indicate that the fluorine surface concentration increases monotonically with increasing projectile nuclearity. That indicates the most uptake of fluorine atoms onto the target surface occurs for SF_5^+ rather than SF_3^+projectiles. This finding is corroborated by the fact that the ratio of AgF and Ag-SNMS signals exhibits qualitatively the same trend [cf. Fig. 50(b)]. On the basis of these observations, we conclude that the largest silver ion yields obtained with SF_3^+ projectiles cannot be solely attributed to the fluorine surface concentration.

7.3.4 Ionization probabilities

In fact that we cannot determine absolute values of the ionization probabilities due to the fact that the post-ionized signal in the SNMS is not saturated. However, we can deduce relative variations of these quantities between different

projectiles by calculating the ratio of silver ionization probabilities produced by SF_m^+ to that produced by Xe^+ :

$$\alpha^+_{\mathrm{Ag}_n}\text{enhancement} = \frac{\alpha^+_{Ag_n}(\mathrm{SF}_m^+)}{\alpha^+_{Ag_n}(\mathrm{Xe}^+)} \tag{94}$$

The evaluated results as a function of cluster size n are displayed in Fig. 51

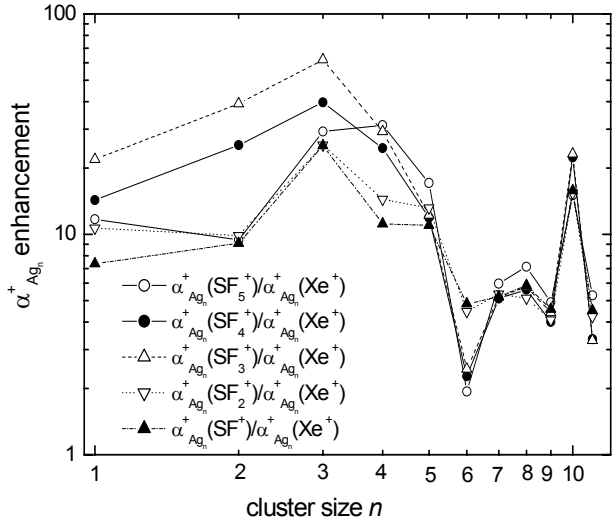

Figure 51: $\alpha^+_{\mathrm{Ag}_n}$ enhancement upon transition from Xe^+ to $SF_m^+(m = 1, ..., 5)$ projectiles as a function of cluster size n.

It is apparent that for all SF_m^+ projectiles the ionization probabilities of Ag atoms, dimers and trimers are higher compared to those produced by Xe^+ by factors ranging from 7 to 22 for atoms, from 8 to 35 for dimers and from 18 to 50 for trimers. The largest enhancement of ionization probabilities is observed for SF_3^+ projectiles similar to that found for indium (Section 7. 1. 5)

7.3.5 Total sputtering yields

In order to calculate the total sputtering yields of silver for different projectiles, the neutral signals $S(n)$-normalized to the primary ion current-presented in Fig. 47 are summed according to

$$Y_{tot}\alpha\sum_n n \cdot S\,(n) \tag{95}$$

Due to fact that the post -ionization process is not saturated, the data must be corrected for the different photoionization cross sections of different sputtered neutral species. For that purpose, we use respective data for sputtered silver atoms and clusters post-ionized by 157 nm radiation that have been determined by Wahl [Wa94], [St2000]. The corrected data are displayed in Fig. 52(a)

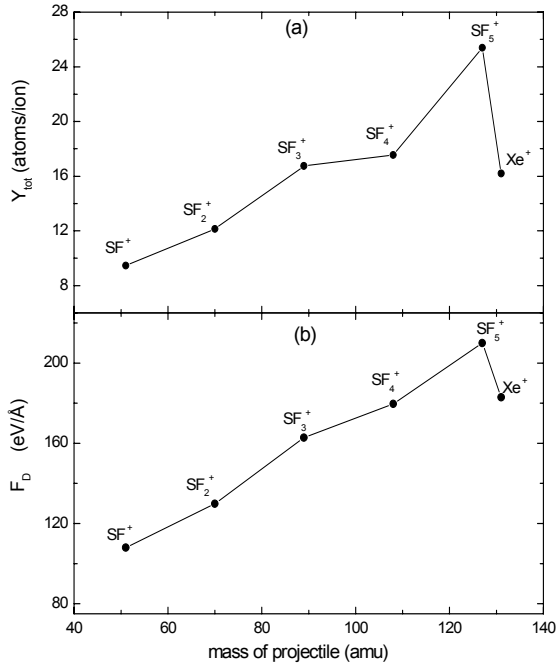

Figure 52: (a) Total sputtering yield of polycrystalline silver under bombardment with different 10-keV projectile ions and (b) energy F_D deposited at the surface for impact of different 10-keV projectiles onto indium as a function of projectile mass (calculated by SRIM).

From the data measured here, only the relative variation of the total yield between the different projectiles can be determined. In order to arrive at absolute values on the ordinate axis, the data have been normalized to a yield value of 16.2 atoms/ion which was obtained from experimental sputtering yield data for Ag target under 10-keV Xe^+ bombardment [An81]. Note that this yield value is low because the data in ref.[An81] were measured under normal impact angle, while our data are taken under 45° impact angle. However, the relative trends remain unaffected by this fact. It is important to note that for the set of isoenergetic SF_m^+ projectiles the total sputtering yields increase linearly with increasing fluorine nuclearity m in the projectile. In addition, the total sputtering yield produced under Xe^+ bombardment is lower than those produced by SF_5^+ and SF_4^+. This finding confirms that the projectile mass is

not the dominant influence since otherwise the total sputtering yield produced by SF_5^+ and Xe^+ would be expected to be the same because these ions have almost equal mass. In contrast, the results can be understood on the basis of a projectile size effect, in which the polyatomic projectiles such as SF_5^+ collide with several atoms at the target surface. The number of atoms which participate in the collision increases with the size of the projectile. The disintegration of SF_5^+ projectiles to S and F atoms will lead to an increased energy deposition at the surface in comparison with the Xe^+ projectile, thereby producing higher sputtering yield than Xe^+.

In order to clarify this point some more, we will evaluate the deposited energy F_D for different projectiles. For that purpose, the same procedure as outlined in Section 7. 2. 5 is employed. The calculated results are displayed in Fig. 52(b) . It is seen that the deposited energy F_D is predicted to increase with increasing fluorine nuclearity. Moreover, the energy deposited by SF_5^+ is higher than that of Xe^+. This finding is in good agreement with our experimental results depicted in Fig. 52(a). As a consequence, we conclude that the yield enhancement observed as a function of increasing fluorine nuclearity of the projectile is fully understandable in the framework of linear cascade sputtering theory. This observation has already been made for indium targets (see chapter 7. 1) and must therefore be regarded as a general characteristic of the interaction of SF_m^+ projectiles with metal surfaces in the impact energy range studied here. By comparison of the results in Fig. 52(a) and Fig. 52(b), it is found that the yield enhancement with increasing of m up to 4 (with respect to $m = 1$) is quantitatively described be the increase of F_D, while for $m = 5$ (SF_5^+) the yield enhancement is found to be slightly larger than the increase of F_D (factor of 2.5 vs. 1.9 for $m = 5 \implies 1$). The last finding may refer to a small contribution of nonlinear cascades to the sputtering process (spike regime).

7.3.6 Partial sputtering yields

In order to discuss the efficiency of different projectiles with respect to cluster production in sputtering, we again define the relative enhancement factor

$$K_{1,m}(n) = \frac{Y^{rel}_{Ag_n}(SF_m^+)}{Y^{rel}_{Ag_n}(SF^+)} \tag{96}$$

The resulting values are plotted as a function of the cluster size n in Fig. 53

For the set of SF_m^+ projectiles, it is seen that the enhancement observed with increasing m is more pronounced for larger sputtered clusters. The largest effect is observed for Ag_{10}, the production of which is enhanced about 16 times as much as the total sputtering yield upon transition from SF^+ to SF_5^+ projectiles.

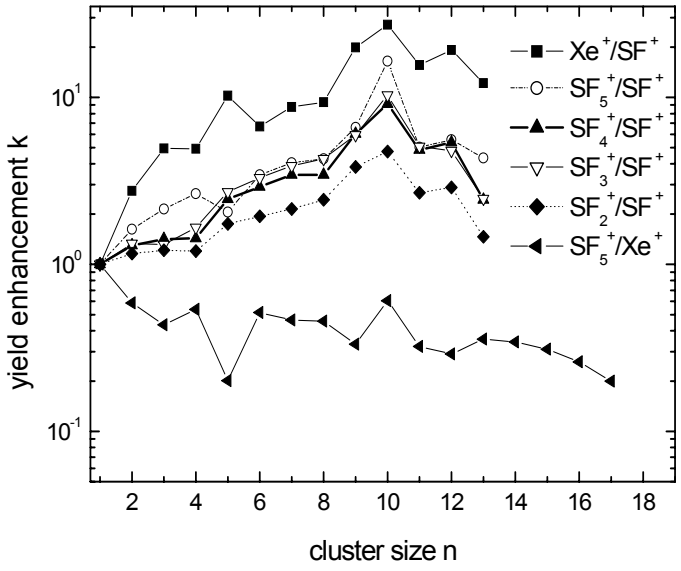

Figure 53: Enhancement factor k [see Eq. (96) for definition] for partial sputter yields of Ag_n clusters upon transition from SF^+ to SF_m^+ and Xe^+ projectiles as a function of cluster size n.

The data presented in Fig. 53 provide clear evidence that the efficiency of cluster production is significantly increased during the progression from SF^+ to SF_5^+ projectiles. The same behavior has been observed for sputtered indium clusters. As mentioned in Section 7. 1. 6 this finding is expected since it has been frequently observed that the relative abundance of sputtered clusters is correlated with the total sputtering yield [Wu002]. More specifically, the cluster abundance distribution is changed in favor of large clusters with increasing total yield as long as atomic projectiles are used. For polyatomic projectiles, it has been demonstrated that this correlation may not be valid any more if the total yield significantly exceeds about 30 atoms/ion, indicating a transition into the "spike" regime of sputtering [He003]. Since all sputter yield values determined here are below that limit, our data fit well into this picture.

Interestingly, the enhancement factors measured for Xe^+ with respect to SF^+ projectiles are clearly higher than those determined for SF_5^+. Hence, Xe^+ is more efficient in producing sputtered clusters than SF_5^+ and other SF_m^+ projectiles with smaller m . Particularly the former finding appears surprising, since the monoatomic Xe^+ projectile will penetrate deeper into the solid, leading to less deposition of energy immediately at the surface. As a consequence, the total sputtering yield imposed by Xe^+ impact is smaller than those induced by SF_5^+ projectiles, and one would therefore expect lower cluster abundances for Xe^+. The fact that such a behavior is not observed here may relate to the

incorporation of projectile species (S and F atoms) into the target surface. The argument is the same as for indium in Section 7. 1. 6 and will not be repeated here. The effect will lead to a suppress ion of the formation of large sputtered clusters under SF_5^+ bombardment in comparison with Xe^+.

7.3.7 Conclusion

The following main points can be extracted from the experiments described above:

- The enhancement observed of silver secondary ion yields under SF_m^+ ($m = 1, ..., 5$) bombardment is predominantly caused by an increased ionization probability of sputtered particles rather than by enhanced partial sputtering yields.
- Monatomic Xe^+ projectile is more efficient in producing sputtered clusters than polyatomic SF_m^+ ($m = 1, ..., 5$) projectiles.
- For set of isoenergetic SF_m^+ projectiles, the total sputtering yield is found to increase linearly with increasing projectile nuclearity m. This increase can be almost fully explained by linear cascade sputtering theory.
- For SF_5^+ projectiles, the obtained total sputtering yield is slightly larger than that estimated from linear cascade theory. The finding may refer to small contribution of nonlinear cascades to the sputtering process (spike regime).

7.4 Investigation of the bombarded surface by X-ray Photoelectron Spectroscopy (XPS)

In order to obtain more information about the surface chemistry of silver subjected to SF_m^+ bombardment and to determine the concentration of fluorine at the bombarded surface as a function of projectile nuclearity, the experiment was repeated in a different ultrahigh vacuum system containing an X-ray photoelectron spectrometer (VSW). The instrument is equipped with a twin anode (Mg Kα, Al kα) X-ray source. The spectrometer was interfaced to an VSW computer system for signal averaging. It is well known that X-ray photoelectron spectroscopy (XPS) was widely used as technique for the investigation of solid surfaces. It gives information on elemental composition as well as electronic states in the surface region of materials [Br90]

7.4.1 Physical basis of XPS

In general the photoelectron spectroscopy is based on a single photon in/ electron out process i.e. it analyzes the kinetic energy of electrons ejected when a solid is irradiated with monoenergetic photons. Specially, when x-rays were used as the exciting photon source, this technique is called x-ray photoelectron spectroscopy (XPS). In XPS the incident photon is absorbed by an atom in the target surface, thus leading to ionization and emission of core (inner shell) electrons. The kinetic energy distribution of the emitted photoelectrons (i.e. the number of emitted photoelectrons as a function of their kinetic energy) can be measured using any appropriate electron energy analyzer.

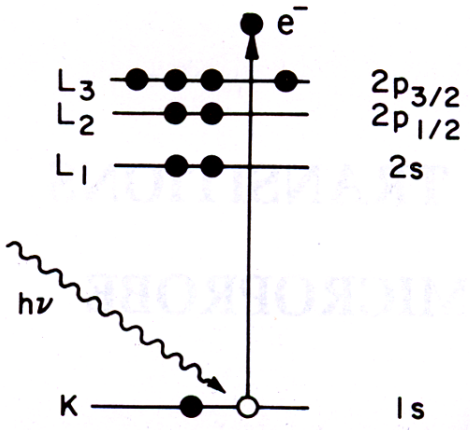

Figure 54: Schematic of photoemission process

By principle of energy conservation, the photoionization process (Fig. 54) can be described according to the equation

$$E_{Kin} = h\upsilon - E_B - \phi \tag{97}$$

where E_{Kin} is the measured electron kinetic energy, $h\upsilon$ the photon energy of the exciting radiation, E_B the binding energy of the electron in the solid and ϕ is the work function. Due to fact that core levels are ionized, E_B is only weakly affected by the chemical bond and thus characteristic of the atom absorbing the photon.

The most important advantages of XPS are:

i) It can be used to identify and determine the concentration of different elements in the sample. As for each element, there will be a characteristic binding energy associated with a core atomic orbital i.e. each element will give rise to a characteristic set of peaks in the photoelectron spectrum at kinetic energies determined by the photon energy and the respective binding energies. Therefore, the presence of peaks at particular energies indicates the presence of a specific element in the sample under study. Furthermore the intensity of peaks is related to the concentration of the element within the sample. Thus, the technique provides a quantitative analysis of the surface composition and is sometimes known by the alternative name, Electron Spectroscopy for Chemical Analysis (ESCA)

ii) In addition, the XPS is able to provide information about the chemical bonds of the detected atoms:

The exact kinetic energy of the photoelectron depends not only upon the level from which photoemission is occurring, but also upon: (1) the formal oxidation state of the atom and (2) the local chemical and physical environment. The changes in either (1) or (2) give rise to small shifts in the peak positions in the spectrum, so called *chemical shifts*. Such shifts are readily observable and interpretable in XPS spectra, since this technique features a of high intrinsic resolution (as core levels are discrete and generally of a well defined energy) basically a one electron process, thus simplifying the interpretation. In the present work we have utilized the XPS for the two previous advantages.

XPS spectrum

Fig. 55 shows a typical photoelectron spectrum from a polycrystalline metallic silver sample obtained with Mg kα excitation ($h\upsilon$ = 1253 eV).The peaks in the spectrum denote kinetic energies corresponding to photon-excited electronic states in the metal. The 3s, 2p, 3d, 4p as well as 4d lines are clearly seen, the most prominent lines are the $3d_{3/2}$ and $3d_{5/2}$. Photoemission from p and d electronic states with nonzero orbital angular momentum produces a spin-orbit doublet such as the $2p_{1/2}$-$2p_{3/2}$ and $3d_{3/2}$-$3d_{5/2}$ lines as shown in Fig. 55.

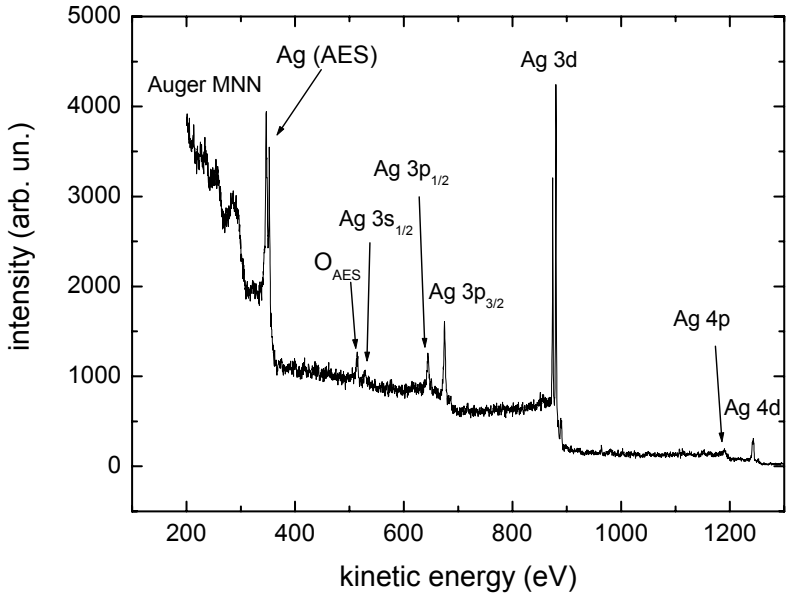

Figure 55: X-ray photoelectron spectrum of a polycrystalline silver excited by Mg Kα ($hv = 1253$ eV)

The two lines correspond to two states with $j = l + 1/2$ and $j = l - 1/2$. In addition, a photon induced Auger (AES) peak for oxygen is clearly observed, which can be attributed to a KLL Auger de-excitation process following photon ionization of the k-shell. From Fig. 55 it is evident that every peak is accompanied by an increased background intensity at the low kinetic energy side. This tail (defined as the background signal associated with the peak) corresponds to electrons that suffered inelastic scattering and energy loss within the material before being emitted into the vacuum. When attempting to resolve a complex photoelectron peak into its individual components, corresponding to different chemical environments (coordination states) of the element giving rise to the peak, it is essential to remove the background. Such peak resolution is most important aspect of the data processing XPS spectra since without the possibility of performing it unambiguously both the inherent chemical information and the ability to quantify are lost [Ri90]. As a consequence, the background signal considers a major problem in the application of X-ray photon electron spectroscopy to surface analysis. In order to determine the true peak area or line shape, the background signal must be removed. For this purpose several methods have been developed, the most important of them will be briefly outlined in following

i) **Linear integration**

In this method, the background intensity as a function of electron kinetic energy is approximated by simply drawing a straight line between two suitably chosen points such as a and b in Fig. 56. The interpolated background signal is then subtracted before integrating the peak. This method is easy and quick, and if used in a consistent manner throughout a series of spectra from the same material, will give good relative accuracy, although not good absolute accuracy. The linear integration method has already been available in our data handling system.

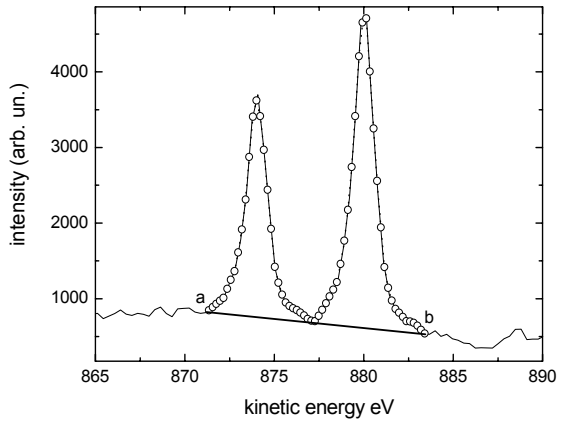

Figure 56: Photoelectron peaks ($3p_{1/2}$, $3p_{2/3}$) of metallic silver showing linear integration method for background subtraction.

ii) **Shirley method**

In this method the background intensity at each point is determined by an iterative analysis to be proportional to the intensity of the total peak area above the background and to higher energy [Sh72]. That means, for each photoelectron ejected at a particular energy there is a flat background at lower energies. Thus the true intensity at energy E can be expressed as

$$I_t(E) = I_{obs}(E) - K \int_0^E I_t(y)\, dy \tag{98}$$

where $I_{obs}(E)$ is the observed intensity at E that includes the background and K a proportionality constant that is determined by matching the calculated to the observed background at some chosen energy below the peak.

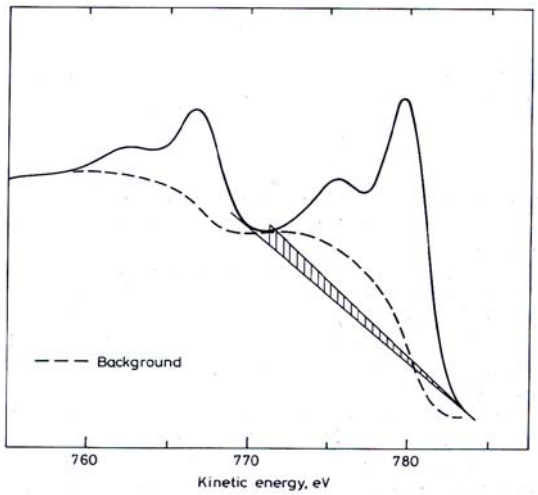

Figure 57: Spectrum simulated by Bishop, corresponding to equal amounts of metallic Fe and Fe_2O_3. The dashed line is the shape of the shirley background calculated according to Eq. (98). The two straight lines indicate two possible positions of a linear background[Br90].

Fig.57 shows the curved background calculated by Shirley's method. It is important to note that, the basic form of Shirley background assumes that for each photoelectron ejected at a particular energy there is a constant probability to contribute to the background at lower energies. This seems a fair approximation for metals since extrinsic events (inelastic scattering) of small energy loss can occur by exciting electrons from just below to just above the fermi level. However, for insulators this is no longer possible and there should be a clearly observed energy interval after the peak, before the background rises on the low energy side, proportional to the band gap [Br90]. In the present work we investigated only a metallic sample, therefore the shirley's method may give reliable results.

iii) Tougaard method

Tougaard [To82], [To86] has used the basis of a physical model for electron transport in solids (deconvolution model) to remove the background in an XPS spectrum. If $j(E)$ is the measured flux of emitted electrons at energy E from a homogeneous solid, the primary excitation spectrum $F(E)$ is given by

$$F(E) = j(E) - \lambda \int_E^\infty K(E' - E) j(E') dE' \tag{99}$$

where $K(E'-E)$ is the probability that an electron of energy E shall lose energy $E' - E$ per unit path length traveled in the solid, while λ is the mean free path for inelastic electron scattering. In the derivation of Eq. (99) it is assumed that the cross section for inelastic scattering is identical for all electrons within the

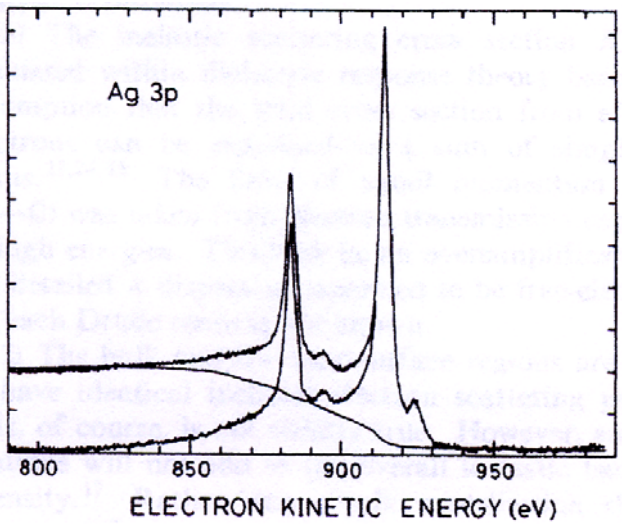

Figure 58: Upper curve is the experimental photoelectron spectrum of silver and lower curve is the primary excitation spectrum as determined by Eq. (99). The difference curve is the background signal of inelastic scattered electrons. The spectrum was recorded by using Al Kα x-rays to excite the core electrons [To86]

spectrum to be deconvoluted. Equation (99) takes into account the background produced by all multiple inelastic scattering events. If the elastic scattering may be characterized by an exponential attenuation length L, then λ in Eq. (99) becomes replaced by $\lambda L/(\lambda + L)$. Then a deconvolution formula is given by

$$F(E) = j(E) - \lambda L/(\lambda + L) \int_E^\infty K(E' - E) j(E') dE' \qquad (100)$$

The energy loss in inelastic scattering $K(E'-E)$ may be calculated theoretically from the dielectric response theory. Tougaard has found excellent results by applying the deconvolution formula Eq. (99) to many peaks in copper, silver, gold [To86] and aluminum [To87]. Unfortunately, the Tougaard method is not available in the program package of our data handling system.

7.4.2 Experimental conditions

The experiments are performed in an VSW analysis system containing :

(i) A twin anode (Mg Kα, Al kα) X-ray source that is used to excite the investigated surface

(ii) An electron energy analyzer (hemispherical analyzer VSW HA5000) that can disperse the emitted electrons according to their kinetic energy and thereby measure the flux of emitted electrons of a particular energy.

In order to establish identical sputter equilibrium conditions as in the TOF-MS experiments, the Atomika ion source has been mounted on the XPS system to generate the projectile ions. All components are housed in an ultrahigh vacuum chamber (analysis chamber) with a base pressure ranging from 10^{-9} to several 10^{-10} mbar. The sample was cleaned in an ultrasound bath containing isopropanol, then it is introduced in the first chamber (sample preparation chamber). This chamber will be pumped down to a vacuum below 10^{-6} mbar. When the proper vacuum has been achieved, the sample is transferred into the analysis chamber.

7.4.3 Measurements procedure

- For better stability of the discharge, the ion source is operated with a gas mixture of Ar and SF_6 gas as mentioned previously in Section. 4. 1. 4
- Prior to each experiment, the sample sputter cleaned by 10-keV Ar^+ ion bombardment to remove any contaminations. After that an XPS spectrum is recorded (Fig. 55). This spectrum is then utilized as a standard for clean silver metal. Note that the bombarding ions collide with the target surface at impact angle of 46° which is approximately similar to that of the TOF-MS measurements.
- The cleaned silver sample is then bombarded with SF_m^+ $(m = 1, ..., 5)$ ions at the same impact energy of 10-keV with a sufficiently high fluence to achieve sputter equilibrium conditions (fluence= $\frac{30 \cdot 10^{-9}\ \mathrm{A} \cdot 5 \cdot 60\ \mathrm{s}}{0.25\ cm^2 \cdot 1.6 \cdot 10^{-19}\ \mathrm{As}} \simeq 2.25 \cdot 10^{14}\ ions/cm^2$). In fact, the generation of the target surface for XPS study is not trivial due to the acceptance area for the XPS being much larger than the raster scanned ion bombarded area [Re87], [Nö74]. To overcome this problem, the following measure were taken:

(i) The objective lens of the ion source is switched off to get large ion beam diameter (1 mm). In addition, the ion beam is scanned i.e., moved line by line over the target surface

(ii) A total 25 of overlapped areas of the target surface have been raster bombarded. In order to determine the bombarded area by XPS spectrometer

the target is translated in two directions horizontally and vertically (x, y) and the photoelectron spectrum is recorded as a function of x, y coordinates. Such study is very important to determine the best position to record the XPS spectrum, the results are displayed in Fig. 59.

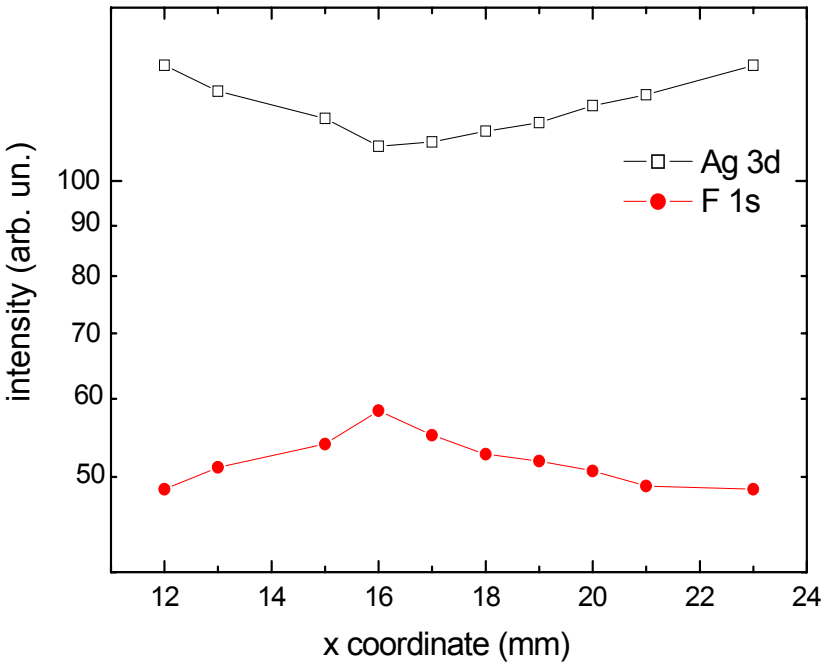

Figure 59: The dependence of Ag 3d and F 1s signals on the variation of x coordinate distance.

The data in Fig. 59 give a good picture about the behavior of both fluorine and silver concentration as a function of position on the sample surface. When the signal of Ag 3d decreases, the signal of F 1s is increasing. That behavior is expected because the XPS signal is related directly to the atomic concentration of an element on the sample under investigation. More clearly, most of the sample here is clean silver and there is only a small area on the sample containing F atoms due to the bombardment with SF_m^+ projectile ions. In the center of the bombarded spot, the XPS signal of silver exhibits a local minimum, accompanied by a local maximum of the fluorine signal. Based on that conclusion, all spectra of XPS in further investigations were recorded at these coordinates.

7.4.4 Results

Fig. 60 shows the photoelectron spectra of metallic silver after bombardment with different SF_m^+ projectile ions. The spectra are recorded by using Mg Kα x-ray photon at energy of 1253 eV.

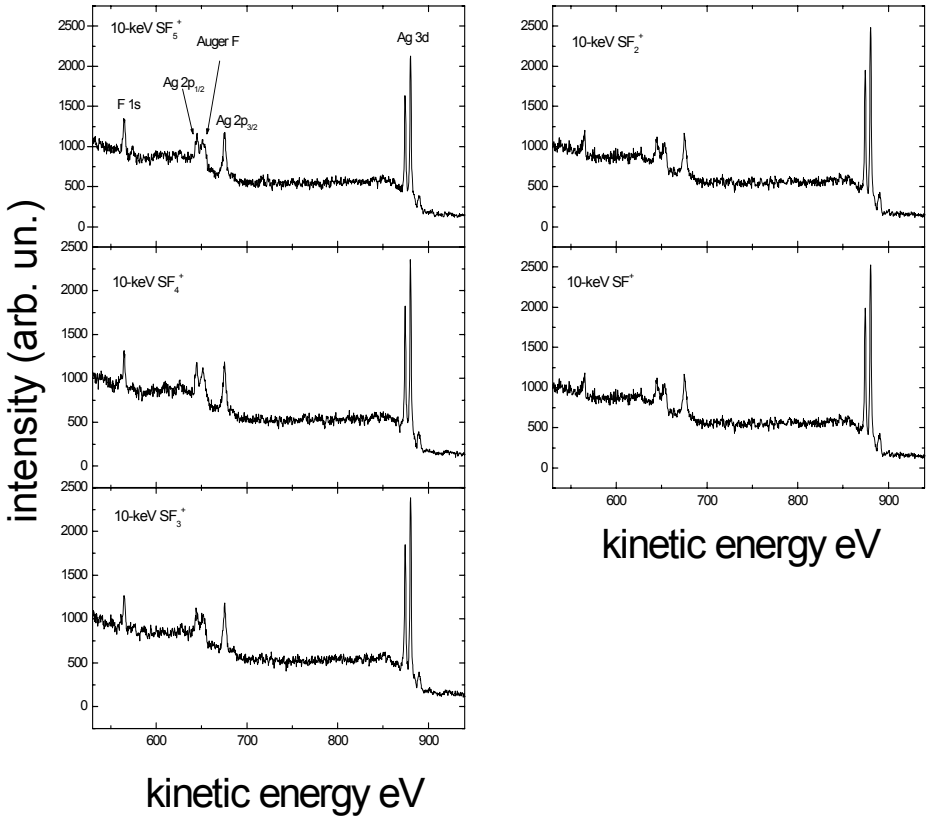

Figure 60: X-ray photoelectron spectra of a polycrystalline silver excited by Mg Kα (1253 eV). The spectra are recorded after the target surface was bombarded with 10-keV SF_m^+ ($m = 1, ..., 5$) projectiles.

The setting parameters of X-ray source are:

X-ray source voltage kV	8.5
filament current (A)	2.3
emission current (mA)	5

It is seen that the peaks corresponding to F (1s), Ag (2p) and Ag (3d) are clearly observed. The F (1s), Ag (2p) and Ag (3d) kinetic energies are found to

be 564.5, 675 and 880 eV, respectively. These findings are in good agreement with literature data [Cr99]. As mentioned previously, to obtain a quantitative information from the photoelectron spectrum, the background signals must be removed. To achieve this, we used the Shirley method to remove the background signal. Fig. 61(a) shows the behavior of fluorine signals for different projectiles after removal of the contribution of background signals.

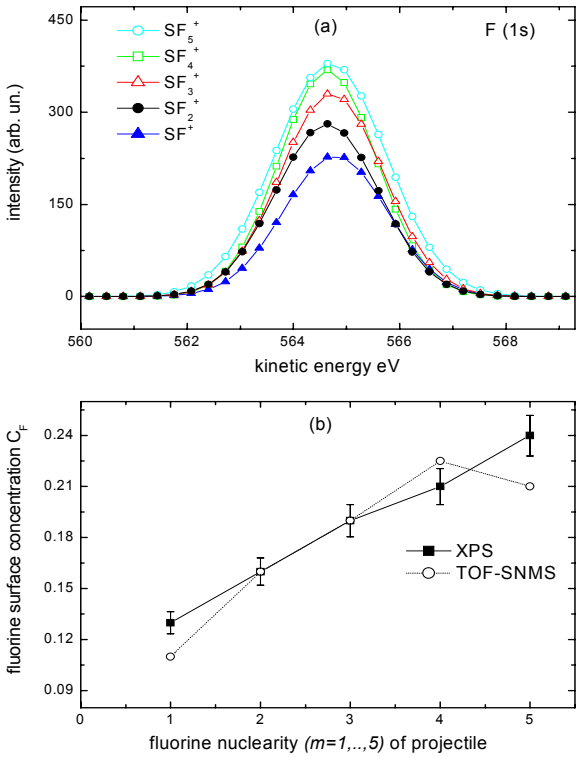

Figure 61: (a). The F (1s) region of the XPS spectra after bombardment of a polycrystalline silver with 10-keV SF_m^+ ($m = 1, ..., 5$) projectiles. (b) Fluorine surface concentration C_F as a function of fluorine nuclearity m in projectile (solid and dot lines are results from the data of XPS and TOF-SNMS, respectively).

It is seen that the F (1s) signal is increased with increasing fluorine nuclearity in projectile. In order to determine the concentration of fluorine on the target surface, the ratio of integrated signals between fluorine and silver is calculated for different projectiles. The resulting data is calibrated with the ratio of integrated signals of fluorine and silver in XPS spectrum of silver-fluoride (AgF) powder that contains on 1/1 for F and Ag respectively. The calculation was done according to the following equation:

$$\frac{C_F}{C_{Ag}} = \frac{I_F}{I_{Ag}} \cdot \frac{I_{Ag}^{AgF}}{I_F^{AgF}} \cdot \frac{C_F^{AgF}}{C_{Ag}^{AgF}} \tag{101}$$

Where C_F, C_{Ag} denote the concentrations of fluorine and silver at the bombarded surface, respectively. I_F , I_{Ag} are the integrated signals of fluorine and silver in the photoelectron spectrum of the bombarded surface. I_{Ag}^{AgF}, I_F^{AgF} are the integrated signals of fluorine and silver in the photoelectron spectrum of silver-fluoride AgF. C_F^{AgF}, C_{Ag}^{AgF} are the concentration of fluorine and silver of silver-fluoride AgF, respectively, hence $\frac{C_F^{AgF}}{C_{Ag}^{AgF}} = 1$. The Eq. (101) has been calculated for each projectile and the evaluated results are displayed in Fig. 61(b)

It is shown that the fluorine concentration at the target surface under sputter equilibrium conditions is increased directly with increasing fluorine nuclearity of the projectile ions. This behavior is in good agreement with what one has expected. Fig. 61b (dot line) shows the C_F estimated from the total sputtering yield Y_{tot} and fluorine nuclearity m : $C_F \simeq \frac{m}{Y_{tot}(SF_m^+)}$ where $Y_{tot}\,(SF_m^+)$ is the measured yield by TOF-SNMS (Section. 7. 3. 5 Fig.52a). It is of interest to note that the C_F estimated by XPS and TOF-SNMS is almost the same. From Fig. 61(b) it seen that C_F does not extrapolate to zero when the fluorine nuclearity m in projectile is zero. That behavior is not a prior expected. It may be attributed to:

The effect of the residual gas in vacuum system due to the operation of the ion source:

In the steady state the rate of the sputtered fluorine atoms is equal to the arrival rate of fluorine atoms at the surface [Bl75] :

$$J_p \cdot Y_F = C_F^{\circ} \cdot J_p \cdot Y_{tot} = \frac{6 \cdot s}{\sqrt{2\pi kTM}}(p_{SF_6}), \text{ then:} \tag{102}$$

$$C_F^{\circ} = \frac{6 \cdot s}{J_p \cdot Y_{tot} \cdot \sqrt{2\pi kTM}}(p_{SF_6}) \tag{103}$$

Where s is the sticking probability (coefficient) for SF_6 molecules, J_p is the primary ion current density ($7.5 \cdot 10^{11}$ions/cm^{2}s), Y_F is the partial sputter yield of fluorine atoms, k is the Boltzmann constant, T is the temperature, M is the mass of SF_6 molecules and p_{SF_6} is the pressure (10^{-8} mbar). The left-hand term represents the rate at which fluorine is sputtered, and the right-hand term represents the arrival rate of fluorine atoms from the gas phase. From Eq. (103) it is possible estimate the fluorine surface concentration C_F° caused by residual gas adsorption. By inserting into the Eq. (103) the following parameters: $Y_{tot} \simeq 10, J_p = \frac{30 \cdot 10^{-9}\ \mathrm{A}}{1.6 \cdot 10^{-19}\mathrm{As} \cdot 0.25\ \mathrm{cm}^2} = 7.5 \cdot 10^{11}$ions/cm^{2}s, $p_{SF_6} \simeq 10^{-8}$ mbar,

$k = 1.38 \cdot 10^{-23}\ J \cdot K^{-1}$, $T = 300\ K$ and $M = 146 \cdot 1.66 \cdot 10^{-27}$ amu: then we obtain $C_F^{\circ} = s$

In fact, we did not found in literature any information about the sticking probability of SF_6 at room temperature. However, the SF_6 is inert gas and, hence, its sticking probability should be small at room temperature.

Chemical shift

The change of chemical state of the silver surface bombarded under 10-keV SF_m^+ $(m = 1, ..., 5)$ projectiles can be observed by comparison of the obtained XPS spectrum with the corresponding spectrum of pure metallic silver (Fig. 62b).

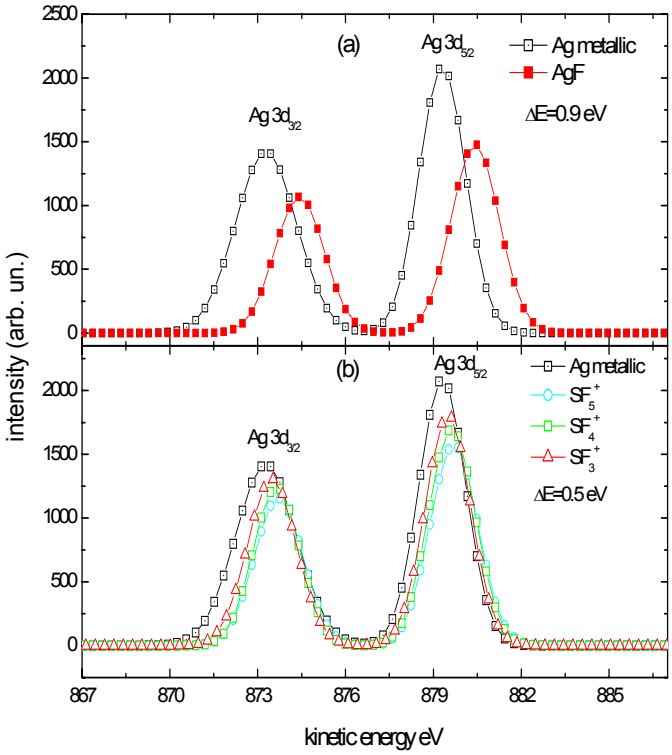

Figure 62: (a) The Ag (3d) region of the XPS spectra of Ag metallic and silver-fluoride AgF. (b) The Ag (3d) region of the XPS spectra of Ag metallic and silver bombarded with 10-keV SF_m^+ $(m = 1, ..., 5)$ projectiles.

It is seen that the electron kinetic energy of Ag 3d is increased (for SF_5^+) by $\simeq 0.5$ eV in comparison with kinetic energy of Ag 3d of pure metallic silver. Thus indicating that the silver-fluoride has been formed. This finding is in good

agreement with the published data of Gaarenstroom [Ga77] who pointed out the compounds of AgF, AgF_2 and Ag_2O have binding energies lower (higher kinetic energies) than Ag metal. An important notice on this observation, the chemical shift energy of the bombarded surface is lower than the corresponding of silver-fluoride AgF powder (Fig. 62a). For silver-fluoride AgF the chemical shift is found $\Delta E\left(AgF\right) = 0.9$ eV with respect to the pure metallic silver (Fig. 62a). The difference between the magnitude of chemical shift of the bombarded surface and silver-fluoride AgF may be attributed to: in the case of the bombarded surface with SF_m^+ $(m = 1, ..., 5)$ not all fluorine atoms will be bonded with Ag atoms, on the other hand for silver-fluorinde all fluorine atoms will be bonded with Ag atoms therefore the chemical shift energy is high. Fig. 63a) shows the chemical shift as a function of m , it is found that the ΔE is increased directly with increasing the projectile nuclearity. The data in Fig. 63a) can be used to estimate the C_F by:

$$C_F = \frac{\Delta E\left(m\right)}{\Delta E\left(AgF\right)} \cdot 0.5 \tag{104}$$

The evaluated results are displayed in Fig. 63b) by comparing this figure with Fig. 61b) we found a good agreement

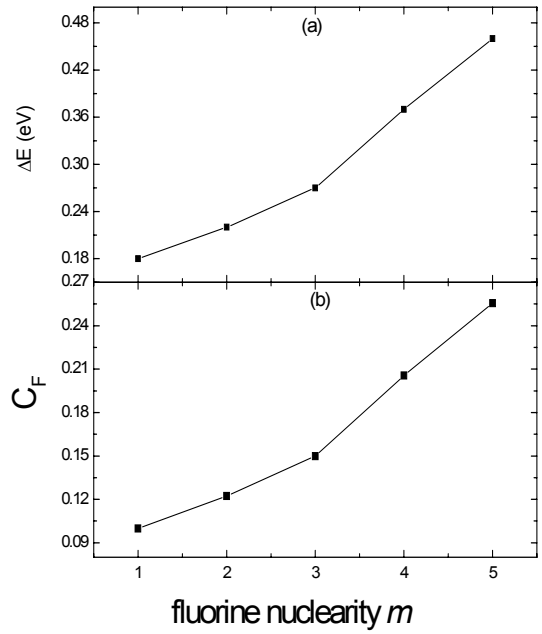

Figure 63: (a) Chemical shift and (b) C_F calculated by Eq. (104) as a function of fluorine nuclearity m .

8 Summary

The sputtering of metal surface clusters under bombardment with polyatomic and monatomic projectiles was investigated experimentally by means of time-of-flight mass spectrometry (TOF-MS) characterizing the composition of the sputtered flux. In order to obtain information about the relative abundance of clusters among the flux of sputtered particles independent of their charge state, mass spectra of both secondary ions and sputtered neutral particles are recorded under comparable experimental conditions. The neutral species are post-ionized prior to mass analysis by means of photo-ionization using a intense of UV laser at a wavelength of 193 nm.

As a first step, the formation of sputtered indium clusters under bombardment with SF_5^+ ($m = 1, ..., 5$) and Ar^+ projectiles is investigated. In these experiments, a photon energy of the ionizing laser (6.4 eV) is larger than the ionization energy of indium atoms (5.79 eV) and all indium clusters In_n. Therefore, the photo-ionization of all neutral species is achieved by absorption of a single photon (SPI) and, hence, a high ionization efficiency and low fragmentation rates have been achieved. In addition, the nuclearity and fluorine content of the projectile is systematically varied. Such conditions give us the possibility to unravel the behavior of the partial sputtering yields and ionization probabilities as a function of the fluorine content and nuclearity of the projectile. The investigations demonstrated that the measured secondary ion signals increase much more than those of the corresponding neutral particles if SF_m^+ projectiles are used instead of Ar^+ ions, indicating that the ionization probability under bombardment with SF_m^+ is enhanced by a chemical matrix effect induced by fluorine incorporation into the surface. Interestingly, the largest values of the ionization probability are observed for SF_3^+ projectiles. The total sputtering yield is found to be larger for SF_m^+ compared to Ar^+ projectiles and to increase linearly with increasing m. Both findings are shown to be understandable in the framework of linear cascade sputtering theory. The partial sputtering yields of In_n clusters exhibit a stronger enhancement than the sputtered monomers, the magnitude of the effect increasing with increasing cluster size and projectile nuclearity.

A second step, the formation of sputtered silver clusters under bombardment with Xe^+ and SF_5^+ bombardment is investigated. It is found that measured Ag_n^+ signals increase significantly if SF_5^+ projectiles are used instead of rare gas Xe^+ ions of the same kinetic impact energy. On other hand, the signals of neutral Ag atoms and Ag_n clusters exhibit only a relatively small increase, thus indicating that the enhancement observed for secondary ions is predominantly caused by an increased ionization probability of sputtered particles under SF_5^+ bombardment rather than by enhanced partial sputtering yield. The mass distribution of sputtered particles does not change in favor of large clusters

between SF_5^+ and Xe^+ projectiles This finding shows that the use of polyatomic SF_5^+ projectiles does not lead to a higher efficiency in producing sputtered clusters.

Expanding on the comparison between Xe^+ and SF_5^+ projectiles, we have investigated the influence of fluorine projectile nuclearity on sputtering of silver by bombarding the target surface under SF_m^+ ($m = 1, ..., 5$) projectiles. The results demonstrated that the total sputtering yield produced by a set of isoenergetic SF_m^+ projectiles is increased linearly with increasing projectile nuclearity m. This increase can be almost fully explained by linear cascade sputtering theory. For SF_5^+ projectiles the obtained total sputtering yield is slightly larger than that estimated from linear cascade theory. The finding may refer to small contribution of nonlinear cascades to the sputtering process (spike regime).

Finally, the experiments are repeated in a different ultrahigh vacuum system containing an X-ray photoelectron spectrometer in order to obtain more information about the surface chemistry of silver subjected to SF_m^+ bombardment and to determine the concentration of fluorine at the bombarded surface as a function of projectile nuclearity. The results show that the concentration of fluorine atoms at the bombarded surface increases directly with increasing fluorine nuclearity in the projectile. In addition, the silver peaks of photoelectron spectrum are shifted to higher kinetic energy ranging from 0.2 to 0.5 eV depending on the fluorine nuclearity m . This indicates the existence of silver-fluoride (AgF). These results are largely consistent with those obtained by secondary neutral time-of-flight mass spectrometry (TOF-SNMS).

However, the physical reason for the observed, extraordinarily high ionization probability in the case of SF_3^+ bombardment remains unclear.

References

[An70] C. A. Andersen
Int. J. Mass Spectrom. Ion Phys. **3**, 413 (1970)

[An73] . C. A. Andersen, J. R. Hinthorne: *Thermodynamic Approach to the Quantitative Interpretation of Sputtered Ion Mass Spectra*
Anal. Chem. **45**, 1421 (1973)

[An75] H. H. Andersen, H. L. Bay: *Havy- Ion Sputtering Yield of Silicon*
J. App. Phys. **46**, 1919 (1975)

[An81] H. H. Andersen, H. L. Bay in: *Sputtering by Particle Bombardment I*
Ed. R. Behrisch (Springer, Berlin 1981), p. 145

[An87] H. H. Andersen
Nucl. Inst. Meth. B **18**, 321 (1987)

[An93] H. H. Andersen: *Fundamental Processes in Sputtering of Atoms and Molecules*
Ed. P. Sigmund. SPUT**93**, Copenhagen, 127 (1993)

[An003] H. H. Andersen, A. Johansen, M. Olsen, V. Touboltsev: *Gold Cluster Ranges in Aluminium, Silicon and Copper*
Nucl. Instr. Meth. B **212**, 56 (2003)

[Ap89] A. Appelhans, J. Delmore: *Comparsion of Polyatomic and Atomic Beams for Secondary Ion Mass Spectrometry of Organics*
Anal. Chem. **61**, 1087 (1989)

[Ba71] R. C. Baetzold: *Calculated Properties of Metal Aggregates. II. Silver and Palladium*
J. Chem. Phys. **55**, 4363 (1971)

[Ba83] J. Bartmess, R. Georgiadis
Vacuum. **33**, 149 (1983)

[Be81] R. Behrisch: *Sputtering by Particle Bombardment I*
Springer-Verlag Berlin, 1981

[Be91] R. Behrisch, K, Wittmaak: *Sputtering by Particle Bombardment III*
Springer-Verlag Berlin, 1991

[Be84] C. Becker, K. Gillen: *Surface Analysis by Nonresonant Multiphoton Ionization of Desorbed or Sputtered Species*
Anal. Chem. **56**, 1671 (1984)

[Be97] S. F. Belykh, I. S. Bitensky, D. Mullajanov, U. K. Rauslev: *Nonlinear Effects in Cluster Emission from Solids Induced by Molecular Ion Impact*
Nucl. Instr. Meth. B **129**, 451 (1997)

[Be00a] S. F. Belykh, B. Habets, U. Rasulev, A. Samartsev, L. Stroev, I. Veryovkin: *Relative Yields, Mass Distributions and Energy Spectra of Cluster Ions Sputtered from Niobium under keV Atomic and Polyatomic Gold Ion Bombardment*
Nucl. Inst. Meth. B **165**, 809 (2000)

[Be00b] S. F. Belykh, U. Rasulev, A. Samartsev, L. Stroev, A. Zinoviev: *High Non- Additive Sputtering of Silicon as Large Positive Cluster Ions under Polyatomic Ion Bombardment*
Vacuum. **56**, 257 (2000)

[Be73] A. Benninghoven: *Surface Investigation of Solids by Statistical Method of Secondary Ion Mass Spectroscopy (SIMS)*
Surf. Sci. **35**, 427 (1973)

[Be75] A. Benninghoven: *Developments in Secondary Ion Mass Spectroscopy and Applications to Surface Studies*
Surf. Sci. **53**, 596 (1975)

[Be95] G. Betz, W. Husinsky: *Molecular Dynamics Studies of Cluster Emission in Sputtering*
Nucl. Inst. Meth. B **102**, (1995)

[Bi87] I. S. Bitensky, E. S. Parilis: *Shock Wave Mechanism Cluster Emission and Organic Molecule Desorption under Heavy Ion Bombardment*
Nucl. Inst. Meth. B **21**, 26 (1987)

[Bl75] G. Blaise, M. Bernheim: *Adsorption of Gases Studied by Secondary Ion Emission Mass Spectrometry*
Surf. Sci. **47**, 324 (1975)

[Br90] D. Briggs, M. P. Seah: *Practical Surface Analysis*
Vol. **1**, Auger and X-ray Photoelectron Spectroscopy, John Wiley, England (1990)

[Br92] D. Briggs, M. P. Seah: *Practical Surface Analysis*
Vol. **2**, Ion and Neutral Spectroscopy, John Wiley, England (1992)

[Ec91] W. Eckstein: *Computer Simulation of Ion-Solid interactions*
Springer-Verlag Berlin Heidelberg (1991)

[En83] W. Ens, R. Beavis, K. G. Standing: *Time-of-Flight Measurements of Cesium-Iodide Cluster Ions*
Phys. Rev. Lett. **50**, 27 (1983)

[Ch001] P. Chabert, A. Lichtenberg, M. Lieberman and A. Marakhtanov: *Instabilities in Low-Pressure Electronengative Inductive Discharges*
Plasma Sources Sci. Technol. **10**, 478 (2001)

[Co71] J. W. Coburn, E. Kay: *A New Technique for the Elemental Analysis of Thin Surface Layers of Solids*
A. Phys. Lett. **19**, 350 (1971)

[Co77] J. W. Coburn, H. F. Winters, T. J. Chuang: *Ion-Surface Interactions in Plasma Etching*
J. Appl. Phys. **48**, 3532 (1977)

[Co91] S. Coon, W. Calaway, J. Burnett. M. Pellin: *Yields and Kinetic Energy Distribution of Sputtered Neutral Copper Clusters*
Surf. Sci. **259**, 275 (1991)

[Co93] S. Coon, W. Calaway, M. Pellin, J. white: *New Findings on the Sputtering of Neutral Metal Clusters*
Surf. Sci. **298**, 161 (1993)

[Co94] S. Coon, W. Calaway, M. Pellin: *Neutral Copper Cluster Sputtering Yields: Ne^+, Ar^+ and Xe^+ Bombardment*
Nucl. Instr. Meth. B **90**, 518 (1994)

[Co003] C. Corr, P.Steen and W. Graham: *Instabilities in an Inductively Coupled Oxygen Plasma*
Plasma Sources Sci. Technol. **12**, 256 (2003)

[Cr99] B. Vincent Crist: *Handbook of Monochromatic XPS spectra*
Volume **1**, The Elements and Native Oxides (Ag–Au), Published by XPS International. Inc, Japan (1999)

[Fe86] L. C. Feldmann, J. W. Mayer: *Fundmentals of Surface and Thin Film Analysis*
Elsevier Science publishing CO. Inc, (1986)

[Fr90] K. Franzreb, A.Wucher, H. Oechsner: *Electron Impact Ionization of Small Silver and Copper Clusters*
Z. Phys. D. **17**, 51 (1990)

[Ga77] S. W. Gaarenstroom, N. Winograd: *Initial and Final State Effects in the ESCA Spectra of Cadmium and Silver Oxides*
J. Chem. Phys. Vol. **67**, 3500 (1977)

[Ga78] B. J. Garrison, N. Winograd, D. E. Harrison, Jr
Phys. Rev. B **18**, 6000 (1978)

[Ga88] B. J. Garrison, N. Winograd, D. M. Deaven, C. T. Reimann, D. Y. Lo, T. A. Tombrello, D. E. Harrison, Jr. and M. H. Shapiro
Phys. Rev. B **37**, 7197 (1988)

[Ge75a] W. Gerhard: *A Model Calculation of the Neutral Molecule Emission by Sputtering Processes*
Z. Phys. B **22**, 31 (1975)

[Ge75b] W. Gerhard, H. Oechsner: *Mass Spectrometry of Neutral Molecules Sputtered from Polycrystalline Metals by Ar^+ - Ions of 100-1000 eV*
Z. Phys. B **22**, 41 (1975)

[Gh002] S. Ghalab, C. Staudt, S. Maksimov, P, Mazarov, N. Dzhemilev, A. Wucher: *Formation of Sputtered Silver Clusters under Bombardment with SF_5^+ Ions*
Nucl. Inst. Meth. B **197**, 43 (2002)

[Gh004] S. Ghalab, A. Wucher: *Cluster Formation at Metal Surface under Bombardment with SF_m^+ (m=1,...,5) and Ar^+ Projectiles*
Nucl. Inst. Meth. B **226**, 264 (2004)

[Gi2000a] I. S. Gilmore, M.P. Seah: *Ion Detection Efficiency in SIMS: Dependencies on Energy, Mass and Composition for Microchannel Plates Used in Mass Spectrometry*
Int. J. Mass Spectr. Ion Process. **202**, 217 (2000)

[Gi98] G. Gillen, S. Roberson: *Preliminary Evaluation of an SF_5^+ Polyatomic Primary Ion Beam for Analysis Organic Thin Films by Secondary Ion Mass Spectrometry*
Rapid Commu. Mass Sp. **12**, 1303 (1998)

[Gi2000] G. Gillen, M. Walker, P. Thompson, J. Bennett: *Use of an SF_5^+ Polyatomic Primary Ion Beam for Ultrashallow Depth Profiling on an Ion Microscope Secondary Ion Mass Spectrometry Instrument*
J. Vac. Sci. Techol. B **18**, 503 (2000)

[Gi003] G. Gillen, A. Fahey: *Secodray Ion Mass Spectrometry Using Cluster Primary Ion Beams*
Appl. Surf. Sci. **(203-204)**, 209 (2003)

[Gn89] H. Gnaser, W.Hofer: *The Emission of Neutral Clusters in Sputtering*
App. Phys. A **48**, 261 (1989)

[Ha76] D. E. Harrison, Jr and C. B Delaplain: *Computer Simulation of the Sputtering Clusters*
J. Appl. Phys. **47**, 2252 (1976)

[Ha81] D. E. Harrison, Jr
J. Appl. Phys. **52**, 1499 (1981)

[Ha98] B. Hagenhoff, P. L. Cobben, C. Bendel, E. Niehuis, A. Benninghoven: *Polymers under SF_5^+ Bombardment - a Systematic Investigation*
Secondary Ion Mass Spectrometry **(SIMS XI)**, eds. G. Gillen, R. Lareau, J. Bennett, F. Stevie Wiley Sons Chichester,1998, p. 585

[He96] R. Heinrich: *Untersuchung zur Bildung Zerstaübter Germanium-Cluster*
Diplomarbeit, Universität Kaiserslautern (1996)

[He2000] R. Heinrich, C. Staudt, M. Wahl, A. Wucher: *Ionization Probability of Sputtered Custers*
Secondary Ion Mass Spectrometry **(SIMS XII)**, eds. P. Bertrand, A. Benninghoven, H.W. Werner (Elsevier, Amsterdam, 2000) p. 111

[He003] R. Heinrich, A. Wucher
Nucl. Instr. Meth. B **207**, 136 (2003)

[Hi27] A. Hippel,: *Zur Theorie der Kathodenzerstaebung*
Ann. Phys. (Leipzig) **80**, 1043 (1927)

[Ho58] R. A. Honig: *Sputtering of Surfaces by Positive Ion Beams of Low Energy*
J. Appl. Phys. **29**, 549 (1958)

[Ho69] G. Hortig and M. Mueller: *Multiatomic Clusters Emerging from a Metal Surface under Ion Bombardment*
Z. Phys. **221**, 119 (1969)

[Ho80] W. O. Hofer
Nucl. Inst. Meth. **170**, 275 (1980)

[Hu96] W. Huinsky, G. Betz: *Fundamental Aspects of SNMS for Thin Film Characterization: Experimental Studies and Computer Simulations*
Thin. Sol. Film. **272**, 289 (1996)

[Ka72] V. I. Karataev, B. A. Mamyrin, D. V. Shmikk
Sov. Phys. -Tech. Phys. **16**, 1177 (1972)

[Ka85] I. Katakuse, T. Ichihara, Y. Fujita, T. Matsuo, T. Sakurai, H. Matsuda: *Mass Distributions of Copper, Silver and Gold Clusters and Electronic Shell Structure*
Int. J. Mass Spectr. Ion Process. **67**, 229 (1985)

[Ka86] I. Katakuse, T. Ichihara, Y. Fujita, T. Matsuo, T. Sakurai, H. Matsuda: *Mass Distributions of Negative Cluster Ions of Copper, Silver and Gold*
Int. J. Mass Spectr. Ion Process. **74**, 33 (1986)

[Kö74] G. P. Können, A. Tip, A. E. de Vries: *On the Energy Distribution of Sputtered Dimers*
Rad. Eff. **21**, 269 (1974)

[Ko94] D. Koch: *Anvendung eines VUV-Lasers zur Nachionisation Gesputterter Neutralteichen*
Diplomarbeit, Universität Kaiserslautern (1994)

[Ko98a] F. Kötter, A. Benninghoven: *Secondary Ion Emission from Polymer Surfaces under Ar^+, Xe^+ and SF_5^+ Ion Bomabrdment*
App. Surf. Sci. **133**, 47 (1998)

[Li61] J. Lindhard, M. Scharff
Phys. Rev. **124**, 128 (1961)

[Li63] J. Lindard, V. Nielsen, M. Scharff and P. V. Thomsen
Mat. Fys. Medd. Dan. Vid. Selsk. **33**, 10 (1963)

[Ma86] K. Mann, M. L. Yu: *Origin of the Chemical Enhancemnet of Postive Secondary Ion Yield in SIMS*
Secondary Ion Mass Spectrometry **(SIMS V)**, eds. A. Benninghoven, R. J. Colton, D. S. Simons, H. W. Werner (Springer, Berlin, Heidelberg 1986), p. 26

[Ma87] K. Mann, M. L. Yu: *Effect of Chemical Bonding on Positive Secondary-Ion Yields In Sputtering*
Phys. Rev. B **35**, 6043 (1987)

[Ma89] W. Matthew, C. Foulkes, R. Haydock: *Tight-Binding Models and Density-Functional Theory*
Phys. Rew. B **39**, 12520 (1989)

[Ma94] Z. Ma, S. R. Coon, W. F. Calaway, M. J. Pellin, D. M. Gruen, E. von Nagy-Felsobuki: *Sputtering of Neutral and Ionic Indium Clusters*
J. Vac. Sci. Technol. A **12**, 2425 (1994)

[Me001] S. Meyer
Diplomarbeit, Universität Essen (2001)

[Nö74] H. Nöller, H. Polaschegg, H. Schillalies
J. Electr. Spectr and Related Phenomena. **5**, 705 (1974)

[Ja92] C. Jackschath, I. Rabin, and W. Schulze Z. Phys. D. **22**, 517 (1992)

[Je92] R. Jede, O. Ganschow, U. kaiser: *Instrumentation for SIMS* Practical Surface Analysis Vol. **2**, Ion and neutral Spectroscopy, eds. D. Briggs, M. Seah (Wiley Frankfurt), p. 83

[Jo79] S. S. Johar, D. A. Thompson: *Spike Effects in Heavy-Ion Sputtering of Ag, Au and Pt Thin Films* Surf. Sci. **90**, 319 (1979)

[Oe74] H. Oechsner, W. Gerhard: *Mass Spectroscopy of Sputtered Neutrals and its Application for Surface Analysis* Sur. Sci. **44**, 480 (1974)

[Oe78] H. Oechsner, H. Schoof, E. Stumpe: *Sputtering of Ions at energies below 1 KeV* Sur. Sci. **76**, 343 (1978)

[Oe83] H. Oechsner, Z. Sroubek Surf. Sci. **127**, 10 (1983)

[Re84] W. Reuter: *An Alternative Primary Beam Source for the Sensitive Detection of Electropostive Elments in SIMS* Secondary Ion Mass Spectrometry **(SIMS IV)**, eds. A. Benninghoven, J. Okano, R. Shimizu, H. W. Werner (Springer, Berlin, Heidelberg 1984), p. 54

[Re87] W. Reuter: *Secondary Ion Emission From Metal Targets under CF_3^+ and O_2^+ Bombardment* Anal. Chem. **59**, 2081 (1987)

[Re88a] W. Reuter, G. Scilla: *Application of a CF_3^+ Primary Ion Source for Depth Profiling in Secondary Ion Mass Spectrometry* Anal. Chem. **60**, 1401 (1988)

[Re88b] W. Reuter, J. Clabes: *Secondary Ion Emission and Sputter Yields from Metal Targets under F_2^+ Bombardment* Anal. Chem. **60**, 1404 (1988)

[Re001] L. E. Rehn, R. C. Birtcher, S. E. Donnelly, P. M. Baldo and L. Funk: *Origin of Atomic Clusters during Ion Sputtering* Phys. Rev. Lett. **87**, 2076011 (2001)

[Ro74] T. Robinson, I. M. Torrens Phy. Rev. B **9**, 5008-5024 (1974)

[Ri90] J. C. Riviere: *Surface Analytical Techniques* Oxford Unversity Press, New York (1990)

[Sa005] A. V. Samartsev, A. Duvenbeck, A. Wucher: *Sputtering of Indium Using Au_m Projectiles: Transition from Linear Cascade to Spike Regime*
Phys. Rev. B (2005) submitted

[Se90] M. P. Seah: *Channel Electron Multipliers: Qanatitative Intensity Measurement- Efficiency, Gain, Linearity and Bias Effects*
J. Electron Spectrosc. Relate. Phenom. **50**, 137 (1990)

[Sh72] D. A. Shirley: *High-Resolution X-Ray Photoemission Spectrum of the Valence Bands of Gold*
Phys. Rev. B **5**, 4709 (1972)

[Si69] P. Sigmund: *Theory of Sputtering. I. Sputtering Yield of Amorphous and Polycrystalline Targets*
Phys. Rev. **184**, 383 (1969)

[Si74] P. Sigmund: *Energy Density and Time Constant of Heavy-Ion-Induced Elastic-Collision Spikes in Solids*
Appl. Phys. Lett. **25**, 169 (1974)

[Si81] P. Sigmund, C. Claussen: *Sputtering from Elastic-Collision Spikes in Heavy Ion Bombardment Metals*
J. Appl. Phys. **52**, 990 (1981)

[Si81a] P. Sigmund, in: *Sputtering by Particle Bombardment I*
Ed. R. Behrisch (Springer, Berlin 1981).

[Si86] P. Sigmund, H. M. Urbassek, D. Matragrano: *A Note on Rotational and Vibrational Motion of Sputtered or Desorbed Diatomic Molecules*
Nucl. Inst. Meth. B **14**, 495 (1986)

[Si87] P. Sigmund: *Machanisms and Theory of Physical Sputtering by Particle Impact*
Nucl. Inst. Meth. B **27**, 1 (1987)

[Sl66] G. Slodzian, J. Hennequin
C. R. Acad. Sci. Paris **263**, 1246 (1966)

[Sl75] G. Slodzian: *Some Problems in Secondary Ion Emission Applied to Elmentary Analysis*
Surf. Sci. **48**, 161 (1975)

[Sl83] G. Slodzian
Phys. Scripta. T **6**, 54 (1983)

[Sm63] A. J. Smith, L. A. Cadbey, D. J. Marshall: *Mass Anaylysis of Sputtered Particles*
J. Appl. Phys. **34**, 2489 (1963)

[SRIM] *For Information on the SRIM Simulation Program See: The Stopping and Range of Ions in Solids by J. Ziegler, J. Biersack, U. Littmark (Pergamon Press, New York, 1985) and http://www.srim.org*

[St08] J. Stark: *Ueber die Zerstaebende Wirkung der Kanalstrahlen (Emission Sekundaerer Atomstrahlen)*
Z. Elektrochem. **46**, 752 (1908)

[St09] J. Stark: *Zur Theorie der Zerstaeubung durch Atomstrahlen*
Z. Elektrochem. **14**, 509 (1909)

[St77] H. A. Storms, K. F. Brown, J. D. Stein: *Evaluation of a Cesium Postive Ion Source for Secondary Ion Mass Spectrometry*
Anal. Chem. **49**, 2023 (1977)

[St98] D. Stapel, O. Brox, A. Benninghoven: *Secondary Ion Emission from Arachidic Acid LB-layers under Ar^+, Xe^+, Ga^+ and SF_5^+ primary Ion Bombardment*
Appl. Surf. Sci. **140**, 156 (1998)

[St2000] C. Staudt, R. Heinrich, A. Wucher: *Formation of Large Clusters During Sputtering of Metal Surfaces*
Nucl. Inst. Meth. B **(164-165)**, 720 (2000)

[St002] C. Staudt, A. Wucher: *Generation of Large Indium Clusters by Sputtering*
Phys. Rev. B **82**, 075419 (2002)

[Th81] M. W. Thompson: *Physical Mechanisms of Sputtering*
Phys. Rep. **69**, 335 (1981)

[To82] S. Tougaard, P. Sigmund: *Influence of elastic and inelastic scattering on energy spectra of electrons emitted from solids*
Phys. Rev. B **25**, 4452 (1982)

[To86] S. Tougaard: *Background Removal in X-ray Photoelectron Spectroscopy: Relative importance of Intrinsic and Extrinsic Processes*
Phys. Rev. B **34**, 6779 (1986)

[To87] S. Tougaard, I. Chorkendorff
Phys. Rev. B **35**, 6570 (1987)

[Ur88] Herbert M. Urbassek: *Sputtered Cluster Mass Distributions, Thermodynamic Equilibrium and Critical Phenomena*
Nucl. Inst. Meth. B **31**, 541 (1988)

[Ur96] Herbert M. Urbassek, Thomas J. Colla: *Effect of Energy Density on Cluster Formation from Energized Metals*
Computational Materials Science **6**, 7 (1996)

[Ur97] Herbert M. Urbassek: *Molecular Dynamics Simulation of Sputtering*
Nucl. Instr. Meth. B **122**, 427 (1997)

[Wa91] M. Wahl
Kaiserslautern, Universität, Diplomarbeit (1991)

[Wa94] M. Wahl, A. Wucher: *VUV Photoionization of Sputtered Neutral Silver Clusters*
Nucl. Inst. Meth. B **94**, 36 (1994)

[Wa95] M. Wahl: *Experimentelle Untersuchungen zur Zerstäubung von Metall-Clustern unter Verwendung der UV/VUV - Photoionisation*
Dissertation, Universität Kaiserlautern (1995)

[Wi55] W. C. Wiley, I. H. Mclaren: *Time-of-Flight Mass Spectrometer With Improved Resolution*
Rev. Sci. Inst. **26**, 1150 (1955)

[Wi77] K. Wittmaack
Nucl. Methods. **1**, 143 (1977)

[Wi78] P. Williams, C. A. Evans, Jr: *Anomalous Enhancement of Negative Sputtered Ion Emission by Oxygen*
Surf. Sci. **78**, 324 (1978)

[Win78] N. Winorgrad, D. E. Harrison, Jr., B. J. Garrison
surf. Sci. **78**, 467 (1978)

[Wi79] P. Williams: *Sputtering Process and Sputtered Ion Emission*
Surf. Sci. **90**, 588 (1979)

[Wi79b] J. L. Wiza: *Microchannel Plate Detectors*
Nucl. Inst. Meth. Vol **162**, 587 (1979)

[Wo64] J. R. Woodyrad, C. B. Cooper: *Mass Spectrometric Study of Neutral Particles Sputtered from Cu by 0-to 100-eV Ar ions*
App. J. Phys. **35**, 1107 (1964)

[Wu87] A. Wucher, H. Oechsner
Nucl. Instr. Meth. B **18**, 458 (1987)

[Wu88] A. Wucher, H. Oechsner: *Emission Energy Dependence of Ionization Probabilities in Secondary Ion Emission from Oxygen Covered Ta, Nb and Cu Surface*
Surf. Sci. **199**, 567 (1988)

[Wu92] A. Wucher, B. J. Garrison
Surf. Sci. **260**, 257 (1992)

[Wu93a] A. Wucher, M. Wahl, H. Oechsner: *Sputtered Neutral Silver Clusters up to Ag_{18}*
Nucl. Inst. Meth. B **82**, 337 (1993)

[Wu93b] A. Wucher, M. Wahl, H. Oechsner: *The Mass Distribution of Sputtered Metal Clusters I. Experiment*
Nucl. Inst. Meth. B **83**, 73 (1993)

[Wu94] A. Wucher, Z. Ma, W. F. Calaway, M. J. Pellin: *Yields of Sputtered Metal Clusters: the Influence of Surface Structure*
Surf. Sci. Lett. **304**, L439 (1994)

[Wu97] A. Wucher, M. Wahl: *Cluster Emission in Sputtering*
Secondary Ion Mass Spectrometry **(SIMS X)**, eds. A. Benninghoven, B. Hagenhoff and H.W. Werner, Wiley, p. 65 (1997)

[Wu96] A. Wucher, M. Wahl: *The Formation of Clusters during Ion Induced Sputtering of Metals*
Nucl. Inst. B **115**, 581 (1996)

[Wu2000] A. Wucher, R. Heinrich, C. Staudt
Secondary Ion Mass Spectrometry **(SIMS XII)**, eds. P. Bertrand, A. Benninghoven, H.W. Werner (Elsevier, Amsterdam, 2000) p. 143

[Wu001] A. Wucher, in: *TOF-SIMS: Surface Analysis by Mass Spectrometry* edited by John C. Vickerman and David Briggs (2001)

[Wu002] A. Wucher
IZV. An. SSSR Fiz. **66**, 499 (2002)

[Ya98] H. Yamamoto, Y. Baba: *Emission of Silicon Cluster Ions by Molecular Ion Bomnardment*
Appl. Phys. Lett. **72**, 2406 (1998)

[Ya2000] H. Yamamoto, F. Esaka, H. Asaoka: *Formation of Negative Carbon Cluster Ions by Molecular Ion Irradiation*
Secondary Ion Mass Spectrometry **(SIMS XII)**, eds. A. Benninghoven, P. Bertrand, H. Migeon, and H. Werner (Elsevier Science Amsterdam, 2000), 295

[Yu86] M. L. Yu, K. Mann: *Bond Breaking and the Ionization of Sputtered Atoms*
Phys. Rev. Lett. **57**, 1476 (1986)

[Yu87] M. L. Yu: *A Bond Breaking Model for Secondary Ion Emission*
Nucl. Inst. Meth. B **18**, 542 (1987)

[Yu88] M. L. Yu: *A Bond-Breaking Model for the Sputtering of Secondary Ions and Excited Atoms*
Secondary Ion Mass Spectrometry **(SIMS VI)**, eds. A. Benninghoven, A. M. Huber, H. W. Werner (Wiley, New York 1988), p. 41

[Yu93] M. L. Yu: *An Overview of the Mechanisms for Secondary Atomic Ion Emission*
Secodary Ion Mass Spectrometry **(SIMS IX)**, eds. A. Benninghoven, Y. Niehei, H. Shimizu, H. W. Werner (Wiley, New York 1993), p. 10

[Zi85] J. F. Ziegler, J. P. Biersack, V. Littmark: *The Stopping and Range of Ions in Solids*
Pergamon, New York (1985)

Acknowledgments

I would like to express my gratitude to all people who have helped me during the period of this work. First of all I am very grateful to Prof. Dr. A. Wucher for giving me the opportunity to perform the present work in his laboratory. Thanks for stimulating discussions and leading hints.

Special thanks to Dipl. Phys. S. Meyer, for his valuable suggestions during the experimental work. Many thanks for Dipl. Phys. P. Mazarov and Dr. A. Samartsev for their technical support during the progress of my work. My great thanks to Dipl. Phys. A. Duvenbeck, for his help and encouragement during writing the thesis.

I would like to thanks my friend M. Sc. A. Khalil (Max-Plank Institute) for his support during the writing of my work. My special thanks to my wife, she was readily to help me at anytime. Finally my gratitude to the Egyptian government for providing financial support.